NMR Studies of Localization and Out-of-Time Ordered Commutators

by

Ken Xuan Wei

B.S. in Physics, University of California, Los Angeles (2011)

Submitted to the Department of Physics
in partial fulfillment of the requirements for the degree of

Doctor of Philosophy in Physics

at the

MASSACHUSETTS INSTITUTE OF TECHNOLOGY

September 2018

Author .... Signature redacted
Department of Physics
August 15, 2018

Certified by................................ Signature redacted
Paola Cappellaro
Associate Professor of Nuclear Science and Engineering
Thesis Supervisor

Certified by............. Signature redacted ....
Senthil Todadri
Professor of Physics
Thesis Supervisor

Accepted by .... Signature redacted
Nergis Mavalvala
Associate Department Head of Physics

NMR Studies of Localization and Out-of-Time Ordered Commutators

by

Ken Xuan Wei

Submitted to the Department of Physics
on August 15, 2018, in partial fulfillment of the
requirements for the degree of
Doctor of Philosophy in Physics

Abstract

This thesis presents a study of many-spin dynamics using a Nuclear Magnetic Resonance (NMR) simulator. A novel correlation metric was designed and experimentally measured in a solid state spin chain system to investigate the dynamics of quantum information transport. By using control techniques to tune the parameters of the system interactions, the effects of disorder and interaction on the dynamics were investigated experimentally. It was shown that in the absence disorder can quench the spread of quantum information; while with weak interaction and disorder, quantum information can spread, albeit slowly. Having found a connection between the correlation metric and the recently proposed out-of-time ordered commutator, the correlation metric was used to experimentally probe a transition between ergodic and prethermal dynamics. Future experiments using out-of-time ordered commutators as a tool to probe many-body localization transition are discussed.

Thesis Supervisor: Paola Cappellaro
Title: Associate Professor of Nuclear Science and Engineering

Thesis Supervisor: Senthil Todadri
Title: Professor of Physics

Acknowledgments

First and foremost, I would like to thank my thesis supervisor Paola Cappellaro for her relentless optimism, and for believing in me at times when I did not believe in myself. Her uncompromising strive for excellent work has motivated me to do the same in all aspects of life.

I would like to thank Sekhar Ramanathan, who has taught me many of the nuts and bolts of solid state NMR and collaborated with me on all the projects. It is always refreshing to hear his insights and suggestions on new experiments.

I would like to thank Seth Lloyd, for sharing his constant flow of original ideas. I would also like to thank Oles and Iman, for collaborating on the theory sides of the projects.

I would like to thank Senthil Todadri and Raymond Ashoori, my thesis committee members, for working with me towards the completion of my degree, and for patiently listening to my research and giving me advice.

I would like to thank all members of the Quantum Engineering Group at MIT, for being inspirational colleagues as well as good friends. In particular I would like to thank Pai Peng, who has helped me on all aspects of the OTO commutator project.

I would like to thank my family and friends at MIT for their support throughout the years. I would like to thank Shijun Sung for all the Starcraft games we played together. I would like to thank my wife Chelsea Zhang for agreeing to spend her life with me, despite my many shortcomings.

Contents

List of Figures

Chapter 1

Introduction

This thesis is about nuclear magnetic resonance (NMR) studies of localization and out-of-time ordered correlations in spin chains. This chapter will focus on the basics of solid state NMR, with emphasis on multi-pulse techniques and multiple quantum coherence (MQC). Chapter 2 will be on spin localization in quasi-one dimensional systems, in particular how one can use NMR techniques to experimentally characterize the spread of quantum information. Chapter 3 will be on out-of-time ordered (OTO) commutators in quantum Ising chains. Chapter 4 will present experimental measurements of of OTO commutators in dipolar chains, with applications to prethermalization and scrambling. Chapter 5 proposes experiments to observe signatures of many-body localization to ergodic transition in three dimensions, as well as prethermalization due to weak integrability breaking. Some preliminary experimental data will be provided.

1.1 Solid State Nuclear Magnetic Resonance

In a crystal lattice, nuclear spins are strongly coupled to each other via magnetic dipole-dipole interactions given by the Hamiltonian [3, 134, 103]

$$H_{\text{dip}} = \sum_{j<k} \frac{\hbar \gamma_j \gamma_k}{|\vec{r}_{jk}|^3} \left[\vec{S}_j \cdot \vec{S}_k - \frac{3\vec{S}_j \cdot \vec{r}_{jk}\, \vec{S}_k \cdot \vec{r}_{jk}}{|\vec{r}_{jk}|^2} \right], \tag{1.1}$$

where γ_j is the gyromagnetic ratio of the j-th spin, $\mathrm{S} = \sigma/2$ is the spin-1/2 angular momentum operator, and $\vec{r}_{jk}$ is the vector between the j-th to k-th spins. In the presence of a strong magnetic field the dipolar Hamiltonian is truncated to the secular dipolar Hamiltonian where only interactions that commute with the magnetic field survive. When the magetic field is along the z-axis, the secular dipolar Hamiltonian in the rotating frame is given by [3, 134, 103]

$$H_{\text{dipz}} = \hbar \sum_{j<k} \gamma_j \gamma_k \frac{1 - 3\cos(\theta_{jk})^2}{2|\vec{r}_{jk}|^3} (2S_z^j S_z^k - S_x^j S_x^k - S_y^j S_y^k) \tag{1.2}$$

where θ_{jk} is the angle between the vector $\vec{r}_{jk}$ and the magnetic field z-axis. When another spin 1/2 specie I is present in the system, there will be a heteronuclear interaction between the S and I spins given by

$$H_{IS} = \hbar \sum_{j<k} \gamma_j \gamma_k \frac{1 - 3\cos(\theta_{jk})^2}{2|\vec{r}_{jk}|^3} S_z^j I_z^k \tag{1.3}$$

1.1.1 Equilibrium State

In thermal equilibrium the density matrix of the spins is given by the Boltzman distribution [3, 134]: $\rho_{\text{eq}} = \mathcal{Z}^{-1} e^{-\beta(-\omega_L \sum_j S_z^j + H_{\text{dipz}})}$, where $\omega_L = \gamma$ is the Larmor frequency, $\beta = (k_B T)^{-1}$ is the inverse temperature, and $\mathcal{Z} = \mathrm{Tr}\left[e^{-\beta(\omega_L \sum_j S_z^j + H_{\text{dipz}})}\right]$ is the partition function. Even in a high magnetic field of 7 Tesla, the room temperature thermal energy $k_B T$ is many orders of magnitude larger than $\hbar\omega_L$, which is itself is many orders of magnitude larger than the energy scales of H_{dipz}. Thus the equilibrium density matrix can be well approximated as

$$\rho_{\text{eq}} \approx (\mathbb{1} - \epsilon \sum_{j=1}^{L} S_z^j)/2^L \tag{1.4}$$

where L is the number of spins and $\epsilon \ll 1$. Since $\mathbb{1}$ does not evolve under unitatry evolution, only the deviation from $\mathbb{1}$ contribute to the measured NMR signal.

1.1.2 Spin Manipulation and Detection

Coherent manipulation of the spins is accomplished by applying radio-frequency (rf) pulses on resonance with ω_L. In practice the sample is placed in the center of a solenoid coil oriented perpendicularly to the external magnetic field, a strong rf pulse is sent into the coil which creates a time-dependent field across the sample. In the rotating frame during the pulse, the spins see a static magnetic field pointing in the x-y plane and are collectively rotated according to the right-hand rule (for negative gryomagnetic ratio) or the left-hand rule (for positive gyromagnetic ratio). In the laboratory frame, the Hamiltonian for a on-resonance rf pulse along the x axis is given by $H_{\text{rf}}(t) = \Omega \sum_j S_x^j \cos(\omega_L t - \phi)$, where Ω the amplitude and ϕ is the phase. In the rotating frame, after making the rotating-wave approximation [31], the rf Hamiltonian is static for the duration of the pulse and is given by

$$H_{\text{rf}}^{\text{rot}} = \frac{\Omega}{2}\left[\sum_j S_x^j \cos(\phi) - \sum_j S_y^j \sin(\phi)\right]$$

Hence by changing ϕ one can change the pulse direction in the rotating frame. If a pulse is applied for a time t_w corresponding to $\Omega t_w = \pi/2$, then the pulse is referred to as a $\pi/2$-pulse. $\theta = \Omega t_w$ is also called the flip angle. In reality, the pulses in the rotating frame are never in perfect square form. Each pulse always has a leading and a trailing transient, as it takes a finite time to switch on and off the amplifier. The effect of this particular pulse imperfection in multi-pulse NMR experiments can be minimized by "symmetrizing" the sequence (see [54] and also Appendix A).

The total magnetization of the spins is detected inductively. First a $\pi/2$ pulse is applied to bring the z magnetization into the x-y plane. As the spins precess due to the external magnetic field and create a changing flux, a current is induced in the solenoid by Faraday's law of induction [134]. This current is then amplified and digitized to give the measured signal. NMR measurements are ensemble measurements, where only total magnetization of the spin ensemble can be measured.

1.2 Hamiltonian Engineering and Multi-pulse Techniques

The strong dipolar coupling is responsible for the large linewidth observed in the free-induction decay (FID) spectrum in solid state systems. In order to increase the resolution (narrow the linewidth), it is necessary to decouple the spins from their dipolar interactions. In solid state NMR, the two most common approaches to homonuclear decoupling are Magic angle spinning (MAS) [10, 11] and multi-pulse sequences [141, 55, 54, 103]. MAS relies on the fact that the angular dependence of the secular Hamiltonian averages to zero when the sample is rotated at the magic angle $\theta_{\mathrm{m}} = \arccos(1/\sqrt{3})$ [10, 11]. On the other hand, multi-pulse decoupling relies on the fact that $H_{\mathrm{dipx}} + H_{\mathrm{dipy}} + H_{\mathrm{dipz}} = 0$. Thus by switching the secular Hamiltonian evenly between x, y, and z one can effectively decouple the dipolar interactions. The most famous multi-pulse sequence is the Waugh-Huber-Haebelrn (WHH4) sequence [141]:

$$\tau - \mathbf{x} - \tau - \bar{\mathbf{y}} - 2\tau - \mathbf{y} - \tau - \bar{\mathbf{x}} - \tau$$

where τ is a delay, $\mathbf{x}(\mathbf{y})$ represent a $\pi/2$ pulse along the x(y) direction, and $\{\bar{\mathbf{x}}, \bar{\mathbf{y}}\} \equiv \{-\mathrm{x}, -\mathrm{y}\}$. For the moment assume the pulses are infinitely short so the rotation of the spins is instantaneous. While in the rotating frame the Hamiltonian during the delays is always H_{dipz}, in the interaction frame given by the pulses however, the Hamiltonian is evenly toggled between H_{dipz}, H_{dipy}, and H_{dipx}. Thus over one cycle the Hamiltonian is averaged to zero to leading order. Higher order terms depend on nested commutators involving H_{dipz}, H_{dipy}, and H_{dipx}; these terms can be made small by decreasing the cycle time of the pulse sequence. Unsurprisingly, the interaction frame given by the pulses is also called the toggling frame. Notice that the effect of the pulses over one cycle is identity, so the rotating frame and toggling frame coincides when the system is observed in "windows" in sync with the pulse sequence, i.e., stroboscopically. The property $U_{\mathrm{rf}}(t_c) = \mathbb{1}$ can be taken as definition of a cycle. Because of the periodicity of the multi-pulse sequence, the dynamics of the system is governed by a Floquet Hamiltonian. While conceptually simple, the performance of multi-pulse methods depends on many factors such as pulse imperfections and higher order corrections to the average Hamiltonian, and many techniques have been developed to compensate for these effects [54]. The general approach to analyze multi-pulse NMR is given by average Hamiltonian theory (AHT), which provides a systematic procedure to obtain a time-independent Hamiltonian to describe the dynamics observed stroboscopically [54]. For a description of AHT see Appendix A.

WHH4 is one of the pioneering discoveries that started the development of high resolution solid state NMR using multi-pulse methods, many subsequent pulse sequences such as MREV8 [102, 121], BR24 [22], and CORY48 [32] have been invented to further improve the resolution.

1.2.1 Hamiltonian Engineering

Not only can multi-pulse sequence be used to accomplish homonuclear decoupling, it can also be used to do Hamiltonian engineering. Denote a generic 4-pulse sequence as $P(\tau_1, \mathbf{n}_1, \tau_2, \mathbf{n}_2, \tau_3, \mathbf{n}_3, \tau_4, \mathbf{n}_4, \tau_5)$, where $\mathbf{n}_j$ represents the direction of the j-th $\pi/2$ pulse, and τ_j's the delays interleaving the pulses. The $\pi/2$ pulses have a width t_w of typically 1 μs. τ_j starts and/or ends at the midpoints of the pulses. Consider a 16-pulse sequence given by

$$P(\tau_1, \mathbf{x}, \tau_2, \mathbf{y}, 2\tau_3, \mathbf{y}, \tau_2', \mathbf{x}, \tau_1')P(\tau_1', \mathbf{x}, \tau_2, \mathbf{y}, 2\tau_3', \mathbf{y}, \tau_2', \mathbf{x}, \tau_1)P(\tau_1, \bar{\mathbf{x}}, \tau_2', \bar{\mathbf{y}}, 2\tau_3', \bar{\mathbf{y}}, \tau_2, \bar{\mathbf{x}}, \tau_1')P(\tau_1', \bar{\mathbf{x}}, \tau_2', \bar{\mathbf{y}}, 2\tau_3, \bar{\mathbf{y}}, \tau_2, \bar{\mathbf{x}}, \tau_1) \tag{1.5}$$

where the delays are given by

$$\begin{aligned} \tau_1 &= \tau(1 + 3c - v + w), & \tau_2 &= \tau(1 + 3b - u + v), & \tau_3 &= \tau(1 - 3a + u - w), \\ \tau_1' &= \tau(1 - 3c - v + w), & \tau_2' &= \tau(1 - 3b - u + v), & \tau_3' &= \tau(1 + 3a + u - w), \end{aligned}$$

In the experiments τ is typically 4 μs. The cycle time t_c, defined as the total time of the sequence, is given by $t_c = 24\tau$. u, v, w, a, b and c are dimensionless adjustable parameters, they are restricted such that none of the inter-pulse spacings becomes negative.

Using the sequence given by Eq.(1.5), the secular dipolar Hamiltonian $H_{\text{dip}} = \frac{1}{2}\sum_{j<k} J_{jk}(2S_z^j S_z^k - S_x^j S_x^k - S_y^j S_y^k) + \sum_j h_j S_z^j$ can be engineered into an average Hamiltonian (or Floquet Hamiltonian) with tunable interactions given by

$$H_0 = \frac{1}{2}\sum_{j<k} J_{jk}\left[(u-w)S_x^j S_x^k + (v-u)S_y^j S_y^k + (w-v)S_z^j S_z^k\right] + \sum_j h_j(aS_x^j + bS_y^j + cS_z^j), \tag{1.6}$$

with null correction in first order (with finite pulse width) thanks to the sequence being symmetric (see Appendix). Thus the leading correction is of second order. The sequence given by Eq.(1.5) allows one to tune the relative strength of each terms in H_0, thereby allowing one to explore different phases of the Hamiltonian. Furthermore, by properly adjusting the delays and phases in sequence, one can invert the sign of H_0. As it will be shown later, time reversal is critical to the measurement scheme of multiple quantum coherence intensities and out-of-time ordered commutators.

In addition, a uniform transverse field can be introduced into Eq.(1.6) in two ways. One strategy is to simply apply pulses off-resonance, so that the resulting H_0 contains the term $c\Delta\omega \sum_j S_z^j$, where $\Delta\omega$ is the resonance offset. This approach is easy to implement, but it cannot achieve independent control over the disordered and uniform fields, and it can result in lower-quality pulses. We use a second approach which is based on phase-shifting the entire pulse sequence. Consider rotating the n-th cycle of the pulse sequence by $(n-1)\phi$ around the $\hat{z}$ axis, which can be accomplished by phase shifting all the pulse directions $\mathbf{n}_j$ in the n-th cycle by $(n-1)\phi$. The evolution operator for each cycle is given by

$$\begin{aligned}
U_1 &= e^{-iH_0 t_c} \\
U_2 &= e^{-i\phi Z} e^{-iH_0 t_c} e^{i\phi Z} \\
U_3 &= e^{-2i\phi Z} e^{-iH_0 t_c} e^{2i\phi Z} \\
&\vdots \\
U_n &= e^{-i(n-1)\phi Z} e^{-iH_0 t_c} e^{i(n-1)\phi Z}
\end{aligned}$$

where $Z = \sum_j S_z^j$. The total evolution operator over n cycles is given by the product:

$$\begin{aligned} U(nt_c) &= U_n U_{n-1} \cdots U_3 U_2 U_1 = e^{-in\phi Z} \left[e^{i\phi Z} e^{-iH_0 t_c} \right]^n \\ &\approx e^{-in\phi Z} e^{-i\left(H_0 - \frac{\phi}{t_c} Z\right) nT} = e^{-in\phi Z} e^{-iH_t n t_c}, \end{aligned} \tag{1.7}$$

where the total Hamiltonian is given by $H_t = H + bZ$, with $b = -\phi/t_c$. The rotation approach also generates an extra term $e^{-in\phi Z}$, this term can be eliminated by appropriately changing the phase of the encoding pulse (see section on MQC measurements) or the readout pulse. The advantage of this method is allowing one to independently tune the disordered field by adjusting c, and the uniform field by varying b.

Notice that multi-pulse techniques can be applied more broadly to engineer desired Hamiltonians H_{des} using only collective rotations of the spins applied to the naturally occurring Hamiltonian, H_{nat}. The engineered Hamiltonian is obtained by piece-wise constant evolution under rotated versions of the natural Hamiltonian under the condition $\sum_k R_k H_{nat} R_k^\dagger = H_{des}$, where R_k are collective rotations of all the spins, which achieves the desired operator to first order in a Magnus expansion. Symmetrization of the sequence can further cancel out the lowest order correction [54].

Using only collective pulses limits which Hamiltonians can be engineered, due to symmetries of the natural Hamiltonian and the action of collective operators. For typical two-body interactions of spin-1/2, an efficient tool to predict which Hamiltonian are accessible is to use spherical tensors [4].

1.2.2 Universal Decoupling and Refocusing Sequences

Interestingly, there are universal pulse sequences which can time reverse any time reversable Hamiltonian [94, 95]. NMR observations of dipolar echoes using such a universal sequence have been made in water and adamantane at zero field [96]. To see how this is possible, first consider what Hamiltonian can be decoupled by collective rotations. One can in general write the interaction Hamiltonian between two spins as $(S_x \quad S_y \quad S_z) D (S_x \quad S_y \quad S_z)^{\mathrm{T}}$, where D is a 3 by 3 real matrix, and D can be different for other pairs of spins. A collective rotation on the S spins is equivalent to an orthogonal transformation of the D matrix: $D \rightarrow D' = \lambda D \lambda^{\mathrm{T}}$. Since orthogonal transformations preserve the trace, the minimal requirement to decouple a Hamiltonian, i.e., $D \rightarrow 0$, is for D to be traceless [30]. The secular dipolar interaction is such a Hamiltonian where D is diagonal with elements $(1 \quad 1 \quad -2)$.

It turns out that $\mathrm{Tr}(D) = 0$ is sufficient to find a universal decoupling sequence. Consider a three pulse subcycle P_3 given by

$$\tau/2 - \left(\frac{2\pi}{3}\right)_{111} - \tau - \left(\frac{2\pi}{3}\right)_{111} - \tau - \left(\frac{2\pi}{3}\right)_{111} - \tau/2$$

where $\left(\frac{2\pi}{3}\right)_{111}$ is a $2\pi/3$ pulse along the $x+y+z$ direction. In the toggling frame, P_3 cyclically permutes the diagonal elements as well as the off diagonal elements of D. Since $\mathrm{Tr}(D) = 0$, P_3 refocuses the diagonal elements of D. In order to refocus the off diagonal elements, one can interleave π pulses in between multiple P_3 subcycles and symmetrize the sequence to obtain

$$P_3 \pi_x P_3 \pi_y P_3 \pi_x P_3 \bar{P}_3 \pi_{-x} \bar{P}_3 \pi_{-y} \bar{P}_3 \pi_{-x} \bar{P}_3 \tag{1.8}$$

The sequence given by Eq. (1.8) is a universal decoupling sequence capable of decoupling any Hamiltonian satisfying $\mathrm{Tr}(D) = 0$ to leading order. It will be interesting to investigate how well the above sequence perform with realistic experimental imperfections, such as finite pulse widths, flip angle errors, and pulse transients.

To make a universal refocusing sequence to reverse any Hamiltonian, start from the decoupling sequence given in Eq. (1.8) and perturb the delays to obtain

$$P_3' P_3 \pi_y P_3 \pi_x P_3 \bar{P}_3 \pi_{-x} \bar{P}_3 \pi_{-y} \bar{P}_3 \bar{P}_3'$$

where P_3' is given by

$$\left(\frac{2\pi}{3}\right)_{111} - \tau - \left(\frac{2\pi}{3}\right)_{111} - \tau - \left(\frac{2\pi}{3}\right)_{-1-11} \tag{1.9}$$

To leading order, Eq.(1.9) can reverse any Hamiltonian with $\mathrm{Tr}(D) = 0$ by making

$D \to -kD$, where $k = 1/11$ is the theoretical maximum scaling factor obtainable when both one-body and two-body interactions are present [94]. However when only one-body or two-body interactions are present, larger scaling factors are achievable. Remarkably, work by [94, 95] provides a group theory approach to systematically construct universal decoupling and refocusing sequences, with bounds on scaling factors. More recently a numerical recipe for finding universal decoupling sequences is given by [30].

1.3 Multiple Quantum Coherence (MQC)

Multiple quantum coherence is a technique used to study the many-spin dynamics in NMR system [17, 24]. Mathematically, MQC can be understood as a Fourier decomposition of a many-spin operator $\mathcal{O}$ with respect to another operator $\mathcal{P}$ satisfying $e^{-2im\pi P} = \pm\mathbb{1}$, where m is an integer. For simplicity consider the experimentally relevant case where $P = \sum_j \mathbf{S}_j \cdot \mathbf{n}$ is the generator of global spin rotation around the $\mathbf{n}$-axis. Any traceless many-spin operator $\mathcal{O}$ can be decomposed as

$$\mathcal{O} = \sum_{q=-L}^{q=L} \mathcal{O}_q \tag{1.10}$$

where L is the total number of spins in the system, and $\mathcal{O}_q$ satisfies following two equivalent relations:

$$e^{-i\theta P}\mathcal{O}_q e^{i\theta P} = e^{-iq\theta}\mathcal{O}_q, \qquad [P, \mathcal{O}_q] = q\mathcal{O}_q. \tag{1.11}$$

From the first relation it is evident that $\mathcal{O}_q = \mathcal{O}^\dagger_{-q}$. What do each multiple quantum component $\mathcal{O}_q$ mean physically? Consider for a moment that $P = \sum_j S^j_z$, then $\mathcal{O}_q$ are the terms in $\mathcal{O}$ that satisfy $q = n_+ - n_-$, where $n_\pm$ is the number of $S^j_\pm = S^j_x \pm iS^j_y$ operators. For example let $\mathcal{O} = S^1_x S^2_y S^3_z + S^1_x S^2_z$, then the multiple quantum components of this operator are given by

$$\mathcal{O}_0 = \frac{1}{4i}(S_-^1 S_+^2 S_z^3 - S_+^1 S_-^2 S_z^3), \qquad \mathcal{O}_{\pm 1} = \frac{1}{2i} S_\pm^1 S_z^2, \qquad \mathcal{O}_{\pm 2} = \pm\frac{1}{4i}(S_\pm^1 S_\pm^2 S_z^3).$$

For a given $\mathcal{O}$, each multiple quantum component $\mathcal{O}_q$ can be formally written as

$$\mathcal{O}_q = \frac{1}{2\pi}\int_0^{2\pi} d\theta e^{iq\theta} e^{-i\theta P}\mathcal{O}e^{i\theta P}. \tag{1.12}$$

which indicates that the multiple quantum components $\mathcal{O}_q$ come from the Fourier decomposition of $\mathcal{O}$ with respect to P. In addition, it can also be shown that $\mathcal{O}_q$ obey the following orthogonality condition:

$$\begin{aligned}
\mathrm{Tr}(\mathcal{O}_q\mathcal{O}_{q'}) &= \frac{1}{4\pi^2}\int_0^{2\pi} d\theta' \int_0^{2\pi} d\theta e^{i(q\theta+q'\theta')}\mathrm{Tr}(e^{-i\theta P}\mathcal{O}e^{i\theta P}e^{-i\theta' P}\mathcal{O}e^{i\theta' P}) \\
&= \frac{1}{4\pi^2}\int_0^{2\pi} d\theta' \int_0^{2\pi} d\theta e^{i(q\theta+q'\theta')}\mathrm{Tr}(e^{-i(\theta-\theta')P}\mathcal{O}e^{i(\theta-\theta')P}\mathcal{O}) \\
&= \frac{1}{4\pi^2}\int_0^{2\pi} d\theta' \int_0^{2\pi} d\theta e^{i(q\theta+q'\theta')}\sum_l e^{-i(\theta-\theta')l}\mathrm{Tr}(\mathcal{O}_l\mathcal{O}) \\
&= \sum_l \delta_{ql}\delta_{q'(-l)}\mathrm{Tr}(\mathcal{O}_l\mathcal{O}) \propto \delta_{q(-q')}
\end{aligned}$$

Using the fact that the maximum q allowed is equal to the total number of spins L, one can rewrite Eq. (1.12) as a discrete Fourier transform:

$$\mathcal{O}_q = \frac{1}{2L}\sum_{m=0}^{2L-1} e^{i\frac{qm\pi}{L}} e^{-i\frac{m\pi P}{L}}\mathcal{O}e^{i\frac{m\pi P}{L}}. \tag{1.13}$$

Notice that there is a slight complication with this equation at $q = L$, namely the RHS actually gives $\mathcal{O}_L + \mathcal{O}_{-L}$ instead of $\mathcal{O}_L$. This is because $\mathcal{O}_{\pm L}$ transforms the same way at $q = L$ and thus cannot be separated. In order the separate $\mathcal{O}_{\pm L}$ one needs an extra transformation given by $ie^{-i\frac{\pi P}{2L}}(\mathcal{O}_L + \mathcal{O}_{-L})e^{i\frac{\pi P}{2L}} = \mathcal{O}_L - \mathcal{O}_{-L}$.

An alternative way to find $\mathcal{O}_q$ is to use the second relationship in Eq. (1.11). Starting from $[P, \mathcal{O}] = \sum_q q\mathcal{O}_q$, by repeatedly commuting both sides with P one can generate a linear system in $\mathcal{O}_q$:

$$\begin{aligned}
[P,\mathcal{O}] &= \sum_q q\mathcal{O}_q \\
[P,[P,\mathcal{O}]] &= \sum_q q^2\mathcal{O}_q \\
[P,[P,[P,\mathcal{O}]]] &= \sum_q q^3\mathcal{O}_q \\
&\vdots \\
\underbrace{[P,[P,[P,[P,\cdots[P,}_{2L}\mathcal{O}],\cdots]]]] &= \sum_q q^{2L}\mathcal{O}_q.
\end{aligned}$$

Using $\mathcal{O}_q^{\pm} = \mathcal{O}_q \pm \mathcal{O}_{-q}$, one can rewrite the above into two linear systems of equations:

$$\begin{bmatrix} [P,\mathcal{O}] \\ [P,[P,[P,\mathcal{O}]]] \\ [P,[P,[P,[P,[P,\mathcal{O}]]]]] \\ \vdots \end{bmatrix} = \begin{bmatrix} 1 & 2 & 3 & \cdots \\ 1^3 & 2^3 & 3^3 & \cdots \\ 1^5 & 2^5 & 3^5 & \cdots \\ \vdots & \vdots & \vdots & \ddots \end{bmatrix} \begin{bmatrix} \mathcal{O}_1^- \\ \mathcal{O}_2^- \\ \vdots \\ \mathcal{O}_L^- \end{bmatrix} \tag{1.14}$$

$$\begin{bmatrix} [P,[P,\mathcal{O}]] \\ [P,[P,[P,[P,\mathcal{O}]]]] \\ [P,[P,[P,[P,[P,[P,\mathcal{O}]]]]]] \\ \vdots \end{bmatrix} = \begin{bmatrix} 1^2 & 2^2 & 3^2 & \cdots \\ 1^4 & 2^4 & 3^4 & \cdots \\ 1^6 & 2^6 & 3^6 & \cdots \\ \vdots & \vdots & \vdots & \ddots \end{bmatrix} \begin{bmatrix} \mathcal{O}_1^+ \\ \mathcal{O}_2^+ \\ \vdots \\ \mathcal{O}_L^+ \end{bmatrix} \tag{1.15}$$

The constant matrices are in the form of Vandermondes matrix, and can be exactly inverted. Thus, by calculating nested commutators of $\mathcal{O}$ and P one can find all the multiple quantum components $\mathcal{O}_q$. In practice, it is more efficient to use Eq. (1.15) than Eq. (1.12) for finding multiple quantum components. This is because when P is sparse, computing nested commutator is faster than computing $e^{-i\frac{m\pi P}{L}}\mathcal{O}e^{i\frac{m\pi P}{L}}$. Eq. (1.15) will also be useful later for finding higher order corrections in prethermal Hamiltonians.

1.3.1 Measuring MQC Intensities

The rotation properties of MQC (first relation in Eq. (1.11)) can instead be used to detect MQC intensities experimentally. Quantum coherences in the **n**-basis are classified based on their response to rotations around the **n** axis: A state of coherence order q, when rotated around the axis **n** by an angle φ, will pick up a phase equal to $q\varphi$, i.e, $e^{-i\varphi\sum_j S_{\mathbf{n}}^j}\rho_q e^{i\varphi\sum_j S_{\mathbf{n}}^j} = e^{-iq\varphi}\rho_q$. This property is often used in NMR experiments to select a particular coherence order, by a procedure called *phase cycling* [21] that amounts to averaging measurements done with phase-shifted pulse sequences.

To see this, consider expanding the density matrix as a sum of quantum coherences: $\rho = \sum_q \rho_q$. If one wish, for example, to keep only the even order coherences, one can measure $\rho + \rho_\pi$, where ρ_π is the density matrix rotated around **n** by π. In ρ_π, all odd order coherences pick up a minus sign and exactly cancel their counterparts when added to ρ, leaving only $\rho_{q\in\text{even}}$. Notice that quantum coherences are defined with respect to a given axis of rotation. Different axes of rotation give rise to different sets of quantum coherences.

Let $\mathcal{O} = \rho$, the MQC intensity of order q is defined as $I_q = \text{Tr}[\rho_q \rho_{-q}]$, that is, I_q can be understood as the weight of the q-th order coherence in the density matrix. MQC intensities are an incomplete measure of many-spin correlations since a signal in I_q indicates there are at least $|q|$ spins present in the correlations. On the other hand, a correlation with m spins can in principle give rise to all I_q with $q = -m, -m+1, \cdots, m$.

MQC intensities can be measured in four steps. The schematic of a conventional MQC experiment is shown in Fig. 1-1B. During preparation, the system initially at ρ_{eq} is driven to evolve under a many-body Hamiltonian H, thereby generating many-spin correlations. An encoding pulse, described by the unitary operator $e^{-i\varphi Z}$, tags the quantum coherences according to their coherence orders. The refocusing step implements the time-reversed evolution to bring the system back into magnetization, which can then be detected by a $\pi/2$ pulse. In our system, the sign of the Hamiltonian can be inverted by adjusting parameters in the pulse sequence (see section 1.2.1). The overall signal of the MQC experiment can be expressed as

$$\begin{aligned}S_\varphi &= \mathrm{Tr}[U^\dagger e^{-i\varphi Z} U \rho_{\mathrm{eq}} U^\dagger e^{i\varphi Z} U Z] \\ &\propto \mathrm{Tr}[e^{-i\varphi Z} \delta\rho e^{i\varphi Z} \delta\rho] = \sum_q e^{-iq\varphi} \mathrm{Tr}[\delta\rho_q \delta\rho_{-q}] = \sum_q e^{-iq\varphi} I_q \end{aligned} \tag{1.16}$$

where $\delta\rho \propto UZU^\dagger \propto U\rho_{\mathrm{eq}}U^\dagger - \mathbb{1}/2^L$ and we have used the identity $\mathrm{Tr}[\delta\rho_q \delta\rho_p] = I_q \delta_{q,-p}$ in the second to last step. To extract the intensities I_q, we perform a series of MQC experiments as we vary φ from 0 to 2π in steps of $\frac{\pi}{M}$, where M is the maximum coherence order to be measured. By performing a discrete Fourier transform (DFT) with respect to φ, the MQC intensities can be found

$$I_q \propto \sum_{m=1}^{2M} e^{-i\frac{qm\pi}{M}} S_m, \tag{1.17}$$

where S_m is the signal of the m-th MQC experiment with $\varphi = m\pi/M$. Notice that the encoding pulse $e^{-i\varphi Z}$ is not implemented by a physical pulse, but rather by phase shifting all the pulses in the preparation step. However, a encoding pulse $e^{-i\varphi X}$ is implemented by two physical pulse: $e^{-i\varphi X} = \left(\frac{\pi}{2}\right)_Y e^{-i\varphi Z} \left(\frac{\pi}{2}\right)_{-Y}$, and the $\left(\frac{\pi}{2}\right)_{-Y}$ pulse is phase shifted along with all the pulses in the preparation sequence during encoding.

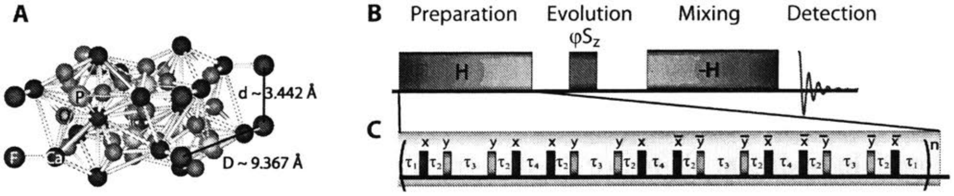

Figure 1-1: **Naturally occurring spin chain sample and experimental technique.** **A** Fluorapatite crystal structure, showing the Fluorine and Phosphorus spins in the unit cell. **B** NMR scheme for the generation and detection of MQC. In the inset (**C**) an exemplary pulse sequence for the generation of the double-quantum Hamiltonian.

1.3.2 Phenomenological Models of MQC Intensities

Finding I_q exactly in dynamic systems with large number of spins is not practical, as the dimension of matrices increases exponentially with system size. However, phenomenological models have been developed to explain MQC intensity distributions observed in experiments with large number of spins.

According to the phenomenological model [17], at a given time the correlations in the system have spread to at most l spins, and within this cluster of l spins all possible types of correlations are equally likely. One can then use a distribution to describe all the spin correlations. For example the probability of finding a k-spin correlation is proportional to $3^k\binom{l}{k}$, since each of the k spins can be either S_x, S_y, or S_z, and there are $\binom{l}{k}$ way to choose k spins. The distribution function can be written as

$$p_k(l) = \frac{3^k}{4^l - 1}\binom{l}{k} \tag{1.18}$$

From this distribution one can calculate the first moment, or the average number of correlated spins: $\sum_{k=1}^{l} k p_k = 3l/4$.

If the phenomenological model is valid, what experimental signature can one expect from the distribution given by Eq. (1.18)? Let $P = \sum_j S_z^j$ and assuming all correlations are equally likely, one can expect the MQC intensity I_q from l spins to have the following form:

$$I_q \propto \sum_{n_+ - n_- = q} 2^{l-n_+-n_-}\binom{l}{n_+ + n_-}\binom{n_+ + n_-}{n_+}$$

Recall that I_q comes from spin correlations satisfying $q = n_+ - n_-$. For a given $n_+ + n_-$ there are $\binom{l}{n_+ + n_-}$ combinations, and for each combination there are $\binom{n_+ + n_-}{n_+}$ permutations. In addition, there are $l - n_+ - n_-$ remaining spins that can be either S_z or I giving an addition factor of $2^{l-n_+-n_-}$. By summing over all possibilities I_q can be written as

$$I_q = \frac{1}{\mathcal{N}}\sum_{n_-=0}^{q} \frac{2^{l-q-2n_-} l!}{(l-q-2n_-)!(q+n_-)!n_-!} = \frac{1}{\mathcal{N}}\frac{\Gamma(2l+1)}{\Gamma(l+1-q)\Gamma(l+1+q)} \tag{1.19}$$

where $\Gamma(n) = (n-1)!$ is the gamma function. Notice that I_q is a even function of q, as expected from the definition $I_q \propto \mathrm{Tr}(\mathcal{O}_q\mathcal{O}_{-q})$. The normalization constant $\mathcal{N}$ can be determined from

$$\sum_q I_q = \sum_q \mathrm{Tr}(\mathcal{O}_q\mathcal{O}_{-q}) = \|\mathcal{O}\|^2,$$

where $\|\mathcal{O}\| = \sqrt{\mathrm{Tr}(\mathcal{O}\mathcal{O}^\dagger)}$ is the Frobenius norm of $\mathcal{O}$. For simplicity let $\|\mathcal{O}\|$ be unity. If the Hamiltonian has no particular symmetry and all coherence orders can be excited, then q take all integer values from $-l$ to l giving a normalization factor of $\mathcal{N} = 4^l$. If the Hamiltonian and initial state are such that only even q or odd q can be exicited, then the normalization factor is $\mathcal{N} = 4^l/2$. In the limit $l \gg 1$, the MQC distribution can be well approximated by a Gaussian function. [1]

The Gaussian distribution is often used as a starting point to analyze observed I_q from MQC experiments on 3-dimensional spin netowrks such as $\mathrm{CaF_2}$ and Adamantaine [27, 107, 17] where the phenomological model is expected to be valid. However it has been pointed out that in some cases an exponential distribution is a better fit to the experimental data [87]. Never mind the exact MQC distribution, one can always use the second moment $\sum_q q^2 I_q$ to characterize the spread of a discrete MQC spectrum I_q. The second moment is a measure of the average number of correlated spins in the system. In a pioneering work the width of the MQC distribution is used to distinguish between localized and delocalized dynamics in adamantane [6, 7]. In Chapter 4, it will be shown that the second moment of the MQC distribution is the out-of-time ordered commutator for a system at effectively infinite temperature.

---

[1] For an alternative derivation of Eq. (1.19), start by writing $\mathcal{O} = \sum_{jk} \mathcal{O}_{jk} |j\rangle\langle k|$, where $|j\rangle$, $|k\rangle$ are eigenvectors of P and $\mathcal{O}_j k = \langle j| \mathcal{O} |k\rangle$. For $P = \sum_j S_z^j$, each $|j\rangle$ is a tensor product of a string of $|\uparrow\rangle$ and $|\downarrow\rangle$ states. Under rotation by P: $e^{-i\phi P}\mathcal{O}e^{i\phi P} = \sum_{jk} \mathcal{O}_{jk} e^{-i\frac{j_+ - j_- - k_+ - k_-}{2}\phi} |j\rangle\langle k|$, where $j_\pm$ and $k_\pm$ are the number of $|\uparrow\rangle$ and $|\downarrow\rangle$ in $|j\rangle$ and $\langle k|$ respectively. Using $j_+ + j_- = k_+ + k_- = l$, it can be shown that $e^{-i\phi P}\mathcal{O}e^{i\phi P} = \sum_{jk} \mathcal{O}_{jk} e^{-i(j_+ - k_+)\phi} |j\rangle\langle k|$, here the phase acquired $e^{i(j_+ - k_+)\phi}$ is the coherence between $|j\rangle$ and $|k\rangle$. Since only terms satisfying $j_+ - k_+ = q$ contribute to $\mathcal{O}_q$ and I_q. Eq. (1.19) is recovered by summing over all possibilities: $\sum_{j_+ - k_+ = q} \binom{l}{j_+}\binom{l}{k_+} = \sum_{j_+ = 0}^{l} \binom{l}{j_+}\binom{l}{q + j_+} \propto \frac{\Gamma(2l+1)}{\Gamma(l+1-q)\Gamma(l+1+q)}$.

1.3.3 MQC Intensities for Random Matrices

Intuitively, one expects the phenomenological model to be accurate for random matrices. In order to numerically assess the validity of Eq. (1.19) for random Hermitian matrices, consider a random Hermitian matrix drawn from either a Gaussian orthogonal ensemble (GOE): $\mathcal{O}_{\mathrm{GOE}}$, or a Gaussian unitary ensemble (GUE): $\mathcal{O}_{\mathrm{GUE}}$. $\mathcal{O}_{\mathrm{GOE}}$ are real symmetric random matrices and are thus time-reversal invariant. Let $\overline{\mathcal{O}}_{\mathrm{GOE/GUE}}$ be the normalized traceless part of $\mathcal{O}_{\mathrm{GOE/GUE}}$:

$$\overline{\mathcal{O}}_{\mathrm{GOE/GUE}} = \frac{\mathcal{O}_{\mathrm{GOE/GUE}} - \mathrm{Tr}(\mathcal{O}_{\mathrm{GOE/GUE}})\mathbb{1}/2^L}{\|\mathcal{O}_{\mathrm{GOE/GUE}} - \mathrm{Tr}(\mathcal{O}_{\mathrm{GOE/GUE}})\mathbb{1}/2^L\|}$$

so that $\|\overline{\mathcal{O}}_{\mathrm{GOE/GUE}}\| = 1$. Fig. 1-2 shows the MQC intensities encoded along the z-axis for $\overline{\mathcal{O}}_{\mathrm{GOE/GUE}}$ averaged over 10 disorder realizations for $L = 10$ spins. Both $\overline{\mathcal{O}}_{\mathrm{GOE/GUE}}$ are drawn from distribution of unit variance. The red circles in Fig. 1-2 corresponds to Eq. (1.19). Interestingly the phenomelogical model gives almost perfect agreement to the MQC intensities for random matrices.

1.3.4 MQC Intensities for Chaotic Hamiltonian

One immediate question is whether MQC intensities will follow Eq. (1.19) for generic interacting many-body systems. At first sight the answer seems to be no. Consider for instance the MQC intensities for operator $S_z^j(t) = e^{-iHt}S_z^j e^{iHt}$ encoded with respect to some P, with $[P, H] \neq 0$ and $[S_z^j, H] \neq 0$. This time-dependent operator, however, will never evolve into a random matrix, regardless of how long t is. Since time

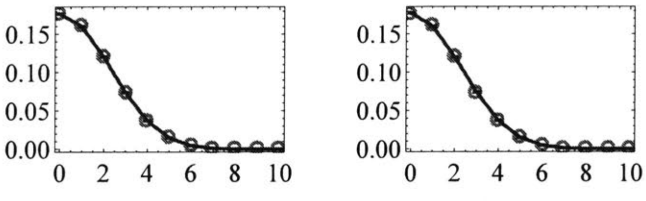

Figure 1-2: **Comparison of MQC intensities given by Eq.(1.19) and that of random matrices** Left: MQC intensities averaged over 10 realizations of random matrices drawn from GOE. Right: same as left except drawn from GUE. Red circles are from Eq.(1.19).

evolution is an unitary transformation, the eigenvalues of $S_z^j(t)$ stays $\pm 1/2$ independent of t, and thus can never exhibit level repulsion as required in random matrices [111]. Interestingly, numeric simulations show that certain interacting 1-dimensional Hamiltonians still follows Eq. (1.19) at large t. Consider for example the Ising model with both transverse and longitudianl fields [79]:

$$H_{\text{Ising}} = \sum_j (\sigma_x^j \sigma_x^{j+1} + g\sigma_y^j + h\sigma_x^j) \tag{1.20}$$

where $\sigma_j^{x,y,z}$ are the Pauli matrices at the j-th site. This model is known to be ergodic, or quantum chaotic, for generic values of g and h. Following [79, 80], let $g = 0.9045$ and $h = 0.8090$ and use periodic boundary conditions (PBC). Fig. 1-3 shows the MQC intensities encoded along the z-axis for the operators $\sigma_z^1(t)$, $\sum_j \sigma_z^j(t)$, and $\sum_j \sigma_z^j \sigma_z^{j+1}(t)$ at $t = 10^5$. Good agreements are found between the exactly calculated MQC spectrum with the phenomenological model given by Eq. (1.19), even though the operators are not random matrices.

According to the eigenstate thermalization hypothesis (ETH), generic many-body eigenstates are thermal, where the local reduced density operator can be described by a thermal equilibrium distribution with inverse temperature depending only on the energy of the eigenstate [123, 138, 61]. Systems satisfying ETH exhibit quantum ergodicity, where individual eigenstates can "sample" all accessible Hilbert space evenly. Consider the density matrix of a single eigenstate $|\psi\rangle$: $\rho = |\psi\rangle\langle\psi|$. If $|\psi\rangle$ is ergodic, one expects ρ to contain evenly all possible types of spin correlations, Fig. 1-4 shows the MQC intensites encoded along z-axis averaged over all 2^L eigenstates. The

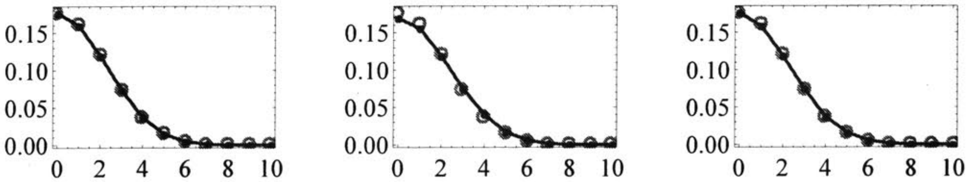

Figure 1-3: **MQC intensities of local operators in chaotic Ising model** Calculated MQC intensities encoded along z-axis for $\sigma_z^1(t)$(left), $\sum_j \sigma_z^j(t)$(middle), and $\sum_j \sigma_z^j \sigma_z^{j+1}(t)$(right) at $t = 10^5$. Red circles are predictions of Eq. (1.19).

results are in good agreement with Eq. (1.19). Ref. [80] shows that in this model, all eigenstates tends to be thermal as system size is increased, indicating ETH in the strong sense: every eigenstate in a quantum ergodic system is thermal.

Notice that the operators chosen for Fig. 1-3 and the encoding axis ($\sum_j S_z^j$) do not have any overlap with the chaotic Ising Hamiltonian. From numerics it is found that when significant overlap is present the phenomenological model is not valid.

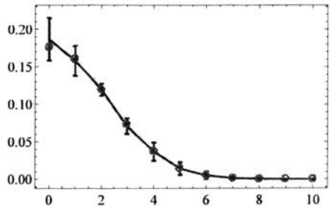

Figure 1-4: **MQC intensities of all eigenstates in chaotic Ising model** Calculated MQC intensities encoded along z-axis averaged over all 2^L eigenstates, the error bars correspond to the standard deviation. Red circles are from Eq. (1.19).

1.4 Flurapatite Crystals, a Quasi-one dimensional spin system

The system used in the experiment for this thesis is a single crystal of fluorapatite (FAp) shown in Figure 1-1(A). Fluorapatite is a hexagonal mineral with space group $P6_3/m$, with the ^{19}F spin-1/2 nuclei forming linear chains along the c-axis. Each fluorine spin in the chain is surrounded by three ^{31}P spin-1/2 nuclei. The sample is placed at room temperature inside an NMR superconducting magnet producing a uniform $B = 7$ T field. The total Hamiltonian of the system is given by

$$H_{tot} = \omega_F \sum_k S_z^k + \omega_P \sum_\kappa s_z^\kappa + H_F + H_P + H_{FP} \tag{1.21}$$

The first two terms represent the Zeeman interactions of the F(S) and P(s) spins, respectively, with frequencies $\omega_F = \gamma_F B = (2\pi)282.37$ MHz and $\omega_P = \gamma_P B = (2\pi)121.51$ MHz, where $\gamma_{F/P}$ are the gyromagnetic ratios. The other three terms represent the secular magnetic dipole-dipole interaction among the spins, given by

$$H_F = \frac{1}{2}\sum_{j<k} J^F_{jk}(2S^j_z S^k_z - S^j_x S^k_x - S^j_y S^k_y) \qquad H_P = \frac{1}{2}\sum_{\lambda<\kappa} J^P_{\kappa\lambda}(2s^\lambda_z s^\kappa_z - s^\lambda_x s^\kappa_x - s^\lambda_y s^\kappa_y) \quad (1.22)$$

and the heteronuclear interaction between the F and P spins,

$$H_{FP} = \sum_{k,\kappa} J^{FP}_{k,\kappa} S^k_z s^\kappa_z, \qquad (1.23)$$

where S^j_n (s^j_n) represents the n component of a Fluorine (Phosphorus) spin Pauli operator on site j. The maximum values of the couplings (for the closest spins) are given respectively by $J^F = -32.76$ krad s^{-1}, $J^P = 1.21$ krad s^{-1} and $J^{FP} = 6.13$ krad s^{-1} when crystal is oriented with its c-axis parallel to the external magnetic field. In this orientation, the coupling of fluorine spins to the closest off-chain fluorine spin is ≈ 40 times weaker, while in-chain, next-nearest neighbor couplings are 8 times weaker. Previous studies on these crystals have indeed observed dynamics consistent with spin chain models, and the system has been proposed as solid-state realizations of quantum wires [23, 25, 119]. This approximation of the experimental system to a 1D, shortrange system, although not perfect has been shown to reliably describe experiments for relevant time-scales [127, 151]. The approximation breaks down at longer time, with a convergence of various effects: long-range in-chain and cross chain couplings, as well as pulse errors in the sequences used for Hamiltonian engineering. In addition, the system also undergoes spin relaxation, although on a much longer time-scale ($T_1 = 0.8$ s for our sample).

Chapter 2

Localization in spin chains

2.1 Introduction

Anderson first demonstrated that single particle wave functions can become exponentially localized in the presence of disorder [9]. Whether this localization [143, 20, 124] survives in the presence of interactions (many-body localization, MBL) has received much attention in recent years [15, 14, 109, 136, 130, 28]. Numerical evidence in spin chains indicates that the system may be in the MBL or ergodic phase depending on the relative strength of interaction and disorder [112, 132, 97]. MBL can be distinguished from its noninteracting counterpart (Anderson Localization, AL) via the dynamics of entanglement entropy [67, 13, 131, 65]. Entanglement entropy is however difficult to evaluate experimentally, and so far has only been measured on systems with small number of particles [70]. One way to circumvent this challenge, is to measure entanglement witnesses such as the quantum fisher information (QFI), which can serve as a lower bound for entanglement entropy [136] for pure states.

A remarkable feature about the MBL phase is that it is predicted to persist at high and even infinite temperature [111], where states are highly mixed and there is little to no entanglement present. How does one characterize the MBL phase experimentally in such a system? Here we introduce a novel metric capable of distinguishing MBL from AL in the non-equilibrium dynamics of highly mixed states, and provide both numerical and experimental evidence in support of the metric. Our approach

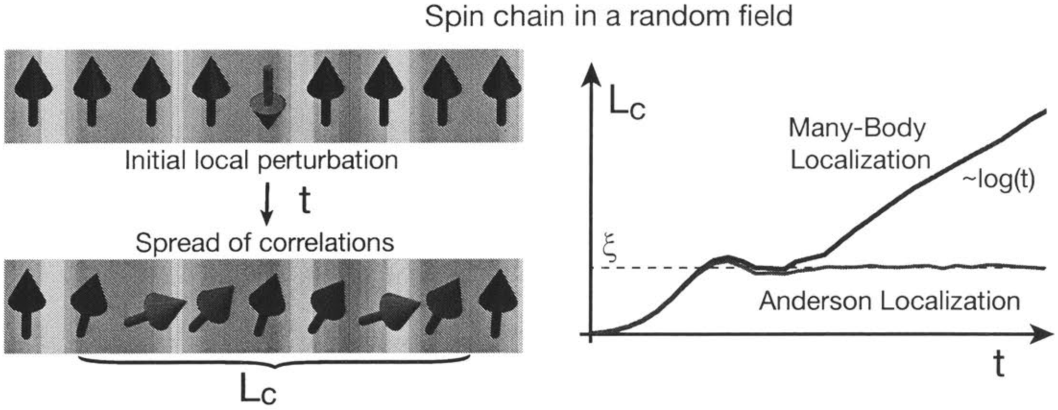

Figure 2-1: Quantum many-body correlations grow from an initial localized state (top) but are restricted to a finite size by disorder (bottom). The average correlation length L_c, which measures the spread of the correlations, is observed to saturate at the localization length ξ in the case of AL, but grows logarithmically with time in the MBL regime.

requires no local control of the system, and relies only on collective rotations and measurements, in contrast to recently proposed metrics [50] that also detect the spread of correlations but require single-spin addressability. The experimental system is composed of nuclear spins in a natural crystal coupled by the magnetic dipolar interaction. While the system is a 3D, open quantum system with long-range interactions, it has been shown that on timescales of relevance to the experiments it can mapped with high-fidelity to an ensemble of 1D, nearest-neighbor coupled spin chains [151, 23]. We exploit Hamiltonian engineering techniques to selectively introduce and tune both the strength of the interaction and the degree of disorder in the system, and measure the growth of many-spin correlations in both the AL and MBL regimes.

2.2 Average Correlation Length

We consider a linear chain of L spins initially at equilibrium at high temperature ($\beta \to 0$) in a strong magnetic field aligned along the $\hat{z}$ direction. Under these conditions, the thermal equilibrium state of the system can be expressed as $\rho_{\text{eq}} = (\mathbb{1} - \epsilon \sum_j S_z^j)/2^L$ (with S the spin-1/2 operator) to first order in $\epsilon = \beta\omega_L \ll 1$, where ω_L is the spin Zeeman energy and $\hbar = 1$. Any spin-spin interactions are assumed to be negligible compared to the Zeeman energy, so that the initial interaction Hamiltonian commutes with the thermal equilibrium state.

If the effective interaction Hamiltonian H of the system is changed suddenly (a rapid quench), the system is no longer in equilibrium and evolves into a many-body correlated state. The presence of disorder hinders the growth of correlations and can give rise to localized states, characterized by an exponentially decreasing probability of correlations outside a typical localization length, ξ, as shown in Figure 2-1. Inspired by this picture, we define a metric of localization that measures the average length over which correlations have developed. We can generically write the high-temperature time-evolved density matrix as

$$\rho(t) = \frac{\mathbb{1}}{2^L} - \frac{\epsilon\sqrt{L}}{2^L}\sum_{k=1}^{L}\sum_{s=1}^{\zeta_k} b_k^s(t)\mathcal{B}_k^s, \tag{2.1}$$

where $\mathcal{B}_k^s$ are operators composed of tensor products of k Pauli matrices and $L-k$ identity operators. Here ζ_k is the number of configurations with exactly k non-identity Pauli operators.

To quantify localization we define the ***average correlation length***

$$L_c = \sum_{k=1}^{L} k f_k, \tag{2.2}$$

where $f_k = \sum_{s=1}^{\zeta_k}[b_k^s]^2$ is the contribution of all possible spin correlations with Hamming weight k (with $\sum_{k=1}^{L} f_k = 1$).

In the initial equilibrium state ρ_{eq} there are no spin correlations and $L_c = 1$. In the absence of disorder, we expect L_c to grow and eventually saturate at a value dependent on L. In the presence of disorder, if the system is noninteracting, AL leads to a coherent suppression of many-spin correlations and L_c is bound by the localization length ξ. When interactions are present, disorder is unable to completely suppress the correlation growth. The slow growth of L_c in the presence of interactions is the key feature that enables L_c to distinguish between AL and MBL for mixed states.

Consider an effective spin Hamiltonian (following the quench) of the form

$$\begin{aligned} H = & \frac{u+v}{2} \sum_{j=1}^{L-1} J S_x^j S_x^{j+1} + \frac{v-u}{2} \sum_{j=1}^{L-1} J S_y^j S_y^{j+1} \\ & + g \sum_{j=1}^{L} h_j S_z^j - v \sum_{j=1}^{L-1} J S_z^j S_z^{j+1}, \end{aligned} \tag{2.3}$$

The first two terms represent an integrable Hamiltonian, as via a Jordan-Wigner transformation [71] they map to a free fermionic Hamiltonian. The third term corresponds to on-site disorder, and the last term introduces interactions between fermions. Tuning the relative strength of these parameters allows us to explore different physical regimes. Figure 2-2 shows that the entropy $S = -\mathrm{Tr}[\rho_L \log \rho_L]$, where ρ_L is the reduced density matrix of the left half of the chain, displays a characteristic logarithmic growth in time [13] when the system enters the MBL phase, and saturates when the system is non-interacting. The figure also shows that for the initial equilibrium state ρ_{eq}, L_c also saturate at long times when the system is noninteracting and increases logarithmically when a weak interaction is introduced. This suggests that L_c can be used as an alternative to entanglement entropy to distinguish MBL from AL for mixed states.

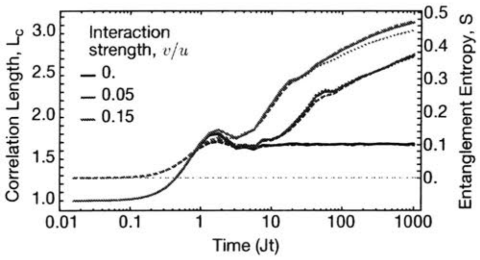

Figure 2-2: **Simulations of spin correlation and entanglement entropy.** We compare the entropy of the reduced half chain (dotted lines, right axis) with the correlation length L_c (solid lines, left axis) and the approximate L_c obtained from measuring the MQC (dotted lines). Simulations were performed for $L = 8$ and with a uniform random noise $gh_j/u \in [-8, 8]$ for 960 realizations. The similar behavior (including logarithmic growth) confirm that the chosen metric is as good an indicator of MBL as the more commonly used entanglement entropy. Here we show a scaled representation of the entanglement entropy, renormalized to vary between 0 and 1, in order to account the mixed initial state of the system.

2.2.1 Average Correlation Distance

In the main text we focused on the average correlation length as the chosen metric to experimentally detect the MBL phase. Here we introduce a second metric, that we call the ***average correlation distance*** that can serve the same purpose and it is even more closely related to the notion of localization length. We will then compare these two metrics to known measures of localization in Sec. 2.7.

In Eq. (1) we decomposed the time-dependent density matrix using operators $\mathcal{B}_k^s$ composed of tensor products of k Pauli matrices and $L-k$ identity operators. An alternative decomposition is

$$\rho(t) = \frac{\mathbb{1}}{2^L} - \frac{\epsilon\sqrt{L}}{2^L}\sum_{k=1}^{L}\sum_{j=1}^{L+1-k}\sum_{r=1}^{\xi_k} a^r_{j,j+k-1}(t)\mathcal{A}^r_{j,j+k-1}, \tag{2.4}$$

where $\mathcal{A}^r_{j,j+k-1}$ represents an operator composed of tensor products of Pauli matrices where the two farthest nonidentity operators are located at sites j and $j+k-1$; for each k there are ξ_k such configurations labeled by r.

We can then define the ***average correlation distance*** over which spin correlations have established in the system:

$$D_c = \sum_{k=1}^{L} k d_k. \tag{2.5}$$

Here $d_k = \sum_{j=1}^{L+1-k}\sum_{r=1}^{\xi_k}[a^r_{j,j+k-1}]^2$ is the contribution of all possible spin correlations over distance k, and satisfies the normalization $\sum_{k=1}^{L} d_k = 1$. D_c is a measure of how far information has spread within the system.

We expect D_c to have a qualitatively similar behavior to L_c, as indeed it is even more closely related to the notion of localization length. However, measuring d_k and D_c is challenging, since for a generic many-body spin Hamiltonian the number of configurations ξ_k is exponential in k and L. In addition, we cannot rely on the measurable MQC intensities to extract d_k. Indeed, since collective rotations cannot distinguish correlations such as $S_x^1 S_x^2$ and $S_x^1 S_x^5$, it is impossible to separate their contributions into d_2 and d_5, even if they can be correctly classified when measuring f_2. We find however that for noninteracting systems, and for simple initial states such as ρ_{eq}, all many-spin correlations are in the form $\mathcal{A}_k = \mathcal{B}_k \sim S_a^j(\prod_{l=j+1}^{k+j-2} S_z^l)S_b^{k+j-1}$, where the end spins $S_{a,b}$ are either S_x or S_y. Then, in these systems a spin correlation established over distance k corresponds to a correlation amongst k spins, thus the average distance D_c can be alternatively understood as the average number of correlated spins, that is, the average correlation length L_c. While for noninteracting systems, $f_k = d_k$ and consequently $L_c = D_c$, for interacting systems the two metrics are different, but they are equally good correlation metrics in distinguishing MBL from AL. Finally, we remark that in higher dimensions, D_c is not unique since there are different ways to label the spins, thus making L_c a more versatile correlation metric than D_c in more than 1 dimensions.

2.3 Experimental Results

Measuring L_c for a generic many-body state is challenging, since it is usually difficult to directly measure many-body correlations to determine f_k, and the number of configurations ζ_k is exponential in k and L. Here we show how to extract L_c in our experiments, with a method that can be extended to other systems.

While the high-temperature thermal equilibrium state does not evolve under this natural dipolar Hamiltonian, we can quench the system to a different effective Hamiltonian of the form of Equation (2.3) by periodically applying a radiofrequency pulse sequence in resonance with the F spins. This method (called Coherent Averaging [54]) has been long used in the NMR literature for spectroscopy and condensed matter studies. Here we further push these techniques to engineer a broad class of Floquet (periodic) Hamiltonians with tunable disorder and interactions. In addition, we are also able to reverse the arrow of time, a tool that allows measuring out-of-time ordered correlations (OTOC). The experimentally adjustable parameters u, v, and g allow us to explore various regimes of interest. The Experimental Method section shows the pulse sequence used to implement this effective Hamiltonian.

In order to calculate the correlation length L_c we need to find the coefficients f_k, which we can determine experimentally by borrowing from well-known NMR techniques that approximate the number of correlated spins by their quantum coherence number [106]. Multiple quantum coherence (MQC) intensities of order q describe the contribution of terms $|m_a\rangle\langle m'_a|$ in the density matrix such that $m_a - m'_a = q$, with m_a the collective S_a eigenvalue (typically $a = z$). MQC intensities I_q can be measured by relying on their distinct behavior under collective rotations [106, 17, 120]. The distribution of I_q has been traditionally used to approximate the average number of correlated spins, or cluster size, in 3-D spin networks [18, 108, 7]. While this approximation fails in 1-D systems, we find instead a practical experimental protocol to *exactly* measure L_c for noninteracting systems. The protocol still yields a very good approximation for disordered interacting (MBL) systems.

We first note that in non-interacting systems, for simple initial states such as ρ_{eq} the number of configurations is simply $\zeta_k \propto L - k$: All many-spin correlations are of the form $\mathcal{B}_k^s \sim S_a^s(\prod_{l=s+1}^{k+s-2} S_z^l) S_b^{k+s-1}$, where the end spins $S_{a,b}$ are either S_x or S_y. This structure is key to extracting the f_k coefficients, as correlations with different k will respond differently when rotated around an appropriate axis. In our MQC protocol, we first decompose $\rho(t)$ into four orthogonal sectors using time-reversal and phase cycling [21] and then measure the MQC intensities encoded in the x axis for each j^{th} sector, I_q^j. The resulting MQC intensities can be related to f_k in Eq. (2.2) by a linear transformation, $f_k = \sum_{jk} M_{kq}^{(j)} I_q^j$, and from the extracted f_k we can calculate L_c. While this protocol was designed for the Hamiltonian we investigated, similar strategies will be available for other integrable Hamiltonians, with a proper choice of the axes along which the MQC are measured.

As long as the interaction term is not too large (and disorder large enough) we expect that the evolved density matrix state will still mostly contain the simpler many-spin correlations described above, thus allowing to extract an approximate L_c. The validity of this argument can be seen from the simulation results shown in Fig. 2-2, where the approximated L_c (calculated from the MQC) continues to closely track the exact L_c and the entanglement entropy in the MBL phase.

Combining Hamiltonian engineering with MQC readout, we can explore the behavior of both noninteracting and interacting models in the presence of disorder. Fig. 2-3 shows the experimentally extracted L_c for our interacting model, as compared to the non-interacting case.

The figure also shows the behavior of L_c as the strength of the interactions (v in Eq. 2.3) are varied, for a fixed disorder strength. The experiments clearly reveal the emergence of slow growth in L_c when interactions are added, the hallmark feature of MBL [13, 115]. For the noninteracting Hamiltonian ($v = 0$), in the absence of disorder

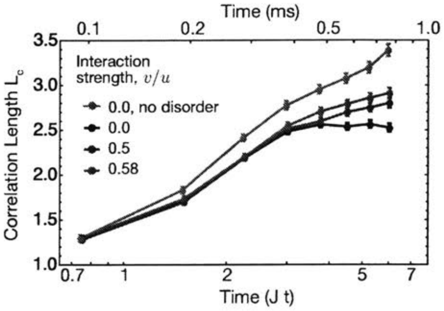

Figure 2-3: **Experimental measurements of spin correlations in interacting spin chains.** We plot in log-linear scale the measured L_c dynamics in the presence of disorder and for varying interaction strengths v. Data are for $u = 0.24$ and $g = 0.12$. After an initial growth of correlations, L_c saturates for the non-interacting systems, while it shows a slow growth in the presence of interactions, thus indicating many-body localization. In contrast, the integrable case (gray, $v = 0$, $g = 0$) shows more pronounced growth, although it is still limited by experimental imperfections.

we expect L_c to increase linearly, consistent with the Lieb-Robinson bound for short-ranged Hamiltonians [92]. In the thermodynamic limit $L \to \infty$ and at large times $uJt \gg 1$, L_c grows with a velocity $V = 2uJ/\pi$. In the presence of disorder, instead, we expect L_c to initially increase, as spins correlate within the localization length, and to saturate at long times due to AL. This experimental evidence proves that our Hamiltonian engineering technique can indeed introduce disorder in the system evolution.

Figure 2-4 illustrates the change in L_c as a function of disorder strength for the non-interacting case. Increasing disorder is clearly seen to result in a saturation of L_c, consistent with Anderson Localization. The lines are numerical simulations using 6 (solid), 10 (dotted) and 20 (dashed) spins respectively, demonstrating that our experimental results are indeed consistent with theoretical predictions. The discrepancies seen at higher L_c are likely due to experimental errors.

Control imperfection and decoherence due to the open system dynamics can preferentially affect the higher quantum coherences of large spin correlations, leading to an apparent saturation of L_c. The same experimental imperfections make it even more difficult to observe the ergodic phase, where interactions dominate disorder. High-fidelity experimental control of complex many-body states is key for any experimental metric of complexity. In some cases, it is still possible to distinguish between the saturation of L_c due to experimental limitations at long time and its quenching due to increasing disorder using additional symmetry properties of the MQCs.

Note that in the experiments we can probe this dynamics only for relatively short times, where the physical system is a good approximation to the ideal model [151]. Indeed, while the chain lengths are much longer than explored on these timescales, we have a 3-D crystal where each spin chain interacts with 6 surrounding chains and the couplings are long-range, $\propto 1/r^3$. Thus, we kept the experimental time short to minimize these effects, as well as pulse imperfections that can lead to unwanted terms in the engineered Hamiltonian (the time is also much shorter than the relaxation time $T_1 \approx 0.8$ s and the P dynamics).

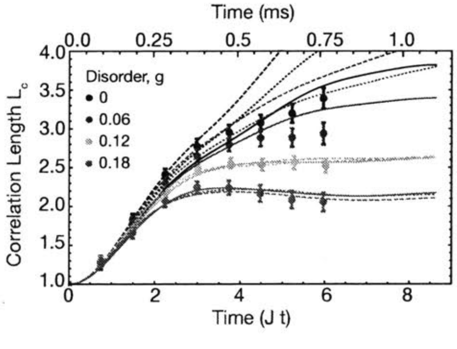

Figure 2-4: **Experimental spin correlations in noninteracting spin chains.** Correlation length L_c for various strength $\propto g$ of disordered transverse fields, with $u = 0.24$ and $v = 0$ (see Eq. 2.3). Errorbars are determined from the noise in the free induction decay, the solid lines are guides to the eye. The lines are numerical simulations using 6 (solid), 10 (dotted) and 20 (dashed) spins respectively, averaged over 126 disorder realizations.

We can obtain a more intuitive understanding of why our experimental method for extracting the correlation length from MQC works in a quite robust way. In the integrable case, where both the initial state and the Hamiltonian can be mapped into free fermions, only a restricted set of operators $\mathcal{B}_k^r$ appear in the dynamics and we can exactly measure their contribution to L_c via the MQC. This method can still be applied to MBL systems due to their *emergent integrability* characterized by a complete set of local integrals of motions (LIOM) [131, 65]. While the number of possible configurations ζ_k in these LIOMs is exponential, only a fraction of them (corresponding to small k) have significant weights – a consequence of area law entanglement in MBL systems [37, 16]. Then, when applied to MBL systems, the MQC method approximately counts the L_c of these interacting LIOMs, while still exhibiting the same logarithmic growth as entanglement entropy. We can further understand our measurement in terms of out-of-time ordered correlations [64, 47, 90]. As explained in Chapter 1, in order to extract the MQC intensities we effectively measure the quantities

$$\begin{aligned} S_\phi(t) =& \mathrm{Tr}\left[\rho_{\mathrm{eq}}\Phi^\dagger(t)\rho_{\mathrm{eq}}\Phi(t)\right], \\ \text{with} \quad & \Phi(t) = U(t)e^{i\phi\sum_j S_x^j}U^\dagger(t). \end{aligned} \tag{2.6}$$

While we can only measure OTOC for collective operators on the whole system, such as Φ, these OTOC still give some information about the spreading or localization of correlations, since ρ_{eq} is a sum of local operators. The information is made more accurate as we consider an average of several OTOC for different $\Phi(0)$ operators, even if we cannot measure a whole basis of a subsystem as required to extract the entropy [62, 64, 43]. It will be interesting to experimentally measure other OTOC in our system, as OTOC has been studied in the context of information scrambling in black holes [139, 146].

In our experimental analysis, we mapped the physical system to the simple, nearest-neighbor 1D spin chain model. This allowed us to analyze the data with a well-known model, that furthermore leads to analytical solutions at least for the non-interacting case. However, it would be interesting to further analyze if the discrepancies from the ideal model, and in particular long-range interactions, give rise to further, interesting properties when exploring the systems for times where the approximation is no-longer as good. For example, the expected slow growth of entanglement in long-range coupling systems is expected to exhibit a power-law [115], instead of a logarithmic growth, while the question of whether localization can be seen in long-range, higher-dimensional systems is still open.

2.4 Fermionic Solution to Noninteracting Systems

In order to show how f_k and L_c can be extracted from MQC intensities, we need to first present a microscopic description of the spin-correlations generated by the Hamiltonian. In the main text, we introduce the generic (Floquet) Hamiltonian that we can experimentally generate with our control (see Eq. (3)),

$$\begin{aligned} H = &\frac{1}{2}\sum_{j=1}^{L-1} uJ(S_x^jS_x^{j+1} - S_y^jS_y^{j+1}) + b\sum_{j=1}^{L} S_z^j + g\sum_{j=1}^{L} h_jS_z^j \\ &+ \frac{1}{2}\sum_{j=1}^{L-1} vJ(S_x^jS_x^{j+1} + S_y^jS_y^{j+1} - 2S_z^jS_z^{j+1}) \end{aligned} \tag{2.7}$$

We can rewrite the spin Hamiltonian H in terms of fermion operators using a Jordan-Wigner transformation [71]: $c_j = \sigma_-^k \prod_{k<j} \sigma_z^j$, where σ are the usual Pauli operators:

$$\begin{aligned} H = &-\frac{uJ}{4}\sum_{j=1}^{L-1}(c_j^\dagger c_{j+1}^\dagger + c_{j+1}c_j) + \frac{b}{2}\sum_{j=1}^{L}(2c_j^\dagger c_j - 1) + \frac{g}{2}\sum_{j=1}^{L} h_j(2c_j^\dagger c_j - 1) \\ &-\frac{vJ}{4}\sum_{j=1}^{L-1}(c_j^\dagger c_{j+1} + c_{j+1}^\dagger c_j) - \frac{vJ}{4}\sum_{j=1}^{L-1}(2c_j^\dagger c_j - 1)(2c_{j+1}^\dagger c_{j+1} - 1). \end{aligned} \tag{2.8}$$

In particular, this makes it apparent that only the last term of the equation corresponds to interactions. Note that we consider the case $b = 0$ in the main text.

The dynamics of the noninteracting Hamiltonian (ignoring the $\sum_j S_z^jS_z^{j+1}$ term) $H = uJ\sum_j(S_+^jS_+^{j+1} + S_-^jS_-^{j+1}) + vJ\sum_j(S_+^jS_-^{j+1} + S_-^jS_+^{j+1}) + g\sum_j h_jS_z^j + b\sum_j S_z^j$ can be solved by mapping the system into a chain of spinless fermions [71, 44, 23]. The initial state is given by the equilibrium state at high temperature; since the dominant component of the Hamiltonian is the Zeeman interaction, $H_Z = \omega_0 Z$, with $Z = \sum_j S_z^j$, the thermal equilibrium state can be well approximated by $\rho_{\text{eq}} \approx e^{-\beta\omega_0 Z} \approx \frac{1}{2^L}(\mathbb{1} - \epsilon Z)$, with $\epsilon = \beta\omega_0$. The time-dependent component of the density matrix $\delta\rho(t) \propto U\rho_{\text{eq}}U^{\dagger} - \mathbb{1}/2^L$ evolves as

$$\begin{aligned}\frac{1}{\sqrt{L}}\delta\rho =& \sum_j 2\mu_{jj}(t)S_z^j + \sum_{j,k>j} 2^{k-j+1}\left[-\mu_{jk}(t)\left(S_x^jS_x^k + S_y^jS_y^k\right) - \eta_{jk}(t)\left(S_x^jS_x^k - S_y^jS_y^k\right)\right.\\ &\left. +\nu_{jk}(t)\left(S_y^jS_x^k + S_x^jS_y^k\right) + \chi_{jk}(t)\left(S_y^jS_x^k - S_x^jS_y^k\right)\right] \prod_{j<l<k} S_z^l,\\ =& \sum_j 2\mu_{jj}S_z^j + \sum_{j,k>j} 2^{k-j+1}\left[-(\mu+\eta)_{jk}S_x^jS_x^k - (\mu-\eta)_{jk}S_y^jS_y^k\right.\\ &\left. +(\nu+\chi)_{jk}S_y^jS_x^k + (\nu-\chi)_{jk}S_x^jS_y^k\right] \prod_{j<l<k} S_z^l, \end{aligned} \tag{2.9}$$

where μ is real and symmetric, whereas χ, η, ν are real and antisymmetric; they correspond to the four possible ways to correlate spins in the noninteracting system as shown above. In terms of these matrices f_k can be expressed as

$$f_1 = \bar{\mu}_0, \qquad f_{k>1} = 2(\bar{\mu}_{k-1} + \bar{\chi}_{k-1} + \bar{\eta}_{k-1} + \bar{\nu}_{k-1}), \tag{2.10}$$

where $\bar{\mu}_k = \sum_j \mu_{jj+k}^2$, and similar expressions hold for χ, η, and ν. Once f_k is found, the correlation length can be calculated as $L_c = \sum_k k f_k$. Notice that in the noninteracting system the average correlation length is exactly equal to the average correlation distance, i.e., $f_k = d_k$ and $L_c = D_c$. Analytical expressions for these two quantities can be obtained in some limiting cases. For instance, let $u = 1$, $v = g = 0$, and consider the double quantum Hamiltonian: $H_{\text{dq}} = J\sum_j(S_+^jS_+^{j+1} + S_-^jS_-^{j+1}) + b\sum_j S_z^j$. We can rewrite H_{dq} in terms of fermion operators using the Jordan-Wigner transformation,

$$H_{\text{f}} = -\frac{J}{4}\sum_j(c_j^{\dagger}c_{j+1}^{\dagger} + c_{j+1}c_j) + \frac{b}{2}\sum_j(c_j^{\dagger}c_j - c_jc_j^{\dagger}),$$

where the fermion operators satisfy $\{c_j^\dagger, c_k\} = \delta_{jk}$, $\{c_j, c_k\} = \{c_j^\dagger, c_k^\dagger\} = 0$. Next we perform a modified Fourier transformation given by $c_j^\dagger = (-i)^j \sqrt{\frac{2}{L+1}} \sum_q \sin\left(\frac{jq\pi}{L+1}\right) d_q^\dagger$, and write the Hamiltonian in momentum space as

$$H_{\mathrm{f}} = \frac{1}{2}\sum_q \begin{pmatrix} d_q^\dagger & d_{\bar{q}} \end{pmatrix} \begin{pmatrix} b & -iJ_q/2 \\ iJ_q/2 & -b \end{pmatrix} \begin{pmatrix} d_q \\ d_{\bar{q}}^\dagger \end{pmatrix},$$

where $\bar{q} = L + 1 - q$, and $J_q = J\cos\left(\frac{q\pi}{L+1}\right)$. Instead of using a Bogoliubov transformation to diagonalize the matrix, we use Heisenberg's equation of motion to directly obtain the dynamics of each pair of modes,

$$\begin{pmatrix} d_q(t) \\ d_{\bar{q}}^\dagger(t) \end{pmatrix} = \exp[-i(b\sigma_z + J_q\sigma_y/2)t] \begin{pmatrix} d_q \\ d_{\bar{q}}^\dagger \end{pmatrix}$$

$$= \begin{pmatrix} \cos(\omega_q t) - i\cos\theta_q \sin(\omega_q t) & -\sin\theta_q \sin(\omega_q t) \\ \sin\theta_q \sin(\omega_q t) & \cos(\omega_q t) + i\cos\theta_q \sin(\omega_q t) \end{pmatrix} \begin{pmatrix} d_q \\ d_{\bar{q}}^\dagger \end{pmatrix}$$

where $\omega_q = \sqrt{b^2 + J_q^2/4}$, $\cos\theta_q = b/\omega_q$, and $\sin\theta_q = J_q/2\omega_q$. Note that d_q represents a fermion operator in momentum space, it is not to be confused with d_k in Eq. (2.5). In the thermodynamic limit ($L \to \infty$), the correlation length in the absence of any transverse field ($b = 0$) can be expressed as

$$L_c = \sum_{k=1}^{\infty} k f_k = 1 + J^2t^2[\mathcal{J}_0^2(Jt) + \mathcal{J}_1^2(Jt)] - Jt\mathcal{J}_0(Jt)\mathcal{J}_1(Jt), \tag{2.11}$$

where $\mathcal{J}_k$ is the k-th Bessel function of the first kind. At long times $Jt \gg 1$, L_c has the asymptotic form $L_c \sim 2Jt/\pi$. This shows that the average spread of correlations in the noninteracting spin chain has a light-cone like behavior. When $b \neq 0$, L_c cannot be expressed analytically. In the regime $J \ll b$, we can approximate L_c as a series expansion in powers of J/b. The first two terms are given by

$$L_c = 1 + \frac{J^2}{4b^2}\left[\frac{1}{2} + \frac{1}{2}\mathcal{J}_0^2\left(\frac{J^2t}{8b}\right) - \mathcal{J}_0\left(\frac{J^2t}{8b}\right)\cos\left(2bt + \frac{J^2t}{8b}\right) + \mathcal{J}_1\left(\frac{J^2t}{8b}\right)\sin\left(2bt + \frac{J^2t}{8b}\right)\right.$$
$$\left. + \frac{J^4t^2}{64b^2}\left(\mathcal{J}_0^2\left(\frac{J^2t}{8b}\right) + \mathcal{J}_1^2\left(\frac{J^2t}{8b}\right)\right) - \frac{J^2t}{8b}\mathcal{J}_0\left(\frac{J^2t}{8b}\right)\mathcal{J}_1\left(\frac{J^2t}{8b}\right)\right] + O\left(\frac{J^4}{b^4}\right), \tag{2.12}$$

which has the asymptotic behavior $L_c \sim \frac{J^2t}{16\pi|b|}\left[\frac{J^2}{b^2} + O\left(\frac{J^4}{b^4}\right)\right]$ at long timescales. In Fig. 2-5 we show the dynamics of L_c in the presence of either disorder or uniform transverse field for different system sizes. It is clear that in the case of disordered fields, AL causes L_c to saturate at the localization length ξ, which is independent of L if $\xi \ll L$ (Fig. 2-5.**A**). On the other hand, L_c does not saturate with transverse field, but instead grows with a reduced velocity (Fig. 2-5.**B**). Notice that for short times, the oscillations induced by transverse field lead to an apparent localization in the system. Later it will be shown how symmetries of the MQC can be used to distinguish AL from the apparent saturation seen at short times in the fixed field case.

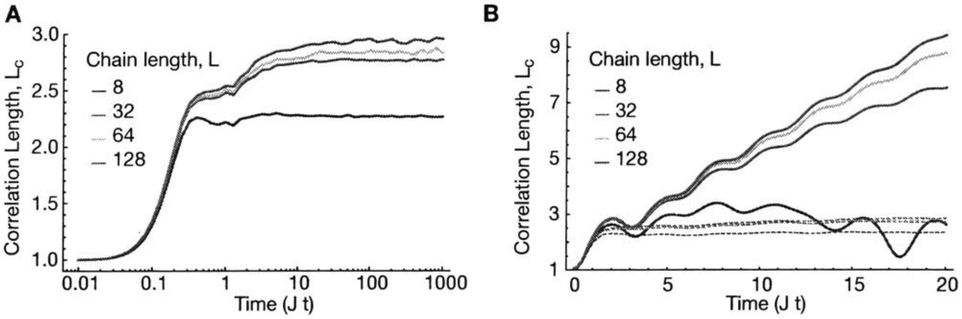

Figure 2-5: **Simulation of $\mathbf{L_c}$ for noninteracting systems.** (**A**) The dynamics of L_c under disordered field at long times; and (**B**) its behavior under uniform (solid lines) and disordered (dashed lines) fields at short times for different system sizes. With disordered fields, AL causes L_c to saturate at a value independent of L. With uniform field, L_c increases faster for larger L, indicating that the system is delocalized in the thermodynamic limit. For the disorder fields in both **A** and **B** we considered $6400/L$ disorder realizations. The disorder was drawn from a uniform distribution $\in [-4J, 4J]$. The uniform field strength was J.

2.5 Experimental Methods

The system used in the experiment was a single crystal of fluorapatite (FAp). The properties of the sample has already been described in Chapter 1. The pulse sequence used to do Hamiltonian engineering is based on a slight modification of the sequence provided in Chapter 1. Using the same notation, our 16-pulse sequence used for the experiments in this Chapter can be expressed as

$$P(\tau_1,\mathbf{x},\tau_2,\mathbf{y},2\tau_3,\mathbf{y},\tau_2,\mathbf{x},\tau_4)P(\tau_4,\mathbf{x},\tau_2,\mathbf{y},2\tau_3,\mathbf{y},\tau_2,\mathbf{x},\tau_1)P(\tau_1,\bar{\mathbf{x}},\tau_2,\bar{\mathbf{y}},2\tau_3,\bar{\mathbf{y}},\tau_2,\bar{\mathbf{x}},\tau_4)P(\tau_4,\bar{\mathbf{x}},\tau_2,\bar{\mathbf{y}},2\tau_3,\bar{\mathbf{y}},\tau_2,\bar{\mathbf{x}},\tau_1) \tag{2.13}$$

where the delays are given by

$$\tau_1 = \tau(1+3g-v+w), \quad \tau_2 = \tau(1-u+v),$$
$$\tau_3 = \tau(1+u-w), \quad \tau_4 = \tau(1-3g-v+w)$$

Taking into account of finite pulse width, H_0 is given by

$$H_0 = \frac{1}{2}\sum_{j<k} J_{jk}\left[(u-w)S_x^j S_x^k + (v-u)S_y^j S_y^k + (w-v)S_z^j S_z^k\right] + g\sum_j h_j S_z^j,$$

and $H_1 = 0$. Restricting to only nearest-neighbor (NN) terms and setting $w = -v$ leads to Eq. (3) in the main text. In addition, by properly modifying the timing and the phases of the pulses, it is also possible to engineering $-H_0$, that is, to invert the arrow of time. In our experiments, we make $-H_0$ (with $w = -v$) by incrementing all phases in the pulse sequence by $\pi/2$, changing v to $-v$ and g to $-g$, while keeping u the same. A uniform transverse field is introduced into the system via the sequence rotating method introduced in Chapter 1. The uniform transverse field can also be reversed by rotating the sequence in the opposite direction.

The method to measure MQC intensities used in this Chapter has already been described in Chapter 1. Here we note that the schemes for measuring MQC intensities amounts to the detection of out-of-time order correlation (OTOC) [47, 43]. Indeed, consider the operators $V \equiv Z = \sum_j S_z^j$ and $W \equiv \Phi = e^{-i\phi Z}$. The signal S_ϕ corresponds to measuring the OTOC, $S_\phi(t) = \langle W(t)^\dagger V^\dagger(0) W(t) V(0)\rangle$, for a system at infinite temperature [43, 90]. While we cannot measure a full basis for a subsystem of the Hilbert space (which has been shown to yield the second Rényi entropy [43]), as we have shown in the main text we can use the measured OTOC's to extract an equivalent metric of the the many-body localized phase. We expect that our metric could be of interest in studying many-body phase transitions or chaotic systems.

2.6 Extracting L_c from MQC

Thanks to the structure of the density matrix shown in Eq. (3.2), we can design a protocol for extracting the average correlation length for the non-interacting system, and to extract a close approximation in the case of interactions (see Fig. 2-6). The first step is to extract signal separately from each of the four sectors, $\bar{\mu}_k$, $\bar{\chi}_k$, $\bar{\eta}_k$, and $\bar{\nu}_k$, defined in Eq. (2.10). We use time reversal of the evolution Floquet Hamiltonian to measure $\rho(t)$ and $\rho(-t)$. Since $\rho(-t) = \rho^*(t)$, we can thus obtain the real and imaginary parts of ρ from $\rho(t) \pm \rho(-t)$.

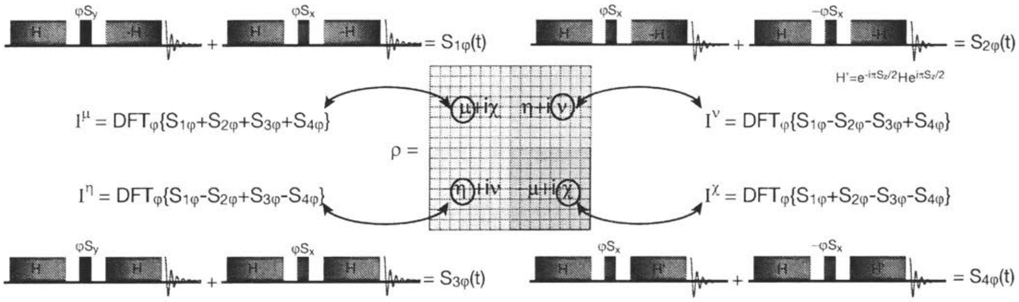

Figure 2-6: **Experimental scheme for extracting the correlation length from measurements of the MQC.** For one measurement of L_c, we perform four MQC experiments according to the above to obtain $S_{1\phi}$, $S_{2\phi}$, $S_{3\phi}$, and $S_{4\phi}$. The MQC intensities for each sector of the density matrix are obtained by first taking the appropriate linear combinations of $S_{j\phi}$ and Fourier transforming with respect to ϕ. The Hamiltonian H in the diagram is engineered using the pulse sequence Eq. (2.13), a schematic of the sequence is shown in Fig. 1-1.C.

The real part, Re$[\rho]$, only contains correlations with an even number of S_y and S_x

operators, i.e, operators such as $\mathcal{B}^{(\mathrm{re})} \propto S_x^i \prod_{k=i+1}^{j-1} S_z^k S_x^j \pm S_y^i \prod_{k=i+1}^{j-1} S_z^k S_y^j$. The imaginary part, instead, $\mathrm{Im}[\rho]$, is composed of $\mathcal{B}^{(\mathrm{im})}$ operators with S_x, S_y operators (and vice-versa) as end spins. We can then further subdivide $\mathrm{Re}[\rho]$ and $\mathrm{Im}[\rho]$ using phase cycling [21]. We note that $S_x^i \dots S_x^j + S_y^i \dots S_y^j$ and $S_x^i \dots S_y^j - S_y^i \dots S_x^j$ are invariant under rotations around z whereas $S_x \dots S_x - S_y \dots S_y$ and $S_x \dots S_y + S_y \dots S_x$ pick up a minus sign when rotated by $\pi/2$. Thus, by measuring $\mathrm{Re}[\rho] \pm U(\pi/2)\mathrm{Re}[\rho]U(\pi/2)^\dagger$ (and similarly for the imaginary part) we can finally find the contributions from the four sectors.

Next we measure the MQC intensities encoded in the x axis for each of these four sectors. For the non-interacting system, the MQC intensities encoded along the x axis for each sector (labeled by the superscript) can be written as

$$\begin{aligned}
I_q^\mu &= \frac{\delta_{1|q|}}{2}\bar{\mu}_0 + \sum_{k=1}\left[\frac{1}{2^{k+1}}\binom{k+1}{\frac{k+1-q}{2}} + \frac{1}{2^{k-1}}\binom{k-1}{\frac{k-1-q}{2}}\right]\bar{\mu}_k \\
I_q^\eta &= \sum_{k=1}\left[\frac{1}{2^{k+1}}\binom{k+1}{\frac{k+1-q}{2}} + \frac{1}{2^{k-1}}\binom{k-1}{\frac{k-1-q}{2}}\right]\bar{\eta}_k \\
I_q^\chi &= \sum_{k=1}\frac{1}{2^{k-1}}\binom{k}{\frac{k-q}{2}}\bar{\chi}_k \\
I_q^\nu &= \sum_{k=1}\frac{1}{2^{k-1}}\binom{k}{\frac{k-q}{2}}\bar{\nu}_k
\end{aligned} \tag{2.14}$$

I_q^μ and I_q^η are defined for $k - q \in$ odd, whereas I_q^χ and I_q^ν are defined for $k - q \in$ even. These expressions amount to a linear transformation $f_k = \sum_{jk} M_{kq}^{(j)} I_q^j$, where $M^{(j)}$ are constant matrices calculated from the inverse of Eq. (2.14). Notice that the MQC spectrum is symmetric, $I_q = I_{-q}$, and satisfies the normalization condition $\sum_q I_q = 1$. All experimental data presented in the main text have been normalized accordingly. By inverting Eq. (2.14) we can extract $\bar{\mu}_k$, $\bar{\chi}_k$, $\bar{\eta}_k$, and $\bar{\nu}_k$ from measured MQC intensities and find f_k using Eq. (2.10).

In the case of the double quantum Hamiltonian, $H_{\mathrm{dq}} = J\sum_j(S_+^j S_+^{j+1} + S_-^j S_-^{j+1}) + g\sum_j h_j S_z^j + b\sum_j S_z^j$, there is a symmetry given by $[\sum_j(-)^j S_z^j, H_{\mathrm{dq}}] = 0$. For ρ_{eq}

this symmetry leads to $\bar{\mu}_{k\in\text{odd}} = \bar{\chi}_{k\in\text{odd}} = \bar{\eta}_{k\in\text{even}} = \bar{\nu}_{k\in\text{even}} = 0$. This simplifies the MQC experiments considerably, and we can extract all the non-vanishing coefficients by decomposing the density matrix into two sectors instead of four

$$\begin{aligned}
I^{\mu+\chi}_{q\in\text{odd}} &= \frac{\delta_{1|q|}}{2}\bar{\mu}_0 + \sum_{k=2,4,\cdots}\left[\frac{1}{2^{k+1}}\binom{k+1}{\frac{k+1-q}{2}} + \frac{1}{2^{k-1}}\binom{k-1}{\frac{k-1-q}{2}}\right]\bar{\mu}_k \\
I^{\eta+\nu}_{q\in\text{even}} &= \sum_{k=1,3,\cdots}\left[\frac{1}{2^{k+1}}\binom{k+1}{\frac{k+1-q}{2}} + \frac{1}{2^{k-1}}\binom{k-1}{\frac{k-1-q}{2}}\right]\bar{\eta}_k \\
I^{\mu+\chi}_{q\in\text{even}} &= \sum_{k=2,4,\cdots}\frac{1}{2^{k-1}}\binom{k}{\frac{k-q}{2}}\bar{\chi}_k \\
I^{\eta+\nu}_{q\in\text{odd}} &= \sum_{k=1,3,\cdots}\frac{1}{2^{k-1}}\binom{k}{\frac{k-q}{2}}\bar{\nu}_k
\end{aligned} \tag{2.15}$$

When disorder is absent, it can be explicitly shown that all remaining $\bar{\chi}_k$ and consequently $I^{\mu+\chi}_{q\in\text{even}}$ vanish.

2.6.1 Verifying Disorder in the System

This feature can be used to distinguish between the saturation of L_c due to experimental limitations at long time and its quenching due to disorder. In particular, we can show that L_c saturation at the intermediate times of interest in this work is due to the controlled insertion of disorder and not simply to experimental imperfections. To that end, we can use properties of the MQC intensities to discriminate between disorder and a uniform transverse field (Fig. 2-5), which would mimic many experimental imperfections associated e.g. with collective pulse errors.

In Fig. 2-7.**A** we shows that L_c saturates at lower values as we increase the disorder strength. On these timescales, however, L_c shows an apparent saturating behavior for both disordered or transverse fields (Fig. 2-7.**C**). As shown above, $I^{\mu+\chi}_{q\in\text{even}}$ vanishes when disorder is absent, while it is still non-zero for the disordered case. This can clearly be seen in the experimental data when comparing the MQC data from this sector in Fig. 2-7.**B** and **D**. This indicates that the behavior of L_c in Fig. 2-7.**B** is not due to disorder, and we expect L_c to resume linear growth at long times. Conversely, we can use this experimental evidence to prove that our Hamiltonian engineering technique can indeed introduce disorder in the system evolution. Thus $I^{\mu+\chi}_{q\in\text{even}}$ can be used as a litmus test for disorder in experiments.

While the methods presented in this section are exact for extracting L_c and D_c for noninteracting systems, it works surprisingly well as an approximation for MBL systems. See Fig. 2-8.**D** for comparison between exact L_c and approximated L_c using Eq. (2.14) and Eq. (2.10).

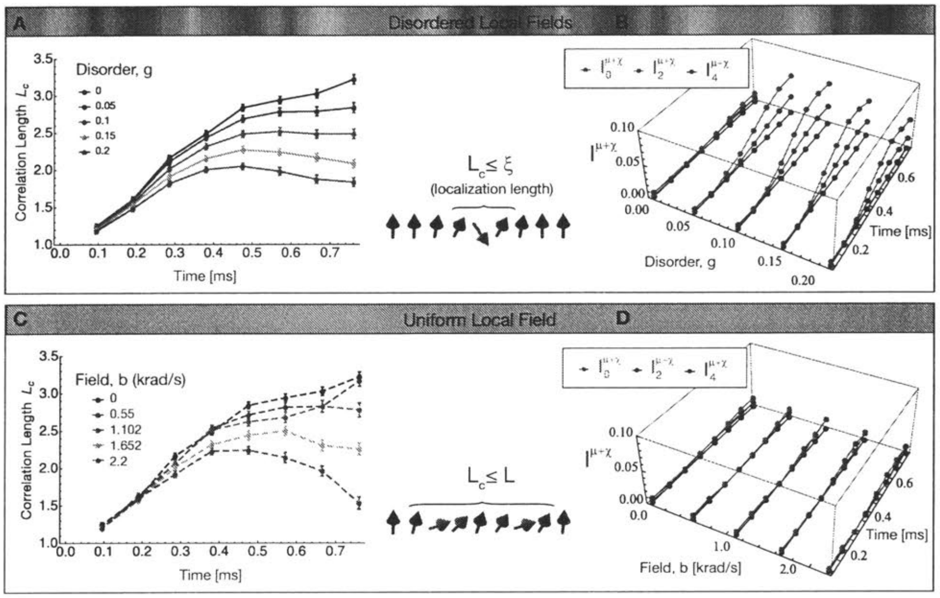

Figure 2-7: **Experimental measurement of $\mathbf{L_c}$ and MQC intensities for noninteracting systems.** Experimentally measured L_c and MQC intensities in the $\mu+\chi$ sector for the double quantum Hamiltonian H_{dq} with different strength of disorder (**A**, **B**) and transverse uniform field (**C**, **D**) . In the absence of any disorder, it can be shown $I^{\mu+\chi}_{q\in\text{even}} = 0$ based on symmetry arguments. Due to the structure of Eq. 2.15, it is sufficient to measure just $S_{1\phi}$ and $S_{2\phi}$ to exactly find L_c.

2.7 Comparison with Known Metrics of Localization

The many-body localized phase can be identified by the behavior of the entanglement entropy (EE) calculated on a subsystem. This metric has been used extensively in numerical studies to gather evidence that spin chains may be in the many-body localized (MBL) or ergodic phase depending on the relative strength of interaction and disorder [112, 132, 97]. Unfortunately, this quantity is typically challenging to measure experimentally, and other metrics have been proposed to analyze the dynamics of out-of-equilibrium systems.

The metric we introduced in the main text directly aims at evaluating the spread of correlations, its saturation due to Anderson localization, and its slow, logarithmic growth in the presence of interaction (MBL). Here we compare our metric with other proposed metrics, to evaluate its robustness and put our work in context. In addition, we show the behavior of well-known metrics of MBL for our physical systems, compare them to the proposed metrics and establish approximate relationships and bounds between them.

Previous works have used the Hamming distance to quantify localization for pure states [136, 57], but this metric shows quantitatively similar dynamics in both AL and MBL. Out-of-time ordered correlations (OTOC) between spatially separated local observables have been proposed as a metric to distinguish AL and MBL [64], and recently measured in some systems [47, 90]. However, OTOC of local operators and other correlation metrics such the QFI are difficult to measure in large many-body systems, as they require the ability to address a subset of the total system. While the QFI has been linked to the experimentally accessible dynamic susceptibility [58], this relationship is valid only for systems at thermal equilibrium.

In [130], particle imbalance between odd and even sites was measured in a disordered 1-D fermionic optical lattice, whereas in [28], imbalance between left and right halves was measured in a disordered 2-D bosonic optical lattice. In both cases a vanishing imbalance, characteristic of nonergodic behavior in MBL systems, was observed for strong disorder. While able to clearly distinguish between ergodic and MBL dynamics, particle imbalance cannot distinguish between AL and MBL, as AL and MBL will both show non-vanishing particle imbalance. In other cold atom works [84, 114], localization was detected by measuring the atomic quasimomentum distribution, which however cannot directly distinguish between AL and MBL.

More recently, signatures of MBL were observed in a chain of 10 ions interacting via long-range Ising couplings [136]. They reported a slow growth of quantum Fisher information (QFI) consistent with slow spreading of correlations in MBL systems. While QFI is useful as an entanglement witness for pure states, it is hard to measure in mixed states (see however a recent breakthrough [58]). All of these cold atom experiments relies on single site addressability, which is not readily available in solid-state systems. Our approach requires no local control of the system, and relies only on collective rotations and measurements, in contrast to recently proposed metrics [50] that also detect the spread of correlations but require single-spin addressability.

MQC have also been used in nuclear spin systems [6, 7] and trapped ions [47], and they've been shown to relate to an entanglement witness for pure states [46]. However, in NMR studies, the MQC behavior (localization under decoherence and no disorder) and its analysis relied on assumptions on the MQC distributions that is only verified for 3D systems. The results for the trapped ion system are instead valid for pure state systems. Our methods can instead be applied to 1D systems (which makes for an easier comparison to numerical and analytical studies) and at high temperature (where other metrics fail).

Our work is thus an unique addition to the previous studies as it can distinguish between AL and MBL for mixed states at high temperature, while requires no local control on the system.

2.7.1 Entanglement/Rényi Entropy and Mutual Information

In our experiments we engineered the Hamiltonian $H = uJ\sum_j(S_+^jS_+^{j+1} + S_-^jS_-^{j+1}) + vJ\sum_j(S_+^jS_-^{j+1} + S_-^jS_+^{j+1} - S_z^jS_z^{j+1}) + \sum_j h_jS_z^j$ and showed how it leads to an MBL state. Indeed, our collective control prevented us from engineering Hamiltonians more commonly found in the literature. As this Hamiltonian has not been studied previously, here we show that its interacting version does indeed support MBL by calculating the bipartite entanglement entropy for an $L = 8$ chain averaged over 10^3 disorder realizations (Fig. 2-8.**A**). We use the initial pure product state $|\uparrow\uparrow\uparrow\cdots\uparrow\uparrow\rangle$, and calculate the entropy $S_R = -\mathrm{Tr}[\rho_R \log \rho_R]$, where ρ_R is the reduced density matrix of the right half of the chain. We observe a logarithmic growth of entanglement in the presence of weak interactions, a defining feature that separates MBL from AL.

We next consider the entanglement entropy in our high-temperature system. As the largest component of the Hamiltonian is the Zeeman interaction, $H_Z = \omega_0 Z$, with $\omega_0 = (2\pi)283$ MHz, the thermal equilibrium state can be well approximated by $\rho_{\text{eq}} = e^{-\beta H} \approx e^{-\beta\omega_0 Z}$. In the experimental conditions, $\epsilon = \beta\omega_0 = \gamma_F B/k_B T \approx 4.6 \times 10^{-5}$ and we have so far considered an expansion to first order in ϵ, $\rho_{\text{eq}} = \frac{1}{2^L}(\mathbb{1} - \epsilon Z)$. Since the entropy of the reduced density matrix is zero to first order in ϵ, we consider the expansion up to second order,

$$\rho_{\text{eq}} = 2^{-L}[(1 - \epsilon^2 L/8)\mathbb{1} - \epsilon Z + \epsilon^2 Z^2/2]$$

To second order in ϵ, the entropy of the reduced density matrix of the right half of the chain is

$$S_R = -\text{Tr}[\rho_R \log(\rho_R)] \approx \frac{1}{2}\left(L\log(2) - \frac{\epsilon^2}{2^{3L/2}}\text{Tr}[\delta\rho_R^2(t)]\right),$$

where $\delta\rho_R(t) = \text{Tr}_L[U(t)ZU(t)^\dagger]$. Thus for high temperatures, entanglement entropy is well approximated by the second Rényi entropy, $S_L^{(2)}$. In Fig. 2 of the main text we plot $1 - 2^{-\frac{L}{2}}\frac{8}{L}\text{Tr}[\delta\rho_R^2(t)] = \frac{2^{L+4}}{\epsilon^2 L}[S_R - \frac{L}{2}\log(2)] + 1$.

In order to avoid the large constant term in this expression, we can calculate instead the mutual information (MI) $\mathcal{I}$, defined as $\mathcal{I} = S_L + S_R - S_{L\cup R}$ [53]. MI is a measure of the total correlations, both quantum and classical, in the system. Notice that MI reduces to twice the bipartite entanglement entropy for pure states, since $S_{L\cup R} = 0$ and $S_L = S_R$ for pure states. For ρ_{eq}, MI can be approximated as

$$\mathcal{I} \approx \frac{\epsilon^2}{2}\left(\frac{L}{4} - 2^{-3L/2}\left[\text{Tr}(\delta\rho_L^2) + \text{Tr}(\delta\rho_R^2)\right]\right) \tag{2.16}$$

Interestingly, $\mathcal{I}$ also saturates for noninteracting systems and increases logarithmically when interactions is added (see Fig. 2-8.**B**), with a similar behavior as S_R. A recent theoretical work studying MI in the context of MBL can be found in [33]. Strictly

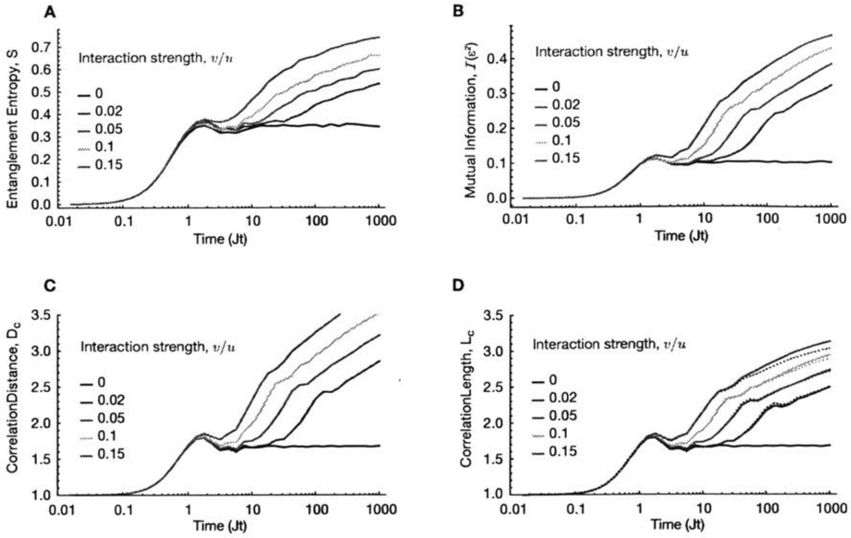

Figure 2-8: **Different correlation metrics used to distinguish MBL from AL.** For pure states, the bipartite entanglement entropy is used (**A**). For ρ_{eq}, the mutual information (**B**), correlation distance (**C**), and correlation length (**D**) can be used. In **D**, the dashed lines corresponding to the approximated L_c extracted from MQC intensities. All plots are for $L = 8$ with open boundary conditions, the disorder h_j is drawn uniformly from $[-W, W]$ with $W = 8$ and 960 realizations. The entanglement entropy in (**A**) was rescaled as described above. In (**B**) we plot $\mathcal{I}$ in units of ϵ^2, where the mutual information was calculated assuming $\epsilon = 10^{-5}$.

speaking ρ_{eq} should also include a term linear in dipolar interaction, i.e., ϵH_{dip}. While this term is larger than $\epsilon^2 Z^2/2$, it does not contribute to mutual information or entanglement entropy to lowest order.

Next we show the dynamics of D_c in Fig. 2-8.**C**, and compare L_c with the approximated L_c (using the MQC method explained in sections 2.6) in Fig. 2-8.**D**. These correlation metrics all display logarithmic growth in the MBL phase, and thus can be applied analogously as entanglement entropy in distinguishing MBL from AL for highly mixed interacting systems.

2.7.2 Relation between Our Metrics and Mutual Information and Entanglement/Rényi Entropy

As shown in Fig. 2 of the main text, L_c and a rescaled Entanglement Entropy show a very similar behavior, suggestive of a direct relationship. Here we argue that D_c, L_c,

S_R, and $\mathcal{I}$ are closely related when considering highly mixed states such as ρ_{eq}. We show this relationship using D_c, but a similar argument also holds for L_c. Since the total weight of all correlations sums to one, we can rewrite the last term in Eq. (2.16) as

$$\mathrm{Tr}(\delta\rho_L^2) + \mathrm{Tr}(\delta\rho_R^2) = \frac{2^{3L/2}L}{4}\left(1 - \sum_{j=1}^{L/2}\sum_{k=L/2+1}^{L}\sum_{r=1}^{\xi_{k+1-j}}\left[a_{j,k}^r\right]^2\right) \tag{2.17}$$

The LHS of Eq. (2.17) represents the total weight of correlations contained in the left and right halves of the chain. It is different from one by the amount corresponding to the correlations across the middle of the chain. This difference is the last term inside the bracket on the RHS. If we approximate the weights of local correlations as averages of bulk weights, i.e., $\sum_{r=1}^{\xi_2}[a_{L/2,L/2+1}^r]^2 = \frac{d_2}{L-1}$, $\sum_{r=1}^{\xi_3}[a_{L/2,L/2+2}^r]^2 = \frac{d_3}{L-2}$, and etc., we can place a lower bound on this difference as

$$\sum_{j=1}^{L/2}\sum_{k=L/2+1}^{L}\sum_{r=1}^{\xi_{k+1-j}}\left[a_{j,k}^r\right]^2 = \sum_{k=2}^{L/2+1}\frac{k-1}{L-(k-1)}d_k + \sum_{k=L/2+2}^{L} d_k \geq \sum_{k=1}^{L}\frac{k-1}{L-1}d_k = \frac{D_c-1}{L-1} \tag{2.18}$$

The approximation $\sum_{r=1}^{\xi_k}[a_{L/2,L/2+k}^r]^2 \approx \frac{d_k}{L-k}$ becomes exact for a translationally invariant system, which is a good approximation for a large system with weak disorder. Similarly, the inequality in the last step of Eq. (2.18) becomes tighter for larger systems. Even in the presence of strong disorder, the approximation is still valid upon averaging over many disorder realizations. Substituting Eq. (2.18) into Eq. (2.16) we obtain a lower bound on the mutual information in terms of the average correlation distance:

$$\mathcal{I} \geq \frac{\epsilon^2 L}{8(L-1)}(D_c - 1) \tag{2.19}$$

With a similar reasoning, we can obtain $\mathcal{I} \geq \frac{\epsilon^2 L}{8(L-1)}(L_c - 1)$. In order to relate L_c and D_c to entanglement entropy, we first note that $S_L \approx S_R$ after disorder averaging.

This allows us to write

$$S_L = \frac{L}{2}\left(\log(2) - \frac{\epsilon^2}{8}\right) + \frac{\mathcal{I}}{2}$$

Using Eq. (2.18), we can place a lower bound on the time-dependent part of the entanglement entropy as

$$\frac{\epsilon^2 L}{16(L-1)}(D_c - 1) \leq S_L - \frac{L}{2}\left(\log(2) - \frac{\epsilon^2}{8}\right) \tag{2.20}$$

Similarly for the second order Rényi entropy: $S_L^{(2)} = \frac{L}{2}\log(2) - \frac{\epsilon^2}{2^{3L/2}}\text{Tr}(\delta\rho_L^2)$, the time-dependent component has a lower bound given by

$$\frac{\epsilon^2 L}{8(L-1)}(D_c - 1) \leq S_L^{(2)} - \frac{L}{2}\left(\log(2) - \frac{\epsilon^2}{4}\right)$$

Beyond the bounds described above, we can obtain explicit expressions for the second order Rényi entropy (or other entanglement metrics) that can be related to measurable quantities in our system. Consider for example the state expansion in terms of the $\mathcal{B}_k^r$ operators, as in Eq. (1) of the main text. Taking the partial trace of these traceless operators, we obtain the Rényi entropy for the left half of the spin chain:

$$S_L^{(2)} = \frac{L}{2}\log(2) - \frac{\epsilon^2/4}{2^{3L/2}}\sum_{k=2}^{L/2}\sum_{s}^{\zeta_k^L}(b_k^s)^2,$$

where ζ_k^L counts only the configurations in the left half of the chain. We note that most generally, for $k > 1$, we have $\zeta_k^L = \frac{L/2-k+1}{L-k+1}\zeta_k$, where ζ_k are all the k-spin configurations in the whole chain.

Given the symmetry of the system, we expect that for a translationally invariant system, b_k^r do not depend on the first spin position, and thus we have $\sum_s^{\zeta_k^L}(b_k^s)^2 = (\zeta_k^L/\zeta_k)f_k$. While this is not exactly true for finite systems with open boundaries (and generally in the presence of disorder), we can still extract an approximated

Rényi entropy:

$$S_L^{(2)} \approx \frac{L}{2}\log(2) - \frac{\epsilon^2/4}{2^{3L/2}}\left(\frac{f_1}{2} + 2\sum_{k=2}^{L/2}\frac{L/2-k+1}{L-k+1}f_k\right) \tag{2.21}$$

This approximated Rényi entropy also shows a distinctive logarithmic growth for the MBL state and can be measured experimentally with our MQC intensity protocol. It is thus an equivalent metric to L_c, however we prefer to still refer to L_c since it has a simpler physical interpretation.

2.8 Conclusion

In conclusion, we introduced a novel metric for localization, able to distinguish between many-body and single-particle localization. The correlation metric can be measured experimentally, with the only requirement of collective rotations and measurements, by extending MQC techniques developed in NMR that can as well be applied to many other physical systems [47]. We also reveal an interesting relationship between the protocol for measuring the correlation length and the measurement of OTOC, thus further confirming its ability to measure the logarithmic growth of entanglement associated with MBL. Thanks to our control techniques, we were able to explore a broad range of interesting behaviors in this solid-state spin system. In particular, we observed, for the first time, many-body localization in a natural spin system associated with a single crystal at high temperature. We note that while we interpreted our results mostly based on a simplified model (1D, nearest-neighbour couplings), the real system is more complex due to long-range interactions and a 3D structure. It will be thus interesting to use the tools developed in this work to study subtler properties of localization when these effects are highlighted by the experimental scheme.

Chapter 3

Out-of-Time Ordered Correlations

3.1 Introduction

Out-of-time ordered correlations (OTOC) was first studied in the context of superconductivity [89, 81, 82]. More recently, OTOC have been proposed as a tool to diagnose chaos and scrambling in quantum many-body systems [101, 100, 63, 125]. Semiclassically, chaos is defined as ultrasensitivity in the trajectory due to perturbations in the initial condition. This can be expressed quantitatively as

$$\{x(t), p(0)\} \sim \frac{\partial x(t)}{\partial x(0)} \sim e^{\lambda_L t} \tag{3.1}$$

where λ_L is called the Lyaponov exponent. A quantum mechanical measure of the same effect is captured by the OTO commutator [81, 101]

$$C(t) = \langle |[W(t), V]|^2 \rangle$$

which is evaluated with respect to a thermal distribution with temperature $T = \beta^{-1}$: $\langle \cdot \rangle = \mathrm{Tr}(e^{-\beta H} \cdot)/\mathrm{Tr}(e^{-\beta H})$.

When $W(t)$, V are local operators with unit norm, the OTO commutator between

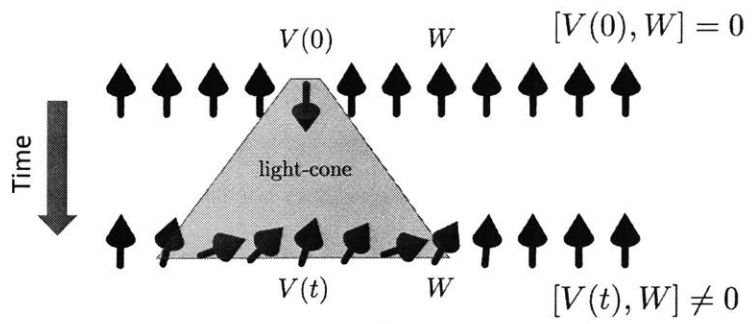

Figure 3-1: **OTO Commutator** Illustration of OTO commutator dynamics between spatially separated local operators. Information about V is felt by W only after a time t, at which $V(t)$ overlaps with W. and the commutator $-[W(t), V]^2$ increases.

the two can be written as

$$C(t) = \langle |[W(t), V]|^2 \rangle = 1 - \mathrm{Re}\,\langle W(t)VW(t)V \rangle$$

where the term $F = \langle W(t)VW(t)V \rangle$ in the last expression is the OTOC. Physically, both OTO commutator and correlation describes how local perturbation in one part of the system is "felt" by another part at time t. As shown in Fig 3-1, $W(0)$ and V are spatially separated and thus commute at $t = 0$. As $W(t) = e^{-iHt}W(0)e^{iHt}$ evolves in time, $W(0)$ starts to correlate with nearby spins and these correlations eventually spread to V resulting in an increase of C (or a decrease in F). Information scrambling refers to the scenario where local information is completely transformed into many-body correlations in the system, and thus becoming effectively hidden to any local measurements [139].

This thesis focuses on the study of OTO commutators between sum of local operators, as they can be experimentally measured using only collective controls in the NMR system. However collective operators do not "wash away" the interesting features in the OTO commutator otherwise shown with local operators.

3.2 Relating OTO Commutator with L_c

Since OTO commutator gives information about the spatial extent of many-spin correlations, it is natural to ask whether it can be related to the correlation length L_c introduced in the last Chapter. For noninteracting systems this is indeed possible and the relationship has a particularly simple form. The main idea, which will be described in detail in later sections, is that the OTO commutator can be related to the second moment of MQC intensities via $-\mathrm{Tr}[W(t), V]^2 = \sum_q q^2 I_q(t)$. When the Hamiltonian can be mapped into noninteracting fermions, the MQC intensities can be exactly computed in some cases. Given the initial state $\delta\rho(0) = L^{-1/2}\sum_j \sigma_z^j$, or any operator which can be expressed as sum of bilinear fermion terms, the time-dependent density operator can be written as

$$\delta\rho = \sum_j \mu_{jj}\sigma_z^j + \sum_{j,k>j} \left[-(\mu+\eta)_{jk}\sigma_x^j\sigma_x^k - (\mu-\eta)_{jk}\sigma_y^j\sigma_y^k + (\nu+\chi)_{jk}\sigma_y^j\sigma_x^k + (\nu-\chi)_{jk}\sigma_x^j\sigma_y^k\right] \prod_{j<l<k}\sigma_z^l, \tag{3.2}$$

where μ is a real and symmetric matrix, whereas χ, η, ν are real and antisymmetric matrices. Recall from last Chapter these four $L \times L$ matrices describe the four possible ways spins can correlate in noninteracting systems. The normalization $\delta\rho$ translates to $1 = \mathrm{Tr}[\mu\mu^T + \chi\chi^T + \eta\eta^T + \nu\nu^T]$. In terms of these matrices, it can be shown that the MQC intensities encoded along x are given by

$$\begin{aligned} I_q^{\mathbf{x}} = \frac{\delta_{1|q|}}{2}\bar{\mu}_0 + \sum_{k=1}\left[\frac{1}{2^{k+1}}\binom{k+1}{\frac{k+1-q}{2}}\sum_j(\mu-\eta)^2_{jj+k} + \frac{1}{2^{k-1}}\binom{k-1}{\frac{k-1-q}{2}}\sum_j(\mu+\eta)^2_{jj+k}\right] \\ + \sum_{k=1}\frac{1}{2^{k-1}}\binom{k}{\frac{k-q}{2}}(\bar{\chi}_k + \bar{\nu}_k) \end{aligned} \tag{3.3}$$

where $\bar{\mu}_k = \sum_j \mu^2_{jj+k}$, and similar expressions are defined for χ, η, and ν. Calculating the second moment leads to

$$\frac{-1}{2^{L+2}L}\mathrm{Tr}[Z(t),X]^2 = \bar{\mu}_0 + \sum_{k=1}\left[(k+1)\sum_j(\mu-\eta)^2_{jj+k} + (k-1)\sum_j(\mu+\eta)^2_{jj+k} + 2k(\bar{\chi}_k+\bar{\nu}_k)\right] \tag{3.4}$$

where $Z = \sum_j S^j_z$, and $X = \sum_j S^j_x$. Similarly for the MQC intensities encoded in the y-axis

$$\begin{aligned} I^y_q = \frac{\delta_{1|q|}}{2}\bar{\mu}_0 &+ \sum_{k=1}\left[\frac{1}{2^{k+1}}\binom{k+1}{\frac{k+1-q}{2}}\sum_j(\mu+\eta)^2_{jj+k} + \frac{1}{2^{k-1}}\binom{k-1}{\frac{k-1-q}{2}}\sum_j(\mu-\eta)^2_{jj+k}\right] \\ &+ \sum_{k=1}\frac{1}{2^{k-1}}\binom{k}{\frac{k-q}{2}}(\bar{\chi}_k+\bar{\nu}_k) \end{aligned} \tag{3.5}$$

calculating the second moment leads to

$$\frac{-1}{2^{L+2}L}\mathrm{Tr}[Z(t),Y]^2 = \bar{\mu}_0 + \sum_{k=1}\left[(k+1)\sum_j(\mu+\eta)^2_{jj+k} + (k-1)\sum_j(\mu-\eta)^2_{jj+k} + 2k(\bar{\chi}_k+\bar{\nu}_k)\right] \tag{3.6}$$

If one takes the average of the two commutator norms in Eq.3.4 and 3.6, one obtain

$$\begin{aligned} \frac{-1}{2^{L+3}L}(\mathrm{Tr}[Z(t),X]^2 + \mathrm{Tr}[Z(t),Y]^2) &= \bar{\mu}_0 + 2\sum_{k=1}k(\bar{\mu}_k+\bar{\eta}_k+\bar{\chi}_k+\bar{\nu}_k) \\ &= L_c - 1 + f_1 \end{aligned} \tag{3.7}$$

where $L_c = \sum_{k=1} kf_k$ is the correlation length and f_k represents the weight of all k-spin correlations: $f_1 = \bar{\mu}_0$, $f_{k>1} = 2(\bar{\mu}_{k-1} + \bar{\eta}_{k-1} + \bar{\chi}_{k-1} + \bar{\nu}_{k-1})$. Here one sees that the commutator norm between $Z(t)$ and X or Y has a simple physical picture, it is related to the average number of correlated spins in $Z(t)$. Depending on the dynamics of $Z(t)$, the commutator norm (and OTOC) can grow indefinitely with time in the thermodynamic limit.

3.3 OTO Commutator in Ising Chains

Now equipped with exact solution to some OTO commutators in noninteracting systems, one can see how OTO commutator behaves in simple many-body models. Consider the transverse field Ising model (TFI) given by the Hamiltonian [129]

$$H_{\mathrm{TFI}} - \sum_{j} \sigma_x^j \sigma_x^{j+1} + g \sum_{j} \sigma_z^j \tag{3.8}$$

The TFI model is perhaps the simplest model exhibiting a quantum phase transition (QPT) [129]. In particular, the ground state in TFI has a symmetry breaking QPT in the thermodynamic limit (system size → infinity), where the ground state $|\mathrm{GS}\rangle$ goes from a paramagnet $|\uparrow\uparrow \cdots \uparrow\rangle$ for $g > 1$ to a ferromagnet pointing either along the $|\leftarrow\leftarrow \cdots \leftarrow\rangle$ or the $|\rightarrow\rightarrow \cdots \rightarrow\rangle$ direction for $g < 1$, thus breaking the so-called Z_2 symmetry in the Hamiltonian, described by a π rotation around the z axis [129].

In the symmetry breaking phase, the ground state of the system has less symmetry than the Hamiltonian. The phase transition is associated with a gap closing in the excitation spectrum, and is known to take place at only zero temperature for 1 dimensional systems. One question one can ask is whether this critical behavior at $g_c = 1$ can be observed in out-of-equilibrium or high temperature settings. If so, what observable can one measure to diagnose this critical behavior?

Consider the following OTO commutator norm for the TFI model

$$C_{ZX} = \frac{-1}{2^{L+2}L} \mathrm{Tr}[Z(t), X]^2 \tag{3.9}$$

In the limit of $g \to 0$, the Ising Hamiltonian reduces to a sum of mutually commuting terms which all commutes with X. Since $C_{ZX} = C_{XZ}$, the OTO commutator will approach 1 in this limit. Now consider the limit where $g \to \infty$. $Z(t)$ now is approaching an integral of motion so C_{ZX} again approaches 1. In the regimes of small and large g, one expects C_{ZX} to grow linearly, albeit slowly, consistent with the linear growth of L_c showed in the previous Chapter for noninteracting systems without any disorder. It is interesting to ask what happens to C_{ZX} when $g = 1$.

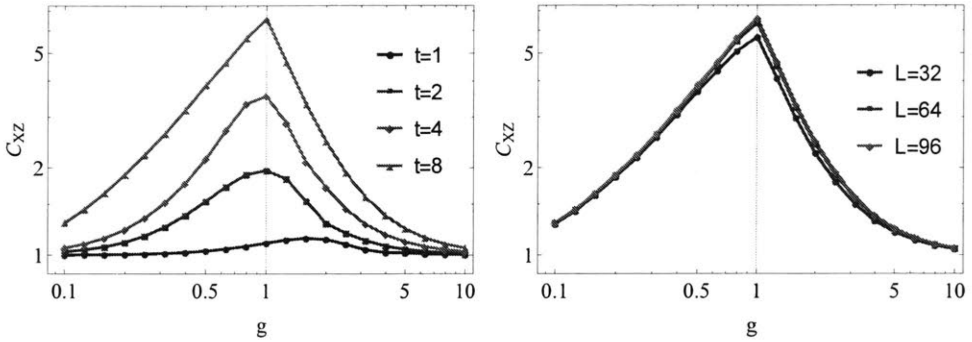

Figure 3-2: **OTO commutator C_{XZ} for TFI model** Left: C_{XZ} as a function of g for different times while keeping $L = 96$ fixed. Right: C_{XZ} as a function of g for different system sizes while keeping $t = 8$ fixed.

As shown in Fig. 3-2, the OTO commutator C_{ZX} actually grows the fastest at the critical point. Most interestingly, C_{ZX} appears to become increasing nonanalytic at $g = 1$, suggested by the "sharpening" of the peak in the case where t is fixed and L is increased (Fig. 3-2(left)), as well as the case where L is fixed and t is increased (Fig. 3-2(right)). While this critical behavior is not expected to be related to the ground state properties of the system (since the OTO commutator is calculated for infinite temperature), it is related to the gap closing in the TFI spectrum.

3.3.1 TFI Diagonalization

It is instructive to briefly go over the diagonalization for the TFI Hamiltonian. After a Jordan-Wigner transformation, the TFI Hamiltonian is written in terms of free fermion operators:

$$H_{\text{TFI}} = \sum_{j=1}^{L} \left[c_j^\dagger c_{j+1} + c_{j+1}^\dagger c_j + c_j^\dagger c_{j+1}^\dagger + c_{j+1} c_j + g(c_j^\dagger c_j - c_j c_j^\dagger) \right]$$

where PBC is used and the boundary term discarded [1]. The fermion operators can be written in terms of their Fourier transform: $c_j = \frac{1}{\sqrt{L}} \sum_q e^{-iqj} c_q$, where $q = \frac{2m\pi}{L}$. When L is odd, m takes on integer values given by $m = -\frac{L-1}{2}, \cdots, 0, \cdots \frac{L-1}{2}$. When L is even, $m = -\frac{L}{2} + 1, \cdots, \frac{L}{2}$. In the momentum basis the fermion Hamiltonian

---

[1] The boundary conditions will not affect the results of this analysis in the thermodynamic limit.

becomes block diagonal,

$$H_{\text{TFI}} = \sum_q \begin{pmatrix} c_q^\dagger & c_{-q} \end{pmatrix} \begin{pmatrix} g + \cos q & -i \sin q \\ i \sin q & -g - \cos q \end{pmatrix} \begin{pmatrix} c_q \\ c_{-q}^\dagger \end{pmatrix},$$

and each block can be readily diagonalized via Bogoliubov transformation. The excitation spectrum is given by

$$\omega_q = \sqrt{(\cos q + g)^2 + \sin q^2} \tag{3.10}$$

3.3.2 Translationally Invariant Integrals of Motion in TFI

To see why OTO commutator C_{XZ} grows the fastest, consider transforming H_{TFI} into an effective Hamiltonian $H_{\text{eff}} = U H_{\text{TFI}} U^\dagger$ consisting of only translationally invariant integral of motions:

$$H_{\text{eff}} = \sum_k \alpha_k H_{\text{eff}}^{(k)} \tag{3.11}$$

where each integral of motion is given by $H_{\text{eff}}^{(k)} = \sum_j d_j^\dagger d_{j+k} + d_{j+k}^\dagger d_j$ and satisfies

$$[H_{\text{eff}}^{(j)}, H_{\text{eff}}^{(k)}] = 0, \qquad \text{Tr}(H_{\text{eff}}^{(j)} H_{\text{eff}}^{(k)}) \propto \delta_{jk} \tag{3.12}$$

d_j are real space fermion operators in the transformed frame defined by U. Using the fact that $H_{\text{eff}}^{(k)}$ is translationally invariant and that H_{TFI} and H_{eff} must have the same spectrum, it follows that in the thermodynamic limit $L \to \infty$ the coefficients α_k are given by the Fourier coefficients of the excitation spectrum:

$$\alpha_k = \frac{1}{2\pi} \int_0^{2\pi} \omega_\theta \cos(k\theta)\, d\theta = \frac{1}{2\pi} \int_0^{2\pi} \sqrt{(\cos\theta + g)^2 + \sin\theta^2} \cos(k\theta)\, d\theta \tag{3.13}$$

Interestingly, for all values of g except for 0 and 1, the coefficients α_k decrease exponentially in k making H_{eff} short-ranged. In the limit $g = 0$, $\alpha_k = \delta_{0,k}$ making H_{eff} trivially localized. Indeed when $g = 0$ only the Ising terms are present in H_{TFI}; these terms are local and mutually commute, thus cannot propagate any correlation

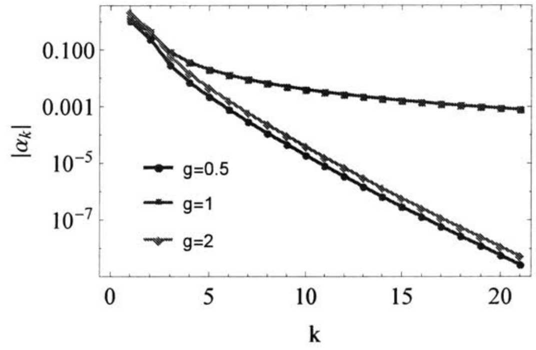

Figure 3-3: $|\alpha_k|$ **as a function of** k **for different** g The interaction range, described by α_k, goes down exponentially as a function of k for all values of g except for $g = 1$ and $g = 0$.

beyond NN. The case $g = 1$ is much more interesting. The spectrum ω_θ can close its gap and the coffiencients α_k shows power-law instead of exponential decay in k. The results are summarized in the following:

$$\alpha_k \begin{cases} = \delta_{0,k} & g = 0 \\ \propto (-1)^k e^{-ck} & g \neq 1 \\ = \frac{(-1)^k}{\pi(k^2-1/4)} & g = 1 \end{cases} \tag{3.14}$$

where c is a constant depending on g. Eq. (3.14) provides a simple explanation to why correlation spreads the fastest at the critical point, namely H_{eff} is long ranged at $g = 1$ and is short ranged for any other values of g. It is important to note that C_{XZ} always spreads linearly in time in the thermodynamic limit regardless of g. So long ranged α_k translate to a larger speed while short ranged α_k translate to lower speeds. To check Eq.(3.14), α_k is calculated numerically and presented in Fig. 3-3. The same results can be obtained directly by Fourier transforming the diagonalized version of $H_{\text{TFI}} = \sum_q \omega_q(d_q^\dagger d_q - d_q d_q^\dagger)$ using $d_q = \sum_j e^{iqj} d_j$.

Lastly, it is worth noting that it is always possible to transform free fermion Hamiltonian into a sum of translationally invariant, mutually commuting, integrals of motion.

3.3.3 Additional OTO Commutator in Ising Chains

OTO correlations and commutators were also studied recently in [93], and critical behaviors at nonzero temperature were also observed. In this section OTO commutator where both operators are bilinear in fermions are investigated at nonzero temperature. The results are given below

$$\begin{aligned}
-\frac{1}{4L}\sum_j \langle [\tau_z^j, Z]^2\rangle_\beta &= \frac{1}{L}\sum_q \frac{1-\cos 2\theta_q}{1+\operatorname{sech}\beta\omega_q} \\
-\frac{1}{4L}\langle [\sum_j \tau_z^j, Z]^2\rangle_\beta &= \frac{2}{L}\sum_q \frac{1-\cos 2\theta_q}{1+\operatorname{sech}\beta\omega_q} \\
-\frac{1}{4L}\langle [\overline{Z(t)}, Z]^2\rangle_\beta &= \frac{1}{L}\sum_q \frac{\sin^2 2\theta_q}{1+\operatorname{sech}\beta\omega_q} \\
-\frac{1}{4L}\overline{\langle [Z(t), Z]^2\rangle_\beta} &= \frac{1}{L}\sum_q \frac{\sin^2 2\theta_q + 2\sin^4\theta_q}{1+\operatorname{sech}\beta\omega_q}
\end{aligned}$$

where ω_q is given in Eq. (3.10), $\cos\theta_q = \frac{g+\cos q}{\omega_q}$, and $\sin\theta_q = \frac{\sin q}{\omega_q}$. τ_z^q are integrals of motion obtained by transforming the fermion operators $d_q^\dagger d_q$ which diagonalizes H_{TFI} back into the spin picture, $Z = \sum_j \sigma_z^j$, and $\overline{Z(t)} = \lim_{T\to\infty}\frac{1}{T}\int_0^T Z(t)\,dt$. Notice that all the commutators are time-independent by construction, and the infinite temperature expectation value is twice as the ground state expectation value. In addition, each commutator is bounded even in the thermodynamic limit. This is because the corresponding MQC intensities, whose second moments equal to the commutators, are restricted to coherence orders of 0 and ±2. So the maximum value attainable for these commutators is 4.

It is interesting to see how these commutators look as a function of g. By going to the continuum limit and replacing the sum with an integral, it can be shown that the commutators have the following expectation values in the zero temperature limit

$$-\frac{1}{4L}\sum_j \langle [\tau_z^j, Z]^2\rangle_0 = \begin{cases} 1 & g<1 \\ \frac{1}{g^2} & g>1 \end{cases}$$

$$-\frac{1}{4L}\langle [\sum_j \tau_z^j, Z]^2\rangle_0 = \begin{cases} 2 & g<1 \\ \frac{2}{g^2} & g>1 \end{cases}$$

$$-\frac{1}{4L}\langle [\overline{Z(t)}, Z]^2\rangle_0 = \begin{cases} \frac{1}{2} & g<1 \\ \frac{2}{g^2}-\frac{3}{2g^4} & g>1 \end{cases}$$

$$-\frac{1}{4L}\overline{\langle [Z(t), Z]^2\rangle_0} = \begin{cases} \frac{5}{4} & g<1 \\ \frac{2}{g^2}-\frac{3}{4g^4} & g>1 \end{cases}$$

It is interesting to see that when both operators can be represented by free fermions, the commutator saturates to a constant value for $g < 1$ and decreases as g^{-2} or g^{-4} for $g > 1$.

Chapter 4

OTO Commutator in Dipolar Chains

Having build up some intuition on OTO commutator in Ising chains, it is time to move on the dipolar chains whose Hamiltonian can be experimentally realized using multipulse techniques described in Chapter 1. While some similarities with the Ising model exist, dipolar chains are fundamentally different as they are not exactly solvable.

4.1 Introduction

The dynamics of many-body quantum systems can display a multitude of interesting phenomena, ranging from thermalization [74, 85] to many-body localization (MBL) [15, 14, 109, 130, 136, 28, 142, 98], discrete time crystals [76, 75, 39, 105, 128, 145, 148, 29, 60], and dynamical phase transitions [149, 147, 59, 153, 45, 72]. Recently, there has been increased interests in systems exhibiting nonergodic dynamics in the absence of any disorder or incommensurate fields, such as quasi-MBL in translationally invariant systems [144] and disorder free localization [113, 135, 104]. Another intriguing possibility is prethermalization, where nonintegrable quantum systems may fail to thermalize on practically accessible timescales [19, 52, 42, 40, 2, 110], yielding an emergent integral of motion.

Here we study thermalization and prethermalization by measuring out-of-time-ordered (OTO) commutators [89, 81, 82, 48, 91, 88], which are powerful indicators of information scrambling, but are typically difficult to observe experimentally.

4.2 NMR Experiments Measuring OTO Commutators

We exploit Hamiltonian engineering techniques to investigate the onset of prethermalization in a nuclear spin system in a natural crystal. We can reach both phases by manipulating the relative strengths of the dipolar interactions among spins and the transverse magnetic field. After a quench, we experimentally measure OTO commutators using multiple quantum coherence (MQC) [106, 49, 142]. In the low field regime, the system is thermal and the commutator keeps increasing in the observed timescale. In the high field regime, instead, an emergent conserved quantity arises due to prethermalization and the OTO commutator involving such prethermal conserved quantity saturates after a short time. We further support the interpretation of our experimental results by constructing the prethermal Hamiltonian perturbatively [41, 2]. We numerically observe the divergence of the perturbation series below a certain transverse field threshold, indicating the breakdown of prethermal dynamics and the onset of thermal regime.

We work with nuclear spins in fluorapatite (FAp) [34], an experimental system recently used to show MBL [142]. The ^{19}F spins-1/2 form linear chains in the crystal and are coupled by the magnetic dipolar interaction. A single crystal is placed in a large (7T) magnetic field at room temperature. The ^{19}F spins are initially at thermal equilibrium with respect to the Zeeman energy and commute with the secular dipolar Hamiltonian $H_{\text{dipz}} = \sum_{j,k>j} J_{jk}\big[S_z^j S_z^k - \frac{1}{2}(S_x^j S_x^k + S_y^j S_y^k)\big]$, where $J_{jk} \propto J|j-k|^{-3}$. Here S_α^j $(\alpha = x, y, z)$ are spin-1/2 operators of the j-th ^{19}F spin In the timescales we explore, the system can be approximately treated as an ensemble of identical spin chains [23, 151, 119], since the interchain coupling is ~ 40 times weaker than the intrachain coupling. The coupling to ^{31}P spins in the lattice is refocused by the applied control, and the spin-lattice relaxation effects are negligible ($T_1 \approx 0.8$s). The dynamics of the ^{19}F spins are thus well approximated by a 1D closed quantum system with dipolar couplings. While the corresponding 1D, nearest-neighbor XXZ Hamiltonian is integrable [5, 133, 140], the Hamiltonian we consider can lead to

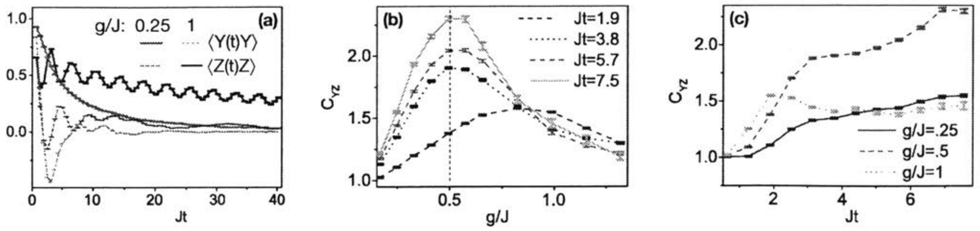

Figure 4-1: (a) Distinct behavior for transverse (Y) and longitudinal (Z) magnetization: $\langle Y(t)Y\rangle$ at $g/J = 0.25$ shows a fast decay as a function of time, indicating thermalization and erasure of initial memory. $\langle Z(t)Z\rangle$ at $g/J = 1$ shows instead slow nonergodic dynamics with periodic oscillations. In the opposite regimes (dashed lines) both correlations quickly decay to zero. (b) $C_{\rm YZ}$ with respect to transverse field strength for $Jt = 1.9$ (purple dashed line), $Jt = 3.8$ (dots), $Jt = 5.7$ (green dashed line) and $Jt = 7.6$ (solid line). (c) $C_{\rm YZ}$ as a function of normalized time, for $g = 0.25$ (solid), $g = 0.5$ (dashed) and $g = 1$ (dots). Here and in the rest of the paper, errorbars are determined from the noise in the free induction decay (see Supplementary Information for details on the experimental scheme). In all experiments we set $u = 0.2$ and a cycle time $\tau_c = 96\mu$s, which corresponds to an effective $J\tau_c = 0.62$, with $J = -uJ_{\rm NN}$ being the engineered nearest-neighbor coupling strength, given the natural $J_{\rm NN} = -33$ krad/s neighbor coupling strength in fluorapatite. Figure prepared by Pai Peng.

diffusive [137, 152] and chaotic behavior [73] in 3D. In the presence of a transverse field, the system is known to show a quantum phase transition [69].

In order to experimentally introduce quenches and time reversal, we modulate $H_{\rm dipz}$ with periodic sequences of strong rf pulse [55] to dynamically engineer an effective (Floquet) transverse field dipolar Hamiltonian [1]:

$$H_{\rm TDip} = u\sum_{j,k>j} J_{jk}\left[S_y^j S_y^k - \frac{1}{2}(S_x^j S_x^k + S_z^j S_z^k)\right] + g\sum_j S_z^j \tag{4.1}$$

where both u and g are under experimental control (for details see Experimental Method section). Whereas for either $g=0$ or $u=0$ the magnetizations $Y = \sum_j S_y^j$ and $Z = \sum_j S_z^j$ are exactly conserved, respectively, for finite values their dynamics is quite different [see Fig. 4-1(a)]. Indeed, $H_{\rm TDip}$ can be mapped to a prethermal Hamiltonian only at high field. As shown in Ref. [1], a prethermal regime exists for Hamiltonians that can be divided into two parts $H = H_0 + \epsilon H_1$, with H_0 having integer

---

[1] Note that the form of this Hamiltonian is reminiscent of a spin-locking dipolar interaction in NMR [134]

eigenvalues, $e^{i2\pi H_0} = 1$. For sufficiently small ϵ, H can be approximately transformed to a prethermal Hamiltonian H_{pre} through a local unitary R, i.e. $RHR^\dagger = H_{\text{pre}} + V$, where V is exponentially small in ϵ and $R = \mathbb{1} + O(\epsilon)$ [2, 38]. As the prethermal Hamiltonian conserves H_0, $R^\dagger H_0 R$ is a conserved quantity in the original frame up to an exponentially long time t_{pre}, after which the small correction V thermalizes the system. In the transverse field dipolar model with $g \gg J$, we can identify the dominant part with the field, $H_0 \equiv Z$, and the perturbation with the dipolar interaction. Then, in the prethermal regime we expect an emergent conserved quantity, Z_{pre}, related to Z by a local unitary transformation R, $Z_{\text{pre}} = R^\dagger Z R$.

To investigate the presence of this emergent constant of motion we experimentally analyze the properties of OTO commutators, defined as $C_{\text{VW}}(t) \equiv \langle [V(t), W][V(t), W]^\dagger \rangle_\beta$, where $V(t) = U(t)VU(t)^\dagger$, with $U(t) = e^{-i\hat{H}t}$ and $\hat{H}$ the system Hamiltonian. Here $\langle \cdot \rangle_\beta = \text{Tr}(e^{-\beta\hat{H}} \cdot)/\text{Tr}(e^{-\beta\hat{H}})$ denotes the ensemble average at the inverse temperature β. The OTO commutator contains a term with an unconventional temporal order, the OTO correlator $F(t) \equiv \langle \hat{V}^\dagger(t)\hat{W}^\dagger V(t)W \rangle_\beta$, which can provide a more accurate description of information scrambling than, e.g., Loschmidt echoes [117, 139, 56, 122, 150, 8, 51, 116]. We exploit our ability to engineer a time reversal of the Hamiltonian in Eq. (4.1) to measure the OTO commutator of extensive observables [86], as we explain in the following.

In room temperature NMR experiments, the initial state for a chain of L spins is described by the density matrix $\rho(0) \approx (\mathbb{1} - \epsilon Z)/2^L$, with $\epsilon \sim 10^{-5}$. Since the identity operator does not contribute to any measurable signal, we only care about the difference $\rho(0) - \mathbb{1}/2^L \propto \delta\rho = 2Z/\sqrt{L}$, which has been normalized such that $\text{Tr}(\delta\rho^2)/2^L = 1$. MQC experiments [106, 17, 120] measure the overlap of the time-evolved density matrix, $\delta\rho(t) = U(t)\delta\rho(0)U^\dagger(t)$, with itself after a collective rotation. The overall measured signal can be expressed as

$$S_\phi = 2^{-L}\text{Tr}[e^{-i\phi\mathcal{O}_{\mathbf{n}}}\delta\rho(t)e^{i\phi\mathcal{O}_{\mathbf{n}}}\delta\rho(t)] \tag{4.2}$$

where $\mathcal{O}_{\mathbf{n}} = \sum_j \mathbf{n} \cdot \boldsymbol{S}_j$ is the collective spin magnetization along $\mathbf{n}$. Taking a discrete

Fourier transform of S_ϕ with respect to ϕ yields the MQC intensities: $S_\phi = \sum_q e^{-iq\phi} I_q$. Expanding S_ϕ in powers of ϕ, it can be shown that the commutator norm between $\delta\rho(t)$ and $\mathcal{O}_{\mathbf{n}}$ is given by $\mathrm{Tr}([\delta\rho(t), \mathcal{O}_{\mathbf{n}}]^2)/2^L = -\sum_q q^2 I_q$. Since $\delta\rho(0)$ is usually the collective spin magnetization pointing in some direction, $\mathcal{O}_{\mathbf{n}'}$, we can write

$$C_{\mathcal{O}_{\mathbf{n}'}\mathcal{O}_{\mathbf{n}}}(t) = \frac{4}{L}\langle |[\mathcal{O}_{\mathbf{n}'}(t), \mathcal{O}_{\mathbf{n}}]|^2 \rangle_{\beta=0} = \sum_q q^2 I_q \tag{4.3}$$

Eq. (4.3) is the central idea of our experiments: by measuring the second moment of the MQC intensities encoded in $\delta\rho(t)$ along $\mathcal{O}_{\mathbf{n}}$ one can obtain the OTO commutator between $\mathcal{O}_{\mathbf{n}'}(t)$ and $\mathcal{O}_{\mathbf{n}}$ as if the system were at infinite temperature [2]. Eq. (4.3) was first derived in Ref. [77] for NMR systems. When applied to pure states dynamics, it relates the second moment of the MQC distribution to the quantum Fisher information [49].

To study the system dynamics after a quench to Hamiltonian (4.1), we measure the OTO commutator $C_{\mathrm{YZ}} \equiv 4L^{-1}\langle |[Y(t), Z]|^2 \rangle_{\beta=0}$ for various transverse field strengths and times [see Fig. 4-1]. First note that in the limit $g \to \infty$, Z would become a conserved quantity thus making C_{YZ} constant. For large but finite transverse field, we observe that C_{YZ} stops growing at an early time, revealing that Z is approaching the emergent conserved quantity, as also revealed by the two point correlator $\langle Z(t)Z \rangle$ [Fig. 4-1(a)]. For small transverse field, instead, C_{YZ} keeps increasing, suggesting that the system is thermal [Fig. 4-1(c)]. Notice that in the limit of exactly no transverse field, Y is a conserved quantity thus making C_{YZ} constant. However, as long as a small field is introduced the system becomes thermal, as indicated by the decay of $\langle Y(t)Y \rangle$ in Fig. 4-1(a) and further demonstrated below.

To gain further insight into the differences between the thermalizing and prethermal regimes, we measure C_{ZZ} and C_{YY}, as shown in Fig. 4-2(a). Because these OTO commutators fluctuate significantly in time, we average it at six different times. As g increases, $Z(t)$ approaches the prethermal conserved quantity Z_{pre}, which itself

---

[2] Notice that exchanging $\mathcal{O}_{\mathbf{n}'}$ and $\mathcal{O}_{\mathbf{n}}$ will result in a different MQC distribution I_q, however its second moment remains the same.

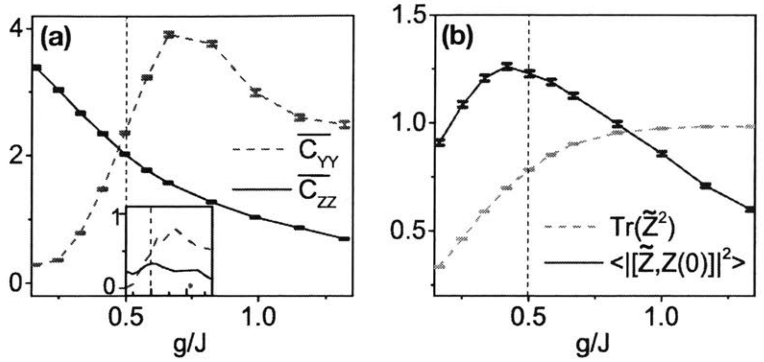

Figure 4-2: (a) Averaged C_{YY} (dashed) and C_{ZZ} (solid) with respect to transverse field strength. (b) $\mathrm{Tr}(\widetilde{Z}^2)$ (dashed) and $\langle|[\widetilde{Z}, Z(0)]|^2\rangle$ (solid) versus transverse field strength. The inset shows the standard deviation. The time average is taken over the values $Jt = 3.77, 5.02, 6.28, 7.54, 8.80, 10.05$, with the longest time corresponding to 16 cycles. Figure prepared by Pai Peng.

approaches Z, and C_{ZZ} gets smaller. This behavior is only observed for OTO commutators involving at least one operator that overlaps with the emergent conserved quantity, while other commutators, such as C_{YY}, keep growing as if the system were thermal, regardless of the transverse field strength (with the exception of exactly zero field, $g = 0$).

We can further analyze another quantity that has recently been proposed for detecting the MBL to ergodic phase transition [26], the time-averaged operator $\overline{Z} = t_{\mathrm{pre}}^{-1} \int_0^{t_{\mathrm{pre}}} Z(t)dt$, where t_{pre} is the timescale over which the prethermal conserved quantity is present. While we cannot experimentally measure $\overline{Z}$, we can approximate it with a discrete time average, $\widetilde{Z} = \sum_{n=1}^{N} Z(t_n)/N$, by independently varying the forward and backward evolution times in the MQC protocol (see Experimental Method section). In the limit $t_{\mathrm{pre}} \to \infty$, $\overline{Z}$ becomes an exact integral of motion. Even for finite-time averaging, $\overline{Z}$ (and its approximation $\widetilde{Z}$) captures the essential features of the conserved quantity Z_{pre}. Indeed, we can generally write $Z(t) = Z_{\mathrm{pre}} + U(t)(Z - R^{\dagger}ZR)U(t)^{\dagger}$: then, in the prethermal regime, the second term is small, yielding $\overline{Z} \approx Z_{\mathrm{pre}}$ after time average (see Extended Data section for a comparison between $\overline{Z}$ and $\widetilde{Z}$). Figure 4-2(b) shows that $\mathrm{Tr}(\widetilde{Z}^2)/\mathrm{Tr}(Z(0)^2)$ approaches unity as g increases, because the time-varying part of Z is very small for large g. Furthermore, $4/L\langle|[\widetilde{Z}, Z(0)]|^2\rangle_{\beta=0}$ approaches zero at large g, suggesting that

$\lim_{g\to\infty}\widetilde{Z} = Z$.

4.3 Emergent Conserved Quantity

To further demonstrate that a conserved quantity emerges for large g, we simulate Z at large times ($t = 10^3$) and decompose it according to the Hamming weight [142]

$$Z(t = 10^3) = \sqrt{2^{L-2}L} \sum_{k=1}^{L} \sum_{s=1}^{\zeta_k} b_k^s(t) \mathcal{B}_k^s, \tag{4.4}$$

where $\mathcal{B}_k^s$ are operators composed of tensor products of k Pauli matrices and $L - k$ identity operators, and $\zeta_k \propto 3^k \times \binom{L}{k}$ labels the number of configurations with k non-identity Pauli operators. We define the Hamming weight of k-spin correlations as $f_k = \sum_{s=1}^{\zeta_k} [b_k^s]^2$, satisfying $\sum_{k=1}^{L} f_k = 1$. Figure 4-4(b) shows that for small transverse field f_k is approximately proportional to ζ_k, suggesting that all possible operators $\mathcal{B}_k^s$ have the same weight, in agreement with the eigenvalue thermalization hypothesis [61, 123, 35, 138]. The result is qualitatively different for $g \gg 1$, where a significant one-body term, f_1, exists even at very late times ($Jt = 10^3$), signifying the failure of thermalization and the emergence of the conserved quantity Z_{pre}. We thus study f_1 as a function of time. For small fields, $g/J \leq 0.5$, the contribution of f_1 in $Z(t)$ quickly relaxes from 1 to zero, as shown in Fig. 4-4(c). For large g/J, instead, f_1 reaches a non-zero, quasi-equilibrium value, signaling the prethermal phase. We do not see the final thermalizing stage in the numerics, possibly because small systems, $L = 13$, do not fully thermalize [99]. Interestingly, as shown in Fig. 4-3the numerically calculated $-4/L\langle [\overline{Z}_{\text{inf}}, S_\alpha]^2 \rangle_{\beta=0}$, with $\overline{Z}_{\text{inf}}$ being the infinite time average of $Z(t)$ and S_α being either X, Y, or Z, shows size-independent behavior (up to $L = 14$) for large g. This tantalizingly suggests that Z_{pre} may be exactly conserved, i.e., $n^* = \infty$ [42]. On the other hand while Y is conserved at exactly zero field ($g = 0$), as soon as a small transverse field is introduced the contribution of f_1 to $Y(t)$ decays to zero [Fig. 4-4(d)]. This indicates that the slow dynamics observed for $Y(t)$ at small g is not protected by any prethermal conserved quantity, and will thus thermalize on

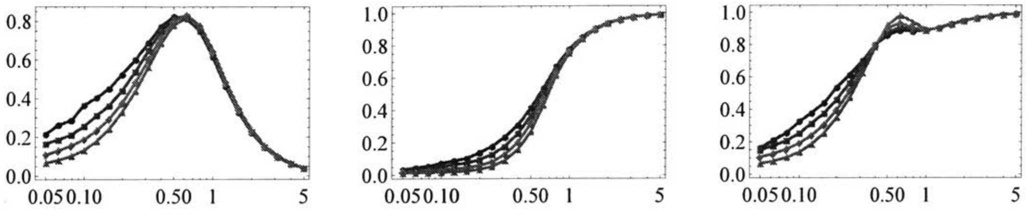

Figure 4-3: **Numerically simulated OTO commutator involving $\overline{Z}_{\text{inf}}$** The commutators between $\overline{Z}_{\text{inf}}$ and Z (left), Y (middle), X (right) are calculated as a function of g for system sizes L =8, 10, 12, 14. For large g, the commutator show little to no dependence on L.

timescales much shorter than t_{pre}. The quantitative difference between f_1 for $Y(t)$ and $Z(t)$ can be approximately observed by measuring the two-point correlations $4\text{Tr}(Z(t)Z)/2^L L$ and $4\text{Tr}(Y(t)Y)/2^L L$. As shown in Figure 4-1(a), in the small field regime $4\text{Tr}(Y(t)Y)/2^L L$ decreases rapidly as a function of time, suggesting that $f_1(t)$ of $Y(t)$ is not a (prethermal) conserved quantity [3]. In stark contrast, $4\text{Tr}(Z(t)Z)/2^L L$ shows a slow decay with periodic oscillations as a function time, suggesting that $f_1(t)$ of $Z(t)$ is mostly conserved, consistent with prethermalization at large g/J [4].

We will further validate our experimental results numerically, by constructing the prethermal Hamiltonian and verifying the emergence of a conserved quantity at high field, while in the low field regime the dynamics is consistent with thermalization. We demonstrate the value of OTO commutators in investigating non-equilibrium quantum thermodynamics, while also providing a method to experimentally measure OTO commutators that could be extended to other experimental platforms. Similar techniques could be used for example to explore other many-body phenomena, such as localization, dynamics phase transition and information scrambling, paving the way to more comprehensive understanding of out-of-equilibrium quantum many-body systems.

---

[3] We further numerically demonstrate in the next section that H is unlikely to be in a prethermal regime with respect to NN Ising interactions $\sum_j S_y^j S_y^{j+1}$, the dominant term in H_{TDip} for small values of g.

[4] taking the average over time, also shows that $\overline{Z} \approx Z$ in the prethermal regime

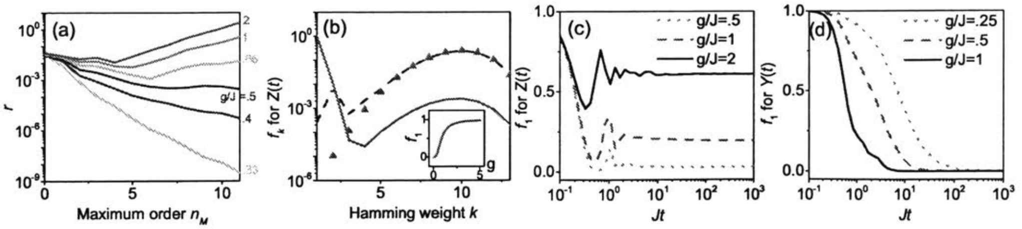

Figure 4-4: (a) Eigenvalue difference r with respect to maximum order n_M for different values of g/J. r shows a convergence, up to a maximum field value $g/J = 0.5$. (b) Decomposition of $Z(t)$ (obtained by exact diagonalization) at $t = 10^3$ according to the operator Hamming weight: f_k is the contribution of all possible spin correlations with Hamming weight k. For small fields, $g/J = 0.05$ (dashed line), the result follows closely the distribution (triangles) obtained randomly sampling all possible operators. For large fields, $g/J = 5$ (solid line) there is a significant contribution of single-body terms, related to the quasi-conserved quantity Z_{pre}. In the inset: f_1 as a function of g. f_1 for $Z(t)$ (c) and $Y(t)$ (d) as a function of normalized time, showing the nonthermal behavior of Z at large g/J, while Y is always thermal even for small g/J. The system size is $L = 12$ for (a) and 13 for (b–d). Figure prepared by Pai Peng

4.4 Prethermalization

To support our interpretation of the experimental results, we explicitly construct the prethermal Hamiltonian, showing that indeed $Z_{\text{pre}} \approx Z$ is an emergent constant of motion. The prethermal Hamiltonian can be expanded in powers of $\epsilon = J/g$

$$H_{\text{pre}} = Z + \sum_{n=1}^{n_M} \epsilon^n h^{(n)}, \tag{4.5}$$

and numerically evaluated up to max order n_M. It has been shown [2] that for generic many-body systems the series in Eq. (4.8) might not converge as $n_M \to \infty$, but there exists an optimal order n^*, so that H_{pre} is most similar to H when truncating the series at n^*. If the system Hamiltonian does indeed support a prethermal phase, we expect its eigenvalues E_m to be close to the prethermal Hamiltonian ones, E_m^{pre}. We thus calculate the eigenvalue difference $r \equiv \text{mean}_m(E_m - E_m^{\text{pre}})/L$ (where m labels the eigenvalues in ascending order), expecting r to converge to zero only in the prethermal phase. Figure 4-4(a) shows r as a function of maximum truncation order n_M for different values of ϵ.

4.4.1 Constructing the Prethermal Hamiltonian

In this section the mathematical framework for prethermalization in time-independent systems is reviewed. The derivations are based on Abanin et al. [2], but uses a different approach to calculate the higher order correlations to the prethermal Hamiltonian. In prethermal systems, certain observables can exhibit slow, nonergodic, dynamics even in the absence of any disorder. The reason for this is that the prethermal Hamiltonian has a emergent symmetry given by $[H_{\text{pre}}, D] = 0$ which is preserved for an exponentially long prethermal time. Thus, any operator that overlaps with D' will have slow dynamics due to the emergent symmetry. The exponential timescale for t_{pre} has been proved rigorously for both time-dependent and independent systems in [2].

To begin, it is useful to divide the transverse field dipolar Hamiltonian into two parts: $H_{\text{TDip}} = H_1 + H_0$, where

$$H_0 = \sum_j S_z^j, \qquad H_1 = u \sum_{j,k>j} J_{jk} \left[S_y^j S_y^k - \frac{1}{2}(S_x^j S_x^k + S_z^j S_z^k) \right] \tag{4.6}$$

where ϵ is a small parameter. The idea is to perform an unitary transformation to bring the Hamiltonian into the following form

$$UHU^\dagger = H_0 + D + V = H_{\text{pre}} + V \tag{4.7}$$

where $[D, H_0] = 0$, $[V, H_{\text{pre}}] \neq 0$, and $H_{\text{pre}} = H_0 + D$. If V is zero, then $U^\dagger H_{\text{pre}} U$ is an exact conserved quantity. Any operators not orthogonal to $U^\dagger H_{\text{pre}} U$ will have some finite component conserved up to infinite times, and the prethermal time t_{pre} is infinity. If however V is nonzero but exponentially small compared to H_{pre}, then $U^\dagger H_{\text{pre}} U$ is an emergent symmetry conserved only up to t_{pre}.

In order to calculate the prethermal effective Hamiltonian H_{pre}, let $U = e^S$ and expand S, D, and V in powers of ϵ:

$$S = \sum_{j=1} \epsilon^j S_j, \qquad D = \sum_{j=1} \epsilon^j D_j, \qquad V = \sum_{j=1} \epsilon^j V_j$$

Once D_j are found the prethermal effective Hamiltonian up to n_M-th order is given by

$$H_{\text{pre}} = H_0 + \sum_{j=1}^{n_M} \epsilon^j D_j \tag{4.8}$$

It is not known whether the series in Eq.(4.8) will converge for any ϵ when $n_M \to \infty$. When the series does converge then prethermal Hamiltonian is an exact symmetry.

It is instructive to see how to solve this perturbation series iteratively. Using the Baker-Campbell-Hausdorff formula

$$e^S H e^{-S} = H + [S,H] + \frac{1}{2!}[S,[S,H]] + \frac{1}{3!}[S,[S,[S,H]]] + \frac{1}{4!}[S,[S,[S,[S,H]]]] + \cdots$$

on the LHS of Eq.(4.7) and collect terms with same order of ϵ, it can be shown that the equations up to ϵ^5 are given by

$$\begin{aligned}
D_1 + V_1 &= [S_1, H_0] + H_1 \\
D_2 + V_2 &= [S_2, H_0] + [S_1, H_1] + \frac{1}{2}[S_1, [S_1, H_0] \\
D_3 + V_3 &= [S_3, H_0] + [S_2, H_1] + \frac{1}{2}([S_1, [S_2, H_0]] + 1 \leftrightarrow 2) + \frac{1}{2}[S_1, [S_1, H_1]] \\
&\quad + \frac{1}{6}[S_1, [S_1, [S_1, H_0]]] \\
D_4 + V_4 &= [S_4, H_0] + [S_3, H_1] + \frac{1}{2}([S_1, [S_3, H_0]] + 1 \leftrightarrow 3) + \frac{1}{2}[S_2, [S_2, H_0]] \\
&\quad + \frac{1}{2}([S_1, [S_2, H_1]] + 1 \leftrightarrow 2) + \frac{1}{6}([S_2, [S_1, [S_1, H_0]]] + 1 \leftrightarrow 2) \\
&\quad + \frac{1}{6}[S_1, [S_1, [S_1, H_1]]] + \frac{1}{24}[S_1, [S_1, [S_1, [S_1, H_0]]]] \\
D_5 + V_5 &= [S_5, H_0] + [S_4, H_1] + \frac{1}{2}([S_1, [S_4, H_0]] + 1 \leftrightarrow 4) + \frac{1}{2}([S_2, [S_3, H_0]] + 2 \leftrightarrow 3) \\
&\quad + \frac{1}{2}([S_1, [S_3, H_1]] + 1 \leftrightarrow 3) + \frac{1}{2}[S_2, [S_2, H_1]] + \frac{1}{6}([S_2, [S_2, [S_1, H_0]]] + 1 \leftrightarrow 2)
\end{aligned}$$

$$
\begin{aligned}
&+\frac{1}{6}([S_3,[S_1,[S_1,H_0]]]+1\leftrightarrow 3)+\frac{1}{6}([S_2,[S_1,[S_1,H_1]]]+1\leftrightarrow 2)\\
&+\frac{1}{24}([S_1,[S_1,[S_1,[S_2,H_0]]]]+1\leftrightarrow 2)+\frac{1}{24}[S_1,[S_1,[S_1,[S_1,H_1]]]]\\
&+\frac{1}{120}[S_1,[S_1,[S_1,[S_1,[S_1,H_0]]]]]\\
&\vdots
\end{aligned}
$$

where $i \leftrightarrow j$ indicates permutation of S_i and S_k in the commutators. Starting at first order in ϵ, all terms on the RHS besides $[S_j, H_0]$, call it h_j, are split into two parts, the part that commutes with H_0 is stored in D_j. S_j is then chosen such that $[S_j, H_0]$ exactly cancels the other part that does not commute with H_0, this automatically makes $V_j = 0$. The iteration is repeated in the next order.

Since H_0 satisfies $e^{2im\pi H_0} \propto \mathbb{1}$, one can use the same approach for calculating MQC components described in Chapter 1 to systematically find D_j and S_j. At each order, decompose h_j to its MQC components: $h_j = \sum_q h_{jq}$, where $[H_0, h_{jq}] = qh_{jq}$, and find them using Eq.(1.15). In terms of h_{jq}, D_j and S_j can be written as

$$D_j = h_{j0}, \qquad S_j = \sum_{q>0} q^{-1}(h_{jq} - h_{j(-q)}) \tag{4.9}$$

The MQC components h_{jq} are referred to as generalized ladder operators in [93]. The problem of finding prethermal Hamiltonian is intimately related to finding the slowest operators, or the operators that best commutes with the Hamiltonian [78, 93].

4.4.2 No Prethermalization for Small g

Here we explore whether the Hamiltonian in Eq.(1) can be prethermal for small values of g. In the main text, it is shown that a prethermal Hamiltonian cannot be generated using $H_0 = Z$ for small g. Another possible prethermal generator is $H_0 = \sum_j 2S_y^j S_y^{j+1}$. Following the method given in the previous section, we construct the prethermal Hamilontian order by order, and calculate the mean eigenvalue difference between the prethermal Hamiltonian and the original Hamiltonian. The eigenvalue difference r stops decreasing after $n_M > 2$ even for moderate transverse field strength [Fig.

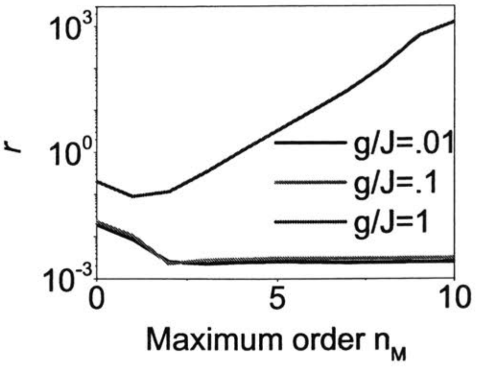

Figure 4-5: (a) Eigenvalue difference, r with respect to maximum order, n_M, for varying values of g/J. r fails to decrease after second order. The system size is $L = 11$.

1(c)], while for large transverse field it diverges as expected. The prethermalization theory fails to apply to small field regime because even with only dipolar interaction $||H_0|| \approx ||H_1||$, thus the series expansion does not converge.

For large g, $r \approx 0$ appears to converge up to the largest numerically accessible order, suggesting that H_{pre} is similar to H and there exists an approximately conserved quantity Z_{pre}. For small g however, r diverges, indicating that a prethermal Hamiltonian that conserves Z cannot be found. The transition happens at around $g/J = 0.5$.

4.5 Experimental Methods

The pulse sequence used in this Chapter is based on modifying the general 16-pulse sequence described in Chapter 1.

4.5.1 Hamiltonian Engineering

Using the forward sequence

$$P(\tau_1, \mathbf{x}, \tau_2, \mathbf{y}, 2\tau_1, \mathbf{y}, \tau_2, \mathbf{x}, \tau_1)P(\tau_1, \mathbf{x}, \tau_2, \mathbf{y}, 2\tau_1, \mathbf{y}, \tau_2, \mathbf{x}, \tau_1)P(\tau_1, \bar{\mathbf{x}}, \tau_2, \bar{\mathbf{y}}, 2\tau_1, \bar{\mathbf{y}}, \tau_2, \bar{\mathbf{x}}, \tau_1)P(\tau_1, \bar{\mathbf{x}}, \tau_2, \bar{\mathbf{y}}, 2\tau_1, \bar{\mathbf{y}}, \tau_2, \bar{\mathbf{x}}, \tau_1)$$

and the backward sequence

$$P(\tau_3, \mathbf{y}, \tau_3, \mathbf{x}, 2\tau_4, \mathbf{x}, \tau_3, \mathbf{y}, \tau_3)P(\tau_3, \mathbf{y}, \tau_3, \mathbf{x}, 2\tau_4, \mathbf{x}, \tau_3, \mathbf{y}, \tau_3)P(\tau_3, \bar{\mathbf{y}}, \tau_3, \bar{\mathbf{x}}, 2\tau_4, \bar{\mathbf{x}}, \tau_3, \bar{\mathbf{y}}, \tau_3)P(\tau_3, \bar{\mathbf{y}}, \tau_3, \bar{\mathbf{x}}, 2\tau_4, \bar{\mathbf{x}}, \tau_3, \bar{\mathbf{y}}, \tau_3)$$

with the delays are given by

$$\tau_1 = \tau(1-u), \quad \tau_2 = \tau(1+2u), \quad \tau_3 = \tau(1+u), \quad \tau_4 = \tau(1-2u)$$

we can engineer a dipolar Hamiltonian along the y direction with opposite sign:

$$H_0 = \pm u \sum_{j<k} J_{jk} \left[S_y^j S_y^k - \frac{1}{2}(S_x^j S_x^k + S_z^j S_z^k) \right],$$

and $H_1 = 0$ (the first order can always be set to zero by a proper symmetrization of the sequence). The average Hamiltonian corresponding to the forward sequence is presented as Eq.(1) in section. As described in Chapter 1, a uniform transverse field can be introduced in H_0 by phase shifting the pulse sequences. The strength of the field is controlled by the angle of rotation and the cycle time τ_c of the sequence, where as sign of the field is controlled by the direction of the rotation.

4.5.2 Measuring OTO Commutators Involving Integrals of Motion

We are interested in measuring the OTO commutator $C_{\mathcal{O}_{\text{inf}}\mathcal{O}'} = -4L^{-1}\langle[\mathcal{O}_{\text{inf}}, \mathcal{O}']^2\rangle_{\beta=0}$, where the integral of motion $\mathcal{O}_{\text{inf}}$ is given by the infinite time average of operator $\mathcal{O}(t)$: $\mathcal{O}_{\text{inf}} = \lim_{\tau\to\infty} \frac{1}{\tau}\int_0^\tau dt\mathcal{O}(t)$. This commutator can be found by measuring the MQC intensities with different forward and backward evolution times. The measured signal in MQC experiments is given by

$$S_\phi(t_1, t_2) = 2^{-L}\text{Tr}[e^{-i\phi\mathcal{O}'}\mathcal{O}(t_1)e^{i\phi\mathcal{O}'}\mathcal{O}(t_2)] = \sum_q e^{-iq\phi}I_q(t_1, t_2)$$

where t_1 and t_2 are now independent. Integrate both sides with respect to t_1 and t_2 and take the infinite limit gives

$$2^{-L}\mathrm{Tr}[e^{-i\phi\mathcal{O}'}\mathcal{O}_{\text{inf}}e^{i\phi\mathcal{O}'}\mathcal{O}_{\text{inf}}] = \sum_q e^{-iq\phi} \lim_{\tau_1,\tau_2\to\infty}\frac{1}{\tau_1\tau_2}\int_0^{\tau_1}\int_0^{\tau_2} I_q(t_1,t_2)dt_1dt_2$$

expand both sides with respect to ϕ and equate terms in ϕ^2 gives

$$C_{\mathcal{O}_{\text{inf}}\mathcal{O}'} = -4L^{-1}\langle[\mathcal{O}_{\text{inf}},\mathcal{O}']^2\rangle_{\beta=0} = \sum_q q^2 \lim_{\tau_1,\tau_2\to\infty}\frac{1}{\tau_1\tau_2}\int_0^{\tau_1}\int_0^{\tau_2} I_q(t_1,t_2)dt_1dt_2$$

In the experiments we can only measure $I_q(t_1,t_2)$ at discrete time points. If we replace the integrals by discrete sums we can measure

$$C_{\bar{\mathcal{O}}\mathcal{O}'} = -4L^{-1}\langle[\bar{\mathcal{O}},\mathcal{O}']^2\rangle_{\beta=0} = \sum_q \frac{q^2}{M^2}\sum_j^M\sum_k^M I_q(j\Delta t, k\Delta t)$$

where $\bar{\mathcal{O}} = \frac{1}{M}\sum_j \mathcal{O}(j\Delta t)$ is a discrete time average of $\mathcal{O}(t)$. $\bar{\mathcal{O}}$ can be used as an approximation for the integral of motion $\mathcal{O}_{\text{inf}}$.

4.6 Extended Data and Numerical Simulations

4.6.1 Experimental Data for $C_{\bar{Z}Z}$ with Disorder

Here the OTO commutator $C_{\bar{Z}Z}$ is measured with disorder introduced into the Hamiltonian, the goal is to that the transition observed is robust to perturbations. The modified dipolar Hamiltonian is given by $H_{\text{mTDip}} = H_{\text{TDip}} + \lambda\sum_j h_j(S_x^j + S_y^j)/\sqrt{2}$. As shown in Fig. 4-6, the transition appears to stay around $g/J \approx 0.5$, but the overall value is smaller than the case without disorder. This suggests that the observed transition has a certain degree of robustness to random perturbation.

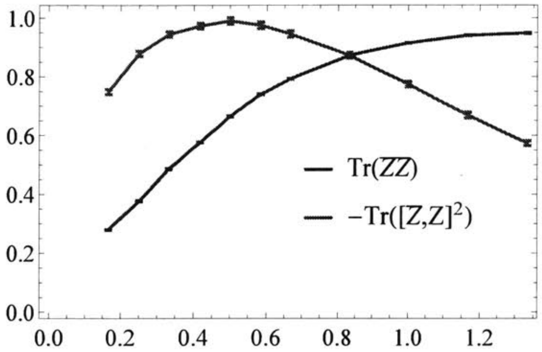

Figure 4-6: Experimentally measured $C_{\bar{Z}Z}$ with disordered field introduced in the $x + y$ direction. In the data $\lambda = 0.08$

4.6.2 Experimental Data for $C_{YY}(t)$ and $C_{ZZ}(t)$

Here we show the experimentally measured $C_{YY}(t)$ and $C_{ZZ}(t)$ at six different times, whose averaged value is presented in Fig. 1(c) in the main text.

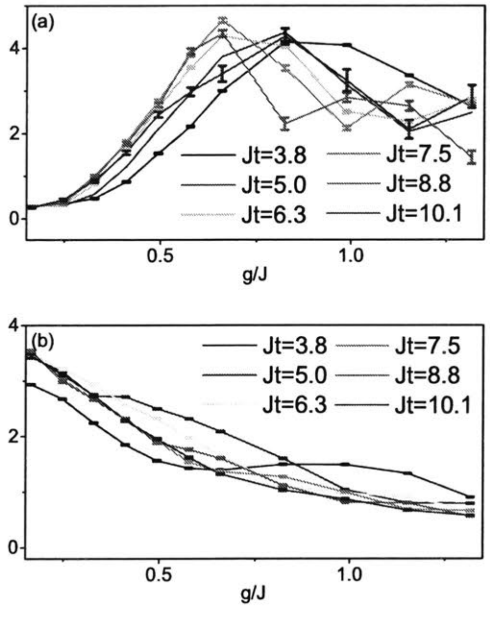

Figure 4-7: Experimentally measured $C_{YY}(t)$ (a) and $C_{ZZ}(t)$ (b) versus transverse field at different times. Figure prepared by Pai Peng

4.6.3 Experimental Data for Tr$(Z(t)Z)$ and Tr$(Y(t)Y)$

The extended data for Tr$(Z(t)Z)$ and Tr$(Y(t)Y)$ is shown in Fig. 4-8. The Tr$(Z(t)Z)$ exhibits oscillations on top of a decay. After averaging over one oscillation period, Tr$(Z(t)Z)$ can be fitted to an exponential function $Ae^{-\gamma Jt}$, where γ is the dimensionless decay rate. Figure 4-8(c) shows the decay rate γ of Tr$(Z(t)Z)$ can be approximated by an exponential function of field strength J/g, i.e. $\gamma = \gamma_0 e^{-\alpha g/J} + \gamma_\infty$, where γ_∞ is a trivial decay in the experiments that is independent of g. This exponentially slow decay agrees with the theory for Floquet prethermalization [42, 40, 2]. Tr$(Y(t)Y)$ shows exponential decay at small g/J [Fig. 4-8(b)], whose decay rate is shown in Fig. 4-8(d). The scaling for the decay rate of Tr$(Y(t)Y)$ cannot be extracted due to limited data points.

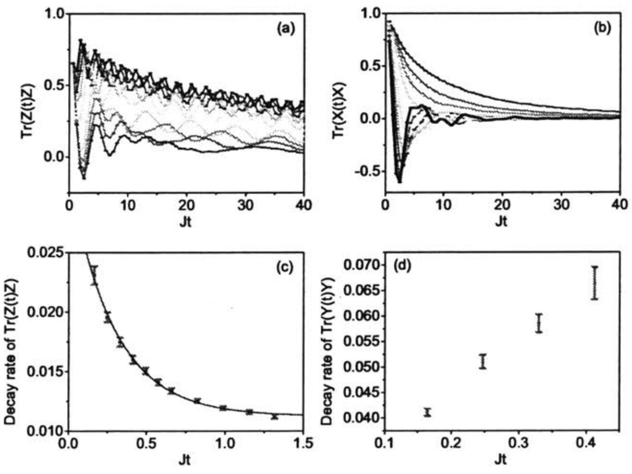

Figure 4-8: Experimentally measured Tr$(Z(t)Z)$ (a) and Tr$(Y(t)Y)$ (b) versus time, with transverse field strength g/J=$\{0.16, 0.25, 0.33, 0.41, 0.49, 0.58, 0.66, 0.82, 0.99, 1.2, 1.3\}$. Blue color represents larger field while red color represents smaller field. (c) Red markers show the decay rate of Tr$(Z(t)Z)$ as a function of field strength J/g. The error bar includes only fitting uncertainty, not including the uncertainty of the raw data. The decay rate can be fitted to an exponential function (blue curve). (d) Decay rate of Tr$(Y(t)Y)$ as a function of field strength J/g. For $J/g > 0.41$, Tr$(Y(t)Y)$ cannot be fitted to an exponential function. Figure and fit done by Pai Peng

4.6.4 Numerical Results

In this section we show the numerical results of OTO commutators using exact diagonalization (Fig. 4-9). System size $L = 12$ and open boundary condition are used here. In comparison with Fig. 4-1 in the main text (reproduced here in (e)-(h) in Fig. 4-9), the numerical and experimental results show quantitatively similar behavior. The difference is mainly due to experimental imperfections and decoherence, as well as the finite size effect in simulation and finite MQC encodings in experiments. In Fig. Fig. 4-9d, we calculated Z_{inf} exactly by taking the diagonal ensemble in the eigenbasis: $Z_{\text{inf}} = \sum_n Z_{nn} |n\rangle\langle n|$, where $|n\rangle$ is an eigenvector of the Hamiltonian. The measured data in Fig. 4-9(h) overestimates Fig. 4-9(d) due to finite discrete averaging.

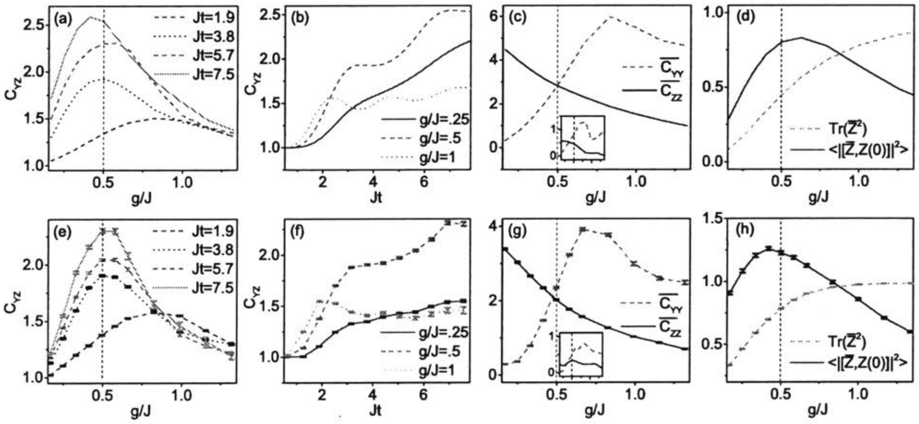

Figure 4-9: (a) C_{YZ} with respect to transverse field strength for $Jt = 1.9$ (purple dashed line), $Jt = 3.8$ (dots), $Jt = 5.7$ (green dashed line) and $Jt = 7.6$ (solid line). (b) C_{YZ} as a function of normalized time, for $g = 0.25$ (solid), $g = 0.5$ (dashed) and $g = 1$ (dots). (c) Averaged C_{YY} (dashed) and C_{ZZ} (solid) with respect to transverse field strength. The time average is taken over the values $Jt = 3.77, 5.02, 6.28, 7.54, 8.80, 10.05$.The inset shows the standard deviation. (d) $\text{Tr}(\bar{Z}^2)$ (dashed) and $\langle |[\bar{Z}, Z(0)]|^2 \rangle$ (solid) versus transverse field strength. The average is taken by keeping only the diagonal matrix elements of Z in the eigenbasis of H. (e)-(h) are the copy of Fig.(4-1) for comparison. Figure prepared by Pai Peng.

4.7 Conclusion

In conclusion, we studied the out-of-equilibrium dynamics of the transverse field dipolar interaction in a solid-state NMR quantum simulator. Using MQC techniques, we measured OTO commutators to reveal a distinct dynamics in the high and low field regimes, and identified them as prethermal and thermal phases. In the prethermal regime, when one of the OTO operators is the emergent quasi-conserved quantity, the OTO commutator saturates at an early time, while it keeps increasing in the thermal regime, with a transition at about $g/J = 0.5$ [5].

It is natural to wonder if this critical point has the same origin as the one found in H_{TFI} described in the last Chapter, namely that H_{TDip} can be transformed into a H_{eff} with long ranged interactions at the critical point. This is difficult to detect numerically because the prethermal expansion for H_{TDip} is perturbative, and thus cannot be applied when g is comparable to J.

---

[5] we note that this value does not corresponds to the critical point of the equilibrium quantum phase transition [69]

Chapter 5

Future Directions

One immediate application based on the techniques developed in the previous two chapters is to experimentally explore the MBL-ergodic phase transition in one and more dimensions. Since OTO commutators can reveal information about the spatial extent of correlations, and the MBL-ergodic transition is marked by a divergence in the spatial extent of integrals of motion, by measuring OTO commutators of integrals of motion one can experimentally probe the MBL-ergodic phase transition. Since this approach does not rely on individual control over the spins, it can be extended to 3-dimensional systems, where the existence and stability of a MBL phase is still an open question.

5.1 OTO Commutator in Disordered Heisenberg Chain

The Hensenberg chain in a disordered field is perhaps the most studied model for MBL-ergodic phase transition [15, 14, 109, 111, 68, 112]. The model is described by the Hamiltonian:

$$H = J\sum_j \mathbf{S}_j \cdot \mathbf{S}_{j+1} + \sum_j h_j S_z, \tag{5.1}$$

where h_j is a random variable with zero mean and a variance of W. The critical disorder strength for the MBL-ergodic transition for this model is predicted to be around $W_c/J \approx 3.5$. For $W/J \gg 3.5$ [111, 112], the model is in the fully many-body localized (fMBL) phase, where the Hamiltonian can be expressed as

$$H = \sum_j H_j \tau_z^j + \sum_{jk} H_{jk} \tau_z^j \tau_z^k + \sum_{jkl} H_{jkl} \tau_z^j \tau_z^k \tau_z^l + \cdots \tag{5.2}$$

where τ_z^j are the integrals of motions (l-bits) satisfying $[\tau_z^j, \tau_z^k] = 0$. In addition the coupling between the l-bits are exponentially small in distance: $H_{jk} \propto \exp\left(\frac{-|j-k|}{\xi}\right)$, where ξ is the characteristic length of the l-bit [65, 66, 131]. In the fMBL phase τ_z^j have strong overlaps with local physical spins (p-bits). The exponential "dressing" of the l-bits in terms of the p-bits have been verified numerically in a number papers [26], it is precisely this exponential dressing that is responsible for the logarithmic growth in entanglement entropy. In the fMBL phase ξ is expected to be independent of L for large L. In approaching the transition from MBL side, ξ is expected to diverge, as the l-bits becomes more nonlocal.

While the l-bits are attractive from a theoretical point of view, they are difficult to measure experimentally. Numerical constructions of l-bits are also highly nontrivial [126, 118, 68]. A promising alternative to l-bits is using infinite time averaged local operators [26], such as

$$\overline{S}_z^j = \lim_{\mathcal{T}\to\infty} \frac{1}{\mathcal{T}} \int_0^{\mathcal{T}} e^{-iHt} S_z^j e^{iHt} dt = \sum_n (S_z^j)_{nn} |n\rangle\langle n| \tag{5.3}$$

where $|n\rangle$ is an eigenstate of H and $(S_z^j)_{nn} = \langle n|S_z^j|n\rangle$. It follows that $[\overline{S}_z^j, \overline{S}_z^k] = 0$ and $[\overline{S}_z^j, H] = 0$, however unlike the l-bits $\overline{S}_z^j$ does not satisfy a Pauli algebra. In order to probe the structure of $\overline{S}_z^j$ across the MBL-ergodic transition, one can study the behavior of the following commutator as a function of the disorder strength.

$$C_{\bar{Z}_s Z_s} = \frac{-1}{2^{L+2}L} \mathrm{Tr}[\bar{Z}_s, Z_s]^2 \tag{5.4}$$

where $Z_s = \sum_j (-)^j S_z^j$ is the total staggered magnetization and $\bar{Z}_s$ is the infinite time averaged operator of Z_s [1]. The way to measure these kinds of commutators in the NMR system have been described in Chapter 3. It is useful to first examine the behavior of $C_{\bar{Z}_s Z_s}$ in the limits of weak and large disorder. In the fMBL phase, $\bar{Z}_s$ has a big overlap with Z_s and the commutator between them is small, so one expects $C_{\bar{Z}_s Z_s}$ to approach zero in the limit of infinite disorder. On the other hand, deep in the ergodic phase the system loses memory of its initial conditions and one expects $\bar{Z}_s \to 0$ in the thermodynamic limit. So in the limit of zero disorder $C_{\bar{Z}_s Z_s}$ also approaches zero. Going back to large but finite disorder, $\bar{Z}_s$ contains correlations with nearby spins. These correlations give finite contributions to $C_{\bar{Z}_s Z_s}$. Since these contributions depends on the spatial extent of $\bar{Z}_s$, it follows that $C_{\bar{Z}_s Z_s}$ should only depend on the disorder strength and not on L for large enough L. To check these claims, $C_{\bar{Z}_s Z_s}$ is calculated for the disordered Heisenberg chain in the $M_z = 0$ sector. As shown in Fig. 5-1, $C_{\bar{Z}_s Z_s}$ indeed appears to be independent of L deep in the MBL phase. In the ergodic phase, $C_{\bar{Z}_s Z_s}$ goes down with increasing system size, suggesting that $C_{\bar{Z}_s Z_s}$ might be zero below W_c in the thermodynamic limit. The most interesting feature appears near the region where $C_{\bar{Z}_s Z_s}$ appears to be diverging, this divergence can be attributed to the divergence of the localization length ξ.

$C_{\bar{O}O}$ is a potential experimental probe to diagnose the elusive ergodic-MBL phase transition in any dimensions with short or long ranged interactions, as long as the mechanism for MBL is based on l-bits. In FaP NMR experiments it is difficult to map out this transition because of a lack of strong intrinsic disorder. One can always use the pulse sequences to engineer the interaction to be small compared to the disorder, however this requires running the experiments at longer timescales to observe the "peak" feature in $C_{\bar{O}O}$. At longer timescales experimental imperfections start to matter, and the fidelity of the MQC intensities is reduced.

It will be interesting to look for 3 dimensional spin systems with strong disorder, such as lithium fluoride (LiF). Measuring $C_{\bar{O}O}$ in such a system will enable one to study the MBL-ergodic transition in 3 dimensions. Unlike in 1-dimensional spin sys-

---

[1] The staggered magnetization is needed here since the unstaggered total magnetization $Z = \sum_j S_z^j$ commutes with the Hamiltonian.

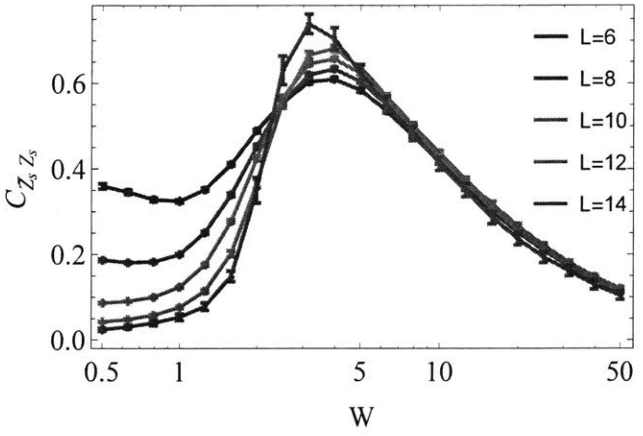

Figure 5-1: **Commutator norm between $\bar{Z}_s$ and Z_s as function of disorder** $C_{\bar{Z}_s Z_s}$ calculated via exact diagonalization in the $M_z = 0$ sector and averaged over 996 disorder realizations for $L = 6$ and $L = 8$, 336 realizations for $L = 10$ and $L = 12$, and finally 108 realizations for $L = 14$.

tems, correlations grows much faster in 3-dimensional systems, so the thermodynamic limit is effectively reached within reasonable experimental time.

5.2 Numerically Constructing l-bits from Eigenstates

The construction of l-bits is highly nontrivial [126, 118, 68], and most of the previous constructions have been based on perturbation methods. One annoying feature in perturbative approaches are the occurrence of resonances, which can make the perturbation series diverge. At each order in perturbation series, resonant blocks in the Hamiltonian must be isolated and separately diagonalized [126, 68]. From the view of perturbation theory, the stability of MBL phase hinges on the nonproliferation of resonances. It is natural to ask whether an exact construction of l-bit is possible. Such a solution will be useful to determine the stability of MBL phase in long-ranged and higher dimensional systems. So far, a rigorous proof of MBL exits only for 1D with short ranged interactions.

As shown in previous chapters, the commutator norm can provide information about the spatial extent of operators. Consider the commutator between a l-bit in the disordered Heisenberg model in Eq. and $X = \sum_j \sigma_x^j$:

$$C_{\tau X} = \frac{-1}{2^{L+2}L}\mathrm{Tr}[\tau_z, X]^2 \tag{5.5}$$

If τ_z is local, one expects the above commutator to be on the order of $\mathcal{O}(L^{-1})$. On the other hand, if τ_z is highly nonlocal the commutator should be on the order of $\mathcal{O}(1)$. Therefore in order for τ_z be a l-bit, it should minimize the commutator in Eq (5.5). Consider expanding τ_z in the eigenbasis of the Hamiltonian:

$$\tau_z = \sum_j a_j \left|j\middle\rangle\middle\langle j\right| \tag{5.6}$$

where $|j\rangle$ is an eigenstate, and a_j is a string of 2^L numbers with half of them being 1 and the other half being -1. This is because τ_z, like the local operator σ_z, only has eigenvalues 1 and -1. Substituting τ_z into Eq. (5.5) one arrives at

$$C_{\tau X} = \frac{1}{2^{L+1}L}\sum_{jk}(1 - a_j a_k)X_{jk}^2 \tag{5.7}$$

where $X_{jk} = \langle j|X|k\rangle$. Intuitively, one should have $a_j = a_k$ when X_{jk}^2 is large in order to minimize C. However this is still a hard problem to tackle, instead one can explicitly force the l-bit to be local with a support at σ_z^k by maximizing the quantity

$$\frac{1}{2^L}\mathrm{Tr}(\tau_z \sigma_z^k) = \frac{1}{2^L}\sum_j a_j \langle j|\sigma_z^k|j\rangle \tag{5.8}$$

In order to choose a string of a_j to maximize the above equation, first sort the diagonal matrix elements $\langle j|\sigma_z^k|j\rangle$ in ascending order, then choose -1 for the first half of the corresponding a_j and $+1$ for the second half. Any other configuration leads to less overlap.

Another choice for l-bits is to maximize the overlap with the noninteracting l-bits:

$$\frac{1}{2^L}\mathrm{Tr}(\tau_z\tilde{\tau}_z^k) = \frac{1}{2^L}\sum_j a_j \langle j|\tilde{\tau}_z^k|j\rangle \tag{5.9}$$

where $\tilde{\tau}_z$ are the noninteracting l-bits obtained by diagonalizing the free fermion part of the Hamiltonian.

5.2.1 $C_{\tau Z}$ in Noninteracting Disordered Systems

It is instructive to first look at the behavior for Eq. (5.5) in noninteracting disordered systems. In one dimension, all states are Anderson localized for any disorder strength. Therefore one expect the size of τ_z to be independent of L and Eq. (5.5) to scale as $\mathcal{O}(L^{-1})$. However, for weak disorder the localization length ξ can be quite large, so for smaller systems one observes larger than $\mathcal{O}(L^{-1})$ values in Eq. (5.5) due to finite size effects. As shown in Fig. 5-2, this apparent delocalization to localization transition goes away for noninteracting systems when L becomes larger than the typical ξ of the l-bits. The Hamiltonian used for the noninteracting model is $H_{\mathrm{AL}} = \sum_j S_x^j S_x^{j+1} + S_y^j S_y^{j+1} + \sum_j h_j S_z^j$, where the disorder h_j is drawn uniformly between $-W$ and W, and $J = 1$.

It is also instructive to look at $C_{\tau X}$ for noninteracting 1-dimensional systems which have delocalization-to-localization transition. Such systems can be realized using quasi-periodic [12] or correlated disordered fields [36]. As a demonstration, consider the Aubry-Andre model given by $H_{\mathrm{AA}} = \sum_j S_x^j S_x^{j+1} + S_y^j S_y^{j+1} + \lambda \sum_j \cos(2\pi\omega j) S_z^j$ [12], where $\omega = \sqrt{2}$ or any irrational number. The H_{AA} model has a transition at $\lambda = 1$, where the integral of motions go from being extended ($\lambda < 1$) to being l-bits ($\lambda > 1$). As shown in Fig. 5-3, this transition can be captured by $C_{\tau X}$ averaged over all integral of motions

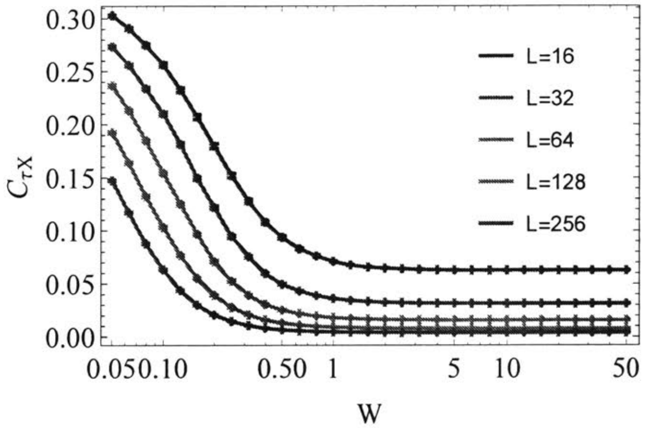

Figure 5-2: **Commutator norm between l-bits and X as function of disorder** Each commutator norm is averaged over all l-bits and 100 disorder realizations. OBC is used. The apparent delocalization to localization transition gradually goes away as the system size is increased.

5.2.2 $C_{\tau Z}$ in Interacting Disordered Systems

According to MBL phenomenology, the integrals of motions should show a transition from extended to localized around the critical disorder strength $W_c \approx 3.5$. Furthermore, one expects $C_{\tau X}$ to reflect this behavior since the commutator is a measure of the characteristic size of τ_z. However, as shown in Fig. 5-4(left) the commutator $C_{\tau X}$ shows an initial increase before decreasing as a function of disorder. In the limit of weak disorder, C_{τ_X} actually goes down as one increases the system size, suggesting that τ_z is becoming more local. This inconsistency is due to the fact that the construction of τ_z based on maximizing Eq. (5.9) is not quite correct. Namely while all the τ_z^j are mutually commuting, they are not mutually orthogonal, e.g., $\mathrm{Tr}(\tau_z^j \tau_z^k) \neq 2^L \delta_{jk}$. When the τ_z^j are not mutually orthogonal, the many-body Hamiltonian cannot be expressed using solely τ_z^j and products of τ_z^j. Interestingly, deep in the MBL phase, the constructed τ_z^j are actually mutually orthogonal, or very close to being mutually or-

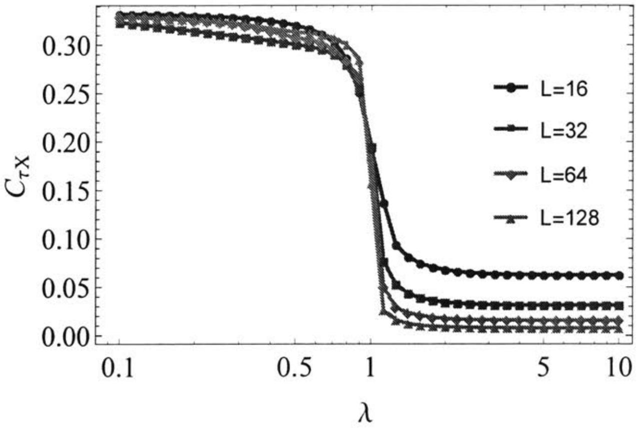

Figure 5-3: **Commutator norm between l-bits and X in Aubry-Andre model** The commutator is calculated using one disorder realization. The frequency is $\omega = \sqrt{2}$

thogonal. To check this, the quantity $D = 2^{-L}\binom{L}{2}^{-1}\sum_{j,j<k}\mathrm{Tr}(\tau_z^j\tau_z^k)$ is plotted against disorder for different system sizes in Fig. 5-4(right). For large disorder strength, the overlap between any two distinct l-bit is nearly always zero, indicating that the MBL Hamiltonian can be written in the form given by Eq. (5.2). However notice that D starts to diverge for larger disorder strength with increasing system size. This suggests that for large enough system sizes one may not always get mutually commuting l-bits constructed from Eq. (5.9) even at large disorder.

A consistent construction of mutually commuting integral of motions valid for all disorder strength is an interesting and challenging problem. This section attempted a nonperturbative construction of l-bits directly from eigenstates, but is unable to keep them mutually commuting in the ergodic phase or near the phase transition. Further direction might explore how to combine nonperturbative construction using eigenstates and perturbative approaches based on operators.

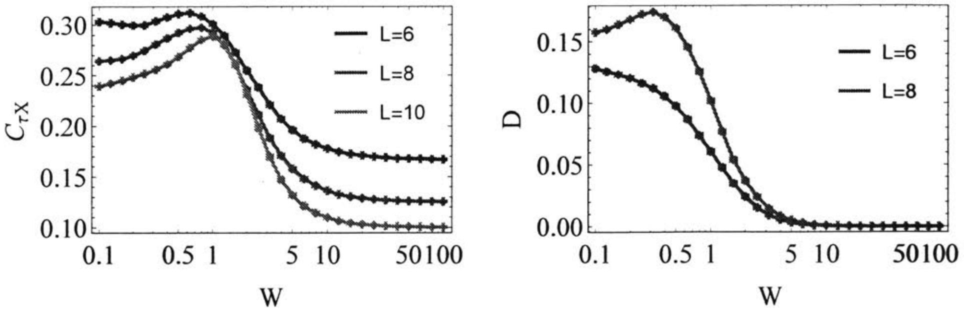

Figure 5-4: $C_{\tau X}$ **and** D **for disordered Heisenberg model.** $C_{\tau X}$ is averaged over all l-bits constructed from Eq. (5.9) and over 250 disorder realizations, while for D 500 disorder realizations are used.

5.3 Prethermalization from Breaking Integrability

As shown in Chapter 2 and 3, noninteracting 1 dimensional systems are integrable with an extensive set of IOMs' thus they cannot thermalize or scramble. As a result of their integrability, OTO commutators involving local operators such as σ_z saturate as a function of time.

One interesting question is whether this saturating behavior in the OTO commutators for integrable systems will survive under a weak integrability breaking perturbation. Intuitively, one expects the OTO commutators to remain constant for intermediate timescales when the perturbation is weak. This "prethermalization plateau" will cease to exist at long time scales when the system realizes it is no longer integrable [83].

To look for this prethermalization plateau, one can focus on the most "noninteracting" model achievable in spin chain NMR: the double quantum Hamiltonian $H_{\text{dq}} = \sum_{j,j<k} J_{jk}(S_x^j S_x^k - S_y^j S_y^k)$, which can be implemented straightforwardly using multi-pulse techniques. H_{dq} is noninteracting in the limit of only NN couplings, so couplings due to NNN and beyond can be considered as interactions which breaks the integrability of H_{eq}. Indeed, earlier experiments have already looked at the timescale

at which H_{eq} starts to show integrability breaking [151].

Here integrability breaking perturbation in the form of a disordered field $H_{\mathrm{pert}} = g\sum_j h_j(S_x^j + S_y^j)/\sqrt{2}$ is introduced into the system. In the integrable limit, OTO commutator $-\mathrm{Tr}[Z(t), Z]$ comes from only the ±2 order MQC intensity and shows strong oscillations in time. In order to observe integrability breaking, one can focus on the growth of the second moment using only the odd coherence orders, as they should all be zero in the integrable case. Fig. 5-5 is the measurement results. One see that in the absence of any perturbation the odd coherence orders are indeed very small. When perturbation is introduced, however, the odd coherence orders start to grow. It is not clear that a prethermal plateau can be identified from the measurements, as all curves, except for the two lowest ones, appears to start growing around the same timescale.

We remark that prethermalization in weakly broken integrable systems is different from the prethermalization studied in Chapter 4. In weakly broken integrable systems, prethermalization plateau is expected to survive up to a timescale on the order of $|g|^{-1}$ to g^{-2} [83], where g is strength of the integrability breaking perturbation. While in prethermal systems with emergent conserved quantities, the prethermal plateau is predicted to persist up to exponentially long timescale.

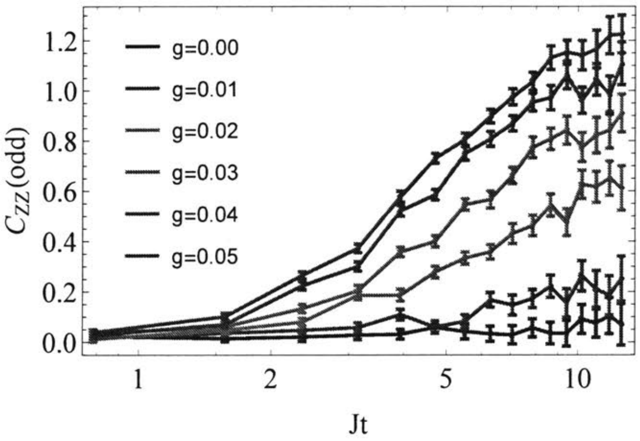

Figure 5-5: **Odd coherence order contribution to C_{ZZ} for the disordered double quantum model** C_{ZZ}(odd) shows a slow growth reminiscent of MBL, but it is happening for very small values of disorder.

Appendix A

Average Hamiltonian Theory

In the main paper we have used a broad range of Hamiltonians to explore different behaviors of the spin chains, ranging from integrable, to single particle and many-body localized. These Hamiltonians were obtained stroboscopically (Floquet Hamiltonians) by applying periodic rf pulse trains to the natural dipolar Hamiltonian that describes the system. We used Average Hamiltonian Theory (AHT [55]) as the basis for our Hamiltonian engineering method, to design the control sequences and determine the approximation errors.

To see how repeatedly applying a periodic pulse sequence modifies the dynamics of the system, we write the total Hamiltonian as $H = H_{\text{dip}} + H_{\text{ext}}$, where $H_{\text{dip}} = \frac{1}{2}\sum_{j<k} J_{jk}(2S_z^j S_z^k - S_x^j S_x^k - S_y^j S_y^k) + \sum_j h_j S_z^j$ is the system Hamiltonian, and $H_{\text{ext}}(t)$ is the external Hamiltonian due to the rf-pulses. The density matrix ρ evolves under the total Hamiltonian according to $\dot{\rho} = -i[H, \rho]$. Consider an interaction frame defined by $\rho' = U_{\text{rf}}{}^{\dagger}\rho U_{\text{rf}}$, where $U_{\text{rf}}(t) = \mathcal{T}\exp\left[-i\int_0^t H_{\text{ext}}(t')dt'\right]$ and $\mathcal{T}$ is the time ordering operator. In this *toggling* frame, ρ' evolves according to $\dot{\rho}' = -i[H', \rho']$, where $H' = U_{\text{rf}}{}^{\dagger} H_{\text{dip}} U_{\text{rf}}$. Since U_{rf} is periodic, H' is also periodic with the same period t_c. The evolution operator over one period can be written as $U(t_c) = \exp[-iH_{\text{F}}t_c]$, where H_{F} is called the *Floquet* Hamiltonian (or in the language of NMR the *Average Hamiltonian*). Note that if the pulse sequence satisfies the condition $U_{\text{rf}}(t_c) = \mathbb{1}$, the dynamics of ρ and ρ' are identical when the system is viewed stroboscopically, i.e., at integer multiples of t_c. The system evolves as if under a time-independent

Hamiltonian H_{F}. To calculate H_{F} we employ the Magnus expansion as is usual in AHT: $H_{\mathrm{F}} = H_0 + H_1 + \cdots$. The first two terms are given by

$$H_0 = \frac{1}{t_c}\int_0^{t_c} H'(t)dt, \quad H_1 = \frac{-i}{2t_c}\int_0^{t_c} dt_2 \int_0^{t_2} dt_1 [H'(t_2), H'(t_1)].$$

The zeroth order of the average Hamiltonian H_0 is often a good approximation to the Floquet Hamiltonian H_{F}, as the first order can be set to zero by simple symmetrization of the pulse sequence.

In fact it can be shown that all odd order correction can be made to be zero if the toggling frame Hamiltonian satisfies the property $H'(t) = H'(t_c - t)$ [54]. Sequences satisfying this property are referred to as symmetric sequences.

Bibliography

[1] D. Abanin, W. De Roeck, W. W. Ho, and F. Huveneers. A rigorous theory of many-body prethermalization for periodically driven and closed quantum systems. *Commun Math Phys*, 354:809–827, September 2017.

[2] Dmitry A. Abanin, Wojciech De Roeck, Wen Wei Ho, and François Huveneers. Effective Hamiltonians, prethermalization, and slow energy absorption in periodically driven many-body systems. *Phys. Rev. B*, 95:014112, 2017.

[3] A. Abragam. *Principles of Nuclear Magnetism.* Oxford Univ. Press, 1961.

[4] A. Ajoy and P. Cappellaro. Quantum simulation via filtered hamiltonian engineering: application to perfect quantum transport in spin networks. *Phys. Rev. Lett.*, 110:220503, 2013.

[5] F. C. Alcaraz, M. N. Barber, M. T. Batchelor, R. J. Baxter, and G. R W Quispel. Surface exponents of the quantum XXZ, Ashkin-Teller and Potts models. *J. Phys. A. Math. Gen.*, 20(18):6397–6409, 1987.

[6] Gonzalo A. Álvarez and Dieter Suter. Nmr quantum simulation of localization effects induced by decoherence. *Phys. Rev. Lett.*, 104:230403, 2010.

[7] Gonzalo A. Álvarez, Dieter Suter, and Robin Kaiser. Localization-delocalization transition in the dynamics of dipolar-coupled nuclear spins. *Science*, 349(6250):846–848, 2015.

[8] M. F. Andersen, A. Kaplan, and N. Davidson. Echo Spectroscopy and Quantum Stability of Trapped Atoms. *Phys. Rev. Lett.*, 90(2):023001, 2003.

[9] P. W. Anderson. Absence of diffusion in certain random lattices. *Phys. Rev.*, 109:1492–1505, Mar 1958.

[10] E. R. Andrew, A. Bradbury, and R. G. Eades. Nuclear magnetic resonance spectra from a crystal rotated at high speed. *Nature*, 182:1659 EP –, Dec 1958.

[11] E. R. Andrew, A. Bradbury, and R. G. Eades. Removal of dipolar broadening of nuclear magnetic resonance spectra of solids by specimen rotation. *Nature*, 183:1802 EP –, Jun 1959.

[12] S Aubry and G Andre. Analyticity breaking and anderson localization in incommensurate lattices. *Ann. Israel Phys. Soc*, 1980.

[13] Jens H. Bardarson, Frank Pollmann, and Joel E. Moore. Unbounded growth of entanglement in models of many-body localization. *Phys. Rev. Lett.*, 109(1):017202, Jul 2012.

[14] D. M. Basko, I. L. Aleiner, and B. L. Altshuler. Possible experimental manifestations of the many-body localization. *Phys. Rev. B*, 76:052203, Aug 2007.

[15] D.M. Basko, I.L. Aleiner, and B.L. Altshuler. Metal-insulator transition in a weakly interacting many-electron system with localized single-particle states. *Ann. Phys.*, 321(5):1126–1205, 2006.

[16] Bela Bauer and Chetan Nayak. Area laws in a many-body localized state and its implications for topological order. *J. Stat. Mech: Theory Exp.*, 2013(09):P09005, Sep 2013.

[17] J. Baum, M. Munowitz, A. N. Garroway, and A. Pines. Multiple-quantum dynamics in solid state nmr. *J. Chem. Phys.*, 83(5):2015–2025, 1985.

[18] J. Baum and A. Pines. Nmr studies of clustering in solids. *J. Am. Chem. Soc.*, 108:7447, 1986.

[19] J. Berges, Sz Borsányi, and C. Wetterich. Prethermalization. *Phys. Rev. Lett.*, 93(14):14–17, 2004.

[20] Juliette Billy, Vincent Josse, Zhanchun Zuo, Alain Bernard, Ben Hambrecht, Pierre Lugan, David Clement, Laurent Sanchez-Palencia, Philippe Bouyer, and Alain Aspect. Direct observation of anderson localization of matter waves in a controlled disorder. *Nature*, 453(7197):891–894, Jun 2008.

[21] Geoffrey Bodenhausen, Herbert Kogler, and R.R Ernst. Selection of coherence-transfer pathways in nmr pulse experiments. *J. Mag. Res.*, 58(3):370 – 388, 1984.

[22] D. P. Burum and W. K. Rhim. Analysis of multiple pulse nmr in solids. iii. *J. Chem. Phys.*, 71(2):944–956, 1979.

[23] P. Cappellaro, C. Ramanathan, and D. G. Cory. Simulations of information transport in spin chains. *Phys. Rev. Lett.*, 99(25):250506, 2007.

[24] Paola Cappellaro. Implementation of state transfer hamiltonians in spin chains with magnetic resonance techniques. In Georgios M. Nikolopoulos and Igor Jex, editors, *Quantum State Transfer and Network Engineering*, Quantum Science and Technology, pages 183–222. Springer Berlin Heidelberg, 2014.

[25] Paola Cappellaro, Lorenza Viola, and Chandrasekhar Ramanathan. Coherent-state transfer via highly mixed quantum spin chains. *Phys. Rev. A*, 83(3):032304, 2011.

[26] Anushya Chandran, Isaac H. Kim, Guifre Vidal, and Dmitry A. Abanin. Constructing local integrals of motion in the many-body localized phase. *Phys. Rev. B*, 91:085425, Feb 2015.

[27] H. Cho, D. G. Cory, and C. Ramanathan. Spin counting experiments in the dipolar-ordered state. *J. Chem. Phys.*, 118(8):3686–3691, 2003.

[28] Jae-Yoon Choi, Sebastian Hild, Johannes Zeiher, Peter Schauß, Antonio Rubio-Abadal, Tarik Yefsah, Vedika Khemani, David A. Huse, Immanuel Bloch, and Christian Gross. Exploring the many-body localization transition in two dimensions. *Science*, 352(6293):1547–1552, 2016.

[29] Soonwon Choi, Joonhee Choi, Renate Landig, Georg Kucsko, Hengyun Zhou, Junichi Isoya, Fedor Jelezko, Shinobu Onoda, Hitoshi Sumiya, Vedika Khemani, Curt von Keyserlingk, Norman Y. Yao, Eugene Demler, and Mikhail D. Lukin. Observation of discrete time-crystalline order in a disordered dipolar many-body system. *Nat.*, 543(7644):221–225, 2017.

[30] Soonwon Choi, Norman Y. Yao, and Mikhail D. Lukin. Dynamical engineering of interactions in qudit ensembles. *Phys. Rev. Lett.*, 119:183603, Nov 2017.

[31] Claude Cohen-Tannoudji, Jacques Dupont-Roc, and Gilbert Grynberg. *Atom-Photon Interactions: Basic Processes and Applications.* Wiley-Interscience, 1992.

[32] D.G Cory, J.B Miller, and A.N Garroway. Time-suspension multiple-pulse sequences: applications to solid-state imaging. *Journal of Magnetic Resonance (1969)*, 90(1):205 - 213, 1990.

[33] Giuseppe De Tomasi, Soumya Bera, Jens H. Bardarson, and Frank Pollmann. Quantum mutual information as a probe for many-body localization. *Phys. Rev. Lett.*, 118:016804, Jan 2017.

[34] W. Van der Lugt and W.J. Caspers. Nuclear magnetic resonance line shape of fluorine in apatite. *Physica*, 30(8):1658–1666, 1964.

[35] J. M. Deutsch. Quantum statistical mechanics in a closed system. *Phys. Rev. A*, 43:2046–2049, Feb 1991.

[36] David H. Dunlap, H-L. Wu, and Philip W. Phillips. Absence of localization in a random-dimer model. *Phys. Rev. Lett.*, 65:88–91, Jul 1990.

[37] J. Eisert, M. Cramer, and M. B. Plenio. *Colloquium* : Area laws for the entanglement entropy. *Rev. Mod. Phys.*, 82:277–306, Feb 2010.

[38] D. V. Else, P. Fendley, J. Kemp, and C. Nayak. Prethermal strong zero modes and topological qubits. *Phys. Rev. X*, 7(4):041062, October 2017.

[39] Dominic V. Else, Bela Bauer, and Chetan Nayak. Floquet Time Crystals. *Phys. Rev. Lett.*, 117(9):090402, 2016.

[40] Dominic V. Else, Bela Bauer, and Chetan Nayak. Prethermal phases of matter protected by time-translation symmetry. *Phys. Rev. X*, 7:011026, 2017.

[41] Dominic V. Else, Bela Bauer, and Chetan Nayak. Prethermal phases of matter protected by time-translation symmetry. *Phys. Rev. X*, 7:011026, Mar 2017.

[42] Dominic V. Else, Paul Fendley, Jack Kemp, and Chetan Nayak. Prethermal Strong Zero Modes and Topological Qubits. *Phys. Rev. X*, 7:041062, 2017.

[43] Ruihua Fan, Pengfei Zhang, Huitao Shen, and Hui Zhai. Out-of-time-order correlation for many-body localization. *ArXiv:1608.01914*, 2016.

[44] Edward B. Fel'dman and Serge Lacelle. Multiple quantum nmr spin dynamics in one-dimensional quantum spin chains. *Chem. Phys. Lett.*, 253(1-2):27 – 31, 1996.

[45] Nick Fläschner, Dominik Vogel, Matthias Tarnowski, Benno S. Rem, Dirk-Sören Lühmann, Markus Heyl, Jan Carl Budich, Ludwig Mathey, Klaus Sengstock, and Christof Weitenberg. Observation of a dynamical topological phase transition. 2016.

[46] M. Gärttner, P. Hauke, and A. M. Rey. Relating out-of-time-order correlations to entanglement via multiple-quantum coherences. *arXiv:1706.01616*, 2017.

[47] Martin Garttner, Justin G. Bohnet, Arghavan Safavi-Naini, Michael L. Wall, John J. Bollinger, and Ana Maria Rey. Measuring out-of-time-order correlations and multiple quantum spectra in a trapped-ion quantum magnet. *Nat. Phys.*, 13(8):781–786, August 2017.

[48] Martin Garttner, Justin G. Bohnet, Arghavan Safavi-Naini, Michael L. Wall, John J. Bollinger, and Ana Maria Rey. Measuring out-of-time-order correlations and multiple quantum spectra in a trapped-ion quantum magnet. *Nat. Phys.*, 13(8):781–786, 2017.

[49] Martin Gärttner, Philipp Hauke, and Ana Maria Rey. Relating out-of-time-order correlations to entanglement via multiple-quantum coherences. *Phys. Rev. Lett.*, 120(4):40402, 2017.

[50] M. Goihl, M. Friesdorf, A. H. Werner, W. Brown, and J. Eisert. Experimentally accessible witnesses of many-body localisation. *arXiv:1601.02666*, 2016.

[51] Thomas Gorin, Tomaž Prosen, Thomas H. Seligman, and Marko Žnidarič. Dynamics of Loschmidt echoes and fidelity decay. *Phys. Rep.*, 435(2-5):33–156, 2006.

[52] M. Gring, M. Kuhnert, T. Langen, T. Kitagawa, B. Rauer, M. Schreitl, I. Mazets, D. Adu Smith, E. Demler, and J. Schmiedmayer. Relaxation and prethermalization in an isolated quantum system. *Science (80-.).*, 337(6100):1318–1322, 2012.

[53] Berry Groisman, Sandu Popescu, and Andreas Winter. Quantum, classical, and total amount of correlations in a quantum state. *Phys. Rev. A*, 72:032317, Sep 2005.

[54] U. Haeberlen. *High Resolution NMR in Solids: Selective Averaging.* Academic Press Inc., New York, 1976.

[55] U. Haeberlen and J.S. Waugh. Coherent averaging effects in magnetic resonance. *Phys. Rev.*, 175(2):453–467, 1968.

[56] E.L. Hahn. Spin Echoes. *Phys. Rev.*, 80(4):580–594, 1950.

[57] Philipp Hauke and Markus Heyl. Many-body localization and quantum ergodicity in disordered long-range ising models. *Phys. Rev. B*, 92:134204, Oct 2015.

[58] Philipp Hauke, Markus Heyl, Luca Tagliacozzo, and Peter Zoller. Measuring multipartite entanglement through dynamic susceptibilities. *Nat Phys*, 12(8):778–782, Aug 2016.

[59] M. Heyl, A. Polkovnikov, and S. Kehrein. Dynamical quantum phase transitions in the transverse-field ising model. *Phys. Rev. Lett.*, 110(13):135704, 2013.

[60] Wen Wei Ho, Soonwon Choi, Mikhail D. Lukin, and Dmitry A. Abanin. Critical Time Crystals in Dipolar Systems. *Phys. Rev. Lett.*, 119(1):010602, 2017.

[61] Pavan Hosur and Xiao-Liang Qi. Characterizing eigenstate thermalization via measures in the Fock space of operators. *Phys. Rev. E*, 93(February):042138, 2016.

[62] Pavan Hosur, Xiao-Liang Qi, Daniel A. Roberts, and Beni Yoshida. Chaos in quantum channels. *Journal of High Energy Physics*, 2016(2):4, feb 2016.

[63] Pavan Hosur, Xiao Liang Qi, Daniel A. Roberts, and Beni Yoshida. Chaos in quantum channels. *J. High Energy Phys.*, 2016(2):4, 2016.

[64] Zixin Huang, Chiara Macchiavello, and Lorenzo Maccone. Usefulness of entanglement-assisted quantum metrology. *Phys. Rev. A*, 94:012101, Jul 2016.

[65] David A. Huse, Rahul Nandkishore, and Vadim Oganesyan. Phenomenology of fully many-body-localized systems. *Phys. Rev. B*, 90(17):174202, Nov 2014.

[66] David A. Huse and Vadim Oganesyan. A phenomenology of certain many-body-localized systems. *Phys. Rev. B*, 90,:174202, May 2013.

[67] Marko Žnidarič, Tomaz Prosen, and Peter Prelovšek. Many-body localization in the heisenberg xxz magnet in a random field. *Phys. Rev. B*, 77:064426, Feb 2008.

[68] John Z. Imbrie. Diagonalization and many-body localization for a disordered quantum spin chain. *Phys. Rev. Lett.*, 117:027201, Jul 2016.

[69] Aldo Isidori, Annika Ruppel, Andreas Kreisel, Peter Kopietz, Alexander Mai, and Reinhard M. Noack. Quantum criticality of dipolar spin chains. *Phys. Rev. B*, 84(18):1–6, 2011.

[70] Rajibul Islam, Ruichao Ma, Philipp M. Preiss, M. Eric Tai, Alexander Lukin, Matthew Rispoli, and Markus Greiner. Measuring entanglement entropy in a quantum many-body system. *Nature*, 528(7580):77–83, Dec 2015.

[71] P Jordan and E Wigner. About the pauli exclusion principle. *Z. Phys. B*, 47:631, 1928.

[72] P. Jurcevic, H. Shen, P. Hauke, C. Maier, T. Brydges, C. Hempel, B. P. Lanyon, M. Heyl, R. Blatt, and C. F. Roos. Direct Observation of Dynamical Quantum Phase Transitions in an Interacting Many-Body System. *Phys. Rev. Lett.*, 119(8):080501, aug 2017.

[73] Dhrubo Jyoti. Dipolarly-coupled chaotic quantum spin systems. *ArXiv:1711.01948*, November 2017.

[74] Adam M. Kaufman, M. Eric Tai, Alexander Lukin, Matthew Rispoli, Robert Schittko, Philipp M. Preiss, and Markus Greiner. Quantum thermalization through entanglement in an isolated many-body system. *Science*, 353(6301):794–800, 2016.

[75] C W Von Keyserlingk, Vedika Khemani, and S L Sondhi. Absolute stability and spatiotemporal long-range order in Floquet systems. *Phys. Rev. B*, 94:085112, 2016.

[76] Vedika Khemani, Achilleas Lazarides, Roderich Moessner, and S. L. Sondhi. Phase Structure of Driven Quantum Systems. *Phys. Rev. Lett.*, 116(25):250401, 2016.

[77] A. K. Khitrin. Growth of nmr multiple-quantum coherences in quasi-one-dimensional systems. *Chem. Phys. Lett.*, 274:217–220, 1997.

[78] Hyungwon Kim, Mari Carmen Bañuls, J. Ignacio Cirac, Matthew B. Hastings, and David A. Huse. Slowest local operators in quantum spin chains. *Phys. Rev. E*, 92:012128, Jul 2015.

[79] Hyungwon Kim and David A. Huse. Ballistic spreading of entanglement in a diffusive nonintegrable system. *Phys. Rev. Lett.*, 111:127205, Sep 2013.

[80] Hyungwon Kim, Tatsuhiko N. Ikeda, and David A. Huse. Testing whether all eigenstates obey the eigenstate thermalization hypothesis. *Phys. Rev. E*, 90:052105, Nov 2014.

[81] Alexei Kitaev. A simple model of quantum holography. 2015.

[82] Alexei Kitaev and S. Josephine Suh. The soft mode in the Sachdev-Ye-Kitaev model and its gravity dual. 2017.

[83] Marcus Kollar, F. Alexander Wolf, and Martin Eckstein. Generalized gibbs ensemble prediction of prethermalization plateaus and their relation to nonthermal steady states in integrable systems. *Phys. Rev. B*, 84:054304, Aug 2011.

[84] S. S. Kondov, W. R. McGehee, W. Xu, and B. DeMarco. Disorder-induced localization in a strongly correlated atomic hubbard gas. *Phys. Rev. Lett.*, 114:083002, Feb 2015.

[85] G. Kucsko, S. Choi, J. Choi, P. C. Maurer, H. Zhou, R. Landig, H. Sumiya, S. Onoda, J. Isoya, F. Jelezko, E. Demler, N. Y. Yao, and M. D. Lukin. Critical thermalization of a disordered dipolar spin system in diamond. *Phys. Rev. Lett.*, 121:023601, Jul 2018.

[86] Ivan Kukuljan, Sa šo Grozdanov, and Toma ž Prosen. Weak quantum chaos. *Phys. Rev. B*, 96:060301, Aug 2017.

[87] Serge Lacelle, Son Jong Hwang, and Bernard C. Gerstein. Multiple quantum nuclear magnetic resonance of solids: A cautionary note for data analysis and interpretation. *The Journal of Chemical Physics*, 99(11):8407–8413, 1993.

[88] Kevin A Landsman, Caroline Figgatt, Thomas Schuster, Norbert M. Linke, Beni Yoshida, Norm Y. Yao, and Christopher Monroe. Verified Quantum Information Scrambling. 2018.

[89] A I Larkin and Yu N Ovchinnikov. Quasiclassical Method in the Theory of Superconductivity. *Sov. Phys. JETP*, 28(6):1200–1205, 1969.

[90] Jun Li, Ruihua Fan, Hengyan Wang, Bingtian Ye, Bei Zeng, Hui Zhai, Xinhua Peng, and Jiangfeng Du. Measuring out-of-time-order correlators on a nuclear magnetic resonance quantum simulator. *arXiv:1609.01246*, 2016.

[91] Jun Li, Ruihua Fan, Hengyan Wang, Bingtian Ye, Bei Zeng, Hui Zhai, Xinhua Peng, and Jiangfeng Du. Measuring out-of-time-order correlators on a nuclear magnetic resonance quantum simulator. *Phys. Rev. X*, 7(3):031011, 2017.

[92] Elliott H. Lieb and Derek W. Robinson. The finite group velocity of quantum spin systems. *Communications in Mathematical Physics*, 28(3):251–257, 1972.

[93] Cheng-Ju Lin and Olexei I. Motrunich. Explicit construction of quasiconserved local operator of translationally invariant nonintegrable quantum spin chain in prethermalization. *Phys. Rev. B*, 96:214301, Dec 2017.

[94] A. Llor, Z. Olejniczak, and A. Pines. Coherent isotropic averaging in zero field nuclear magnetic resonance. i. general theory and icosahedral sequences. *The Journal of Chemical Physics*, 103(10):3966–3981, 1995.

[95] A. Llor, Z. Olejniczak, and A. Pines. Coherent isotropic averaging in zero field nuclear magnetic resonance. ii. cubic sequences and time reversal of spin couplings. *The Journal of Chemical Physics*, 103(10):3982–3997, 1995.

[96] A. Llor, Z. Olejniczak, J. Sachleben, and A. Pines. Scaling and time reversal of spin couplings in zero-field nmr. *Phys. Rev. Lett.*, 67:1989–1992, Oct 1991.

[97] David J. Luitz, Nicolas Laflorencie, and Fabien Alet. Many-body localization edge in the random-field heisenberg chain. *Phys. Rev. B*, 91:081103, Feb 2015.

[98] Alexander Lukin, Matthew Rispoli, Robert Schittko, M. Eric Tai, Adam M. Kaufman, Soonwon Choi, Vedika Khemani, Julian Léonard, and Markus Greiner. Probing entanglement in a many-body-localized system, 2018.

[99] Francisco Machado, Gregory D. Meyer, Dominic V. Else, Chetan Nayak, and Norman Y. Yao. Exponentially Slow Heating in Short and Long-range Interacting Floquet Systems. 2017.

[100] Juan Maldacena, Stephen H. Shenker, and Douglas Stanford. A bound on chaos. *J. High Energy Phys.*, 2016(8):106, 2016.

[101] Juan Maldacena and Douglas Stanford. Remarks on the Sachdev-Ye-Kitaev model. *Phys. Rev. D*, 94(10):106002, 2016.

[102] P. Mansfield, M. J. Orchard, D. C. Stalker, and K. H. B. Richards. Symmetrized multipulse nuclear-magnetic-resonance experiments in solids: Measurement of the chemical-shift shielding tensor in some compounds. *Phys. Rev. B*, 7(1):90, 1973.

[103] M. Mehring. *Principle of High Resolution NMR in Solids.* Springer-Verlag, 1983.

[104] Alexios A. Michailidis, Marko Žnidarič, Mariya Medvedyeva, Dmitry A. Abanin, Toma ž Prosen, and Z. Papić. Slow dynamics in translation-invariant quantum lattice models. *Phys. Rev. B*, 97:104307, Mar 2018.

[105] R. Moessner and S. L. Sondhi. Equilibration and order in quantum Floquet matter. *Nat. Phys.*, 13(5):424–428, 2017.

[106] M Munowitz and A. Pines. *Principle and Applications of Multiple-Quantum NMR*, volume Academic Press of *Advances in Chemical Physics.* Wiley, 1975.

[107] M Munowitz and A Pines. *Principles and application of multiple-quantum NMR*, volume 66 of *Adv. Chem. Phys.* Wiley, 1987.

[108] Michael Munowitz, Alexander Pines, and Michael Mehring. Multiple-quantum dynamics in nmr: A directed walk through liouville space. *J. Chem. Phys.*, 86(6):3172–3182, 1987.

[109] Rahul Nandkishore and David A. Huse. Many-body localization and thermalization in quantum statistical mechanics. *Annual Review of Condensed Matter Physics*, 6(1):15–38, Mar 2015.

[110] B. Neyenhuis, J. Smith, A. C. Lee, J. Zhang, P. Richerme, P. W. Hess, Z. X. Gong, A. V. Gorshkov, and C. Monroe. Observation of Prethermalization in Long-Range Interacting Spin Chains. *Sci. Adv.*, 3(August):1–10, 2017.

[111] Vadim Oganesyan and David A. Huse. Localization of interacting fermions at high temperature. *Phys. Rev. B*, 75:155111, Apr 2007.

[112] Arijeet Pal and David A. Huse. Many-body localization phase transition. *Phys. Rev. B*, 82(17):174411, Nov 2010.

[113] Z. Papic, E. Miles Stoudenmire, and Dmitry A. Abanin. Many-body localization in disorder-free systems: The importance of finite-size constraints. *Annals of Physics*, 362:714 - 725, 2015.

[114] M. Pasienski, D. McKay, M. White, and B. DeMarco. A disordered insulator in an optical lattice. *Nat Phys*, 6(9):677–680, 09 2010.

[115] M. Pino. Entanglement growth in many-body localized systems with long-range interactions. *Phys. Rev. B*, 90(17):174204, nov 2014.

[116] Tomaž Prosen, Thomas H. Seligman, and Marko Žnidarič. Theory of Quantum Loschmidt Echoes. *Prog. Theor. Phys. Suppl.*, 150:200–228, feb 2003.

[117] H. T. Quan, Z. Song, X. F. Liu, P. Zanardi, and C. P. Sun. Decay of Loschmidt echo enhanced by quantum criticality. *Phys. Rev. Lett.*, 96(14):140604, 2006.

[118] Louk Rademaker and Miguel Ortuño. Explicit local integrals of motion for the many-body localized state. *Phys. Rev. Lett.*, 116:010404, Jan 2016.

[119] Chandrasekhar Ramanathan, Paola Cappellaro, Lorenza Viola, and David G Cory. Experimental characterization of coherent magnetization transport in a one-dimensional spin system. *New J. Phys.*, 13(10):103015, 2011.

[120] Chandrasekhar Ramanathan, Hyungjoon Cho, Paola Cappellaro, Gregory S Boutis, and David G Cory. Encoding multiple quantum coherences in non-commuting bases. *Chem. Phys. Lett.*, 369:311, 2003.

[121] W. K. Rhim, D. D. Elleman, and R. W. Vaughan. Analysis of multiple pulse nmr in solids. *The Journal of Chemical Physics*, 59(7):3740–3749, 1973.

[122] W-K. Rhim, A Pines, and J. S. Waugh. Time-Reversal Experiments in Dipolar-Coupeld Spin Systems. *Phys. Rev. B*, 3(3):684, 1971.

[123] Marcos Rigol, Vanja Dunjko, and Maxim Olshanii. Thermalization and its mechanism for generic isolated quantum systems. *Nature*, 452(7189):854–858, Apr 2008.

[124] Giacomo Roati, Chiara D'Errico, Leonardo Fallani, Marco Fattori, Chiara Fort, Matteo Zaccanti, Giovanni Modugno, Michele Modugno, and Massimo Inguscio. Anderson localization of a non-interacting bose-einstein condensate. *Nature*, 453(7197):895–898, Jun 2008.

[125] Daniel A. Roberts, Douglas Stanford, and Leonard Susskind. Localized shocks. *Journal of High Energy Physics*, 2015(3):51, Mar 2015.

[126] V. Ros, M. Müller, and A. Scardicchio. Integrals of motion in the many-body localized phase. *Nuclear Physics B*, 891:420 – 465, 2015.

[127] E. Rufeil-Fiori, C. M. Sánchez, F. Y. Oliva, H. M. Pastawski, and P. R. Levstein. Effective one-body dynamics in multiple-quantum nmr experiments. *Phys. Rev. A*, 79(3):032324, 2009.

[128] Krzysztof Sacha and Jakub Zakrzewski. Time crystals: A review. *Reports Prog. Phys.*, 81(1):016401, 2018.

[129] Subir Sachdev. *Quantum Phase Transitions*. Cambridge University Press, 2 edition, 2011.

[130] Michael Schreiber, Sean S. Hodgman, Pranjal Bordia, Henrik P. Lüschen, Mark H. Fischer, Ronen Vosk, Ehud Altman, Ulrich Schneider, and Immanuel Bloch. Observation of many-body localization of interacting fermions in a quasi random optical lattice. *Science*, 349(6250):842–845, 2015.

[131] Maksym Serbyn, Z. Papić, and Dmitry A. Abanin. Local conservation laws and the structure of the many-body localized states. *Phys. Rev. Lett.*, 111(12):127201, Sep 2013.

[132] Maksym Serbyn, Z. Papić, and Dmitry A. Abanin. Criterion for many-body localization-delocalization phase transition. *Phys. Rev. X*, 5:041047, Dec 2015.

[133] E. K. Sklyanin. Boundary conditions for integrable quantum systems. *J. Phys. A. Math. Gen.*, 21(10):2375–2389, 1988.

[134] C. P. Slichter. *Principles of Magnetic Resonance*. Springer-Verlag, 3rd edition, 1996.

[135] A. Smith, J. Knolle, D. L. Kovrizhin, and R. Moessner. Disorder-free localization. *Phys. Rev. Lett.*, 118:266601, Jun 2017.

[136] J. Smith, A. Lee, P. Richerme, B. Neyenhuis, P. W. Hess, P. Hauke, M. Heyl, D. A. Huse, and C. Monroe. Many-body localization in a quantum simulator with programmable random disorder. *Nat. Phys.*, 12(10):907–911, October 2016.

[137] Daniel K. Sodickson and John S. Waugh. Spin diffusion on a lattice: Classical simulations and spin coherent states. *Phys. Rev. B*, 52:6467–6479, Sep 1995.

[138] Mark Srednicki. Chaos and quantum thermalization. *Phys. Rev. E*, 50(2):888, Aug 1994.

[139] Brian Swingle, Gregory Bentsen, Monika Schleier-Smith, and Patrick Hayden. Measuring the scrambling of quantum information. *Phys. Rev. A*, 94:040302, Oct 2016.

[140] Yupeng Wang, Wen-Li Yang, Junpeng Cao, and Kangjie Shi. *Off-diagonal Bethe ansatz for exactly solvable models.* Springer, 2016.

[141] J.S. Waugh, L.M. Huber, and U. Haeberlen. Approach to high-resolution nmr in solids. *Phys. Rev. Lett.*, 20:180, 1968.

[142] Ken Xuan Wei, Chandrasekhar Ramanathan, and Paola Cappellaro. Exploring localization in nuclear spin chains. *Phys. Rev. Lett.*, 120:070501, Feb 2018.

[143] Diederik S. Wiersma, Paolo Bartolini, Ad Lagendijk, and Roberto Righini. Localization of light in a disordered medium. *Nature*, 390(6661):671–673, Dec 1997.

[144] N. Y. Yao, C. R. Laumann, J. I. Cirac, M. D. Lukin, and J. E. Moore. Quasi-many-body localization in translation-invariant systems. *Phys. Rev. Lett.*, 117:240601, Dec 2016.

[145] N Y Yao, A C Potter, and A Vishwanath. Discrete Time Crystals : Rigidity , Criticality , and Realizations. *Phys. Rev. Lett.*, 118:030401, 2017.

[146] Norman Y. Yao, Fabian Grusdt, Brian Swingle, Mikhail D. Lukin, Dan M. Stamper-Kurn, Joel E. Moore, and Eugene A. Demler. Interferometric approach to probing fast scrambling. *Arxiv:1607.01801*, July 2016.

[147] Emil A. Yuzbashyan, Oleksandr Tsyplyatyev, and Boris L. Altshuler. Relaxation and persistent oscillations of the order parameter in fermionic condensates. *Phys. Rev. Lett.*, 96(9):097005, 2006.

[148] J. Zhang, P. W. Hess, A. Kyprianidis, P. Becker, A. Lee, J. Smith, G. Pagano, I. D. Potirniche, A. C. Potter, A. Vishwanath, N. Y. Yao, and C. Monroe. Observation of a Discrete Time Crystal. *Nat.*, 543(7644):217–219, 2016.

[149] J. Zhang, G. Pagano, P. W. Hess, A. Kyprianidis, P. Becker, H. Kaplan, A. V. Gorshkov, Z.-X. Gong, and C. Monroe. Observation of a many-body dynamical phase transition with a 53-qubit quantum simulator. *Nature*, 551(7682):601–604, nov 2017.

[150] Shanmin Zhang, B. H. Meier, and R. R. Ernst. Polarization Echoes in NMR. *Phys. Rev. Lett.*, 69(14):2149, 1992.

[151] Wenxian Zhang, Paola Cappellaro, Natania Antler, Brian Pepper, David G. Cory, Viatcheslav V. Dobrovitski, Chandrasekhar Ramanathan, and Lorenza Viola. Nmr multiple quantum coherences in quasi-one-dimensional spin systems: Comparison with ideal spin-chain dynamics. *Phys. Rev. A*, 80(5):052323, 2009.

[152] Wurong Zhang and D. G. Cory. First direct measurement of the spin diffusion rate in a homogenous solid. *Phys. Rev. Lett.*, 80:1324–1327, Feb 1998.

[153] Bojan Žunkovič, Markus Heyl, Michael Knap, and Alessandro Silva. Dynamical Quantum Phase Transitions in Spin Chains with Long-Range Interactions: Merging Different Concepts of Nonequilibrium Criticality. *Phys. Rev. Lett.*, 120(13):130601, 2018.